NANOSTRUCTURED POLYMERIC MATERIALS AND THEIR IMPLEMENTATION IN ENHANCING BIOCATALYTIC PROCESSES

By

Garrett R. Chado

B.S., University of Chicago, 2013

A thesis submitted to the

Faculty of the Graduate School of the

University of Colorado in partial fulfillment

of the requirement for the degree of

Doctor of Philosophy

Department of Chemical and Biological Engineering

2018

This thesis entitled:
Nanostructured Polymeric Materials and Their Implementation in Enhancing Biocatalytic Processes
written by Garrett R. Chado
has been approved for the Department of Chemical and Biological Engineering

_____
(Dr. Joel L. Kaar)

_____
(Dr. Mark P. Stoykovich)

Date_____

The final copy of this thesis has been examined by the signatories, and we find that both the content and the form meet acceptable presentation standards of scholarly work in the above mentioned discipline.

Chado, Garrett R. (Ph.D., Chemical and Biological Engineering)

Nanostructured Polymeric Materials and Their Implementation in Biocatalytic Processes

Thesis directed by Dr. Joel L. Kaar and Dr. Mark P. Stoykovich

Polymer science has played a pivotal role in the development of nanotechnology. Self-assembly of polymeric materials at the molecular-level enables the fabrication of periodic arrays of nanostructures with various geometries and sizes, which present exciting opportunities in fabrication of nanoscale devices. However, self-assembled structures are often too regular for use in fabricating complex devices. Therefore, a simple layer-by-layer method was developed to allow for quantitative control over both size and shape of equilibrium nanostructures in self-assembled block copolymer thin films. The use of photolithography imparted spatial control over the self-assembly process.

Such self-assembly can result in structures approaching the size of single biomacromolecules, potentially enabling the precise placement of individual enzymes. Using these nanostructured thin films as inspiration, the effect of nanopatterning enzymes for multi-step biocatalysis was explored numerically by developing a kinetic Monte Carol simulation. Molecular trajectories of the reaction species as well as turnover frequency of individual enzymes on the surface were tracked under diffusion-limited and reaction-limited conditions. Interestingly, these simulations revealed that enzyme density and arrangement have little impact on overall activity of the multi-enzyme cascade reaction.

Given these results, we turned our attention to improving enzymatic activity by covalent modification of the enzyme with polymeric materials. This covalent modification holds tremendous promise as an approach to tune the molecular-level interactions between enzymes and their solvent environments. Enzymes modified with highly soluble polymers had greatly improved

solubility in an ionic liquid. This correlated with increases of up to 19-fold in enzyme activity. However, because the preparation and purification of enzymes can be costly, the loss of recyclability of the newly homogeneous enzyme-polymer conjugates was undesirable. By utilizing a responsive polymeric material, the miscibility of the enzyme can be altered adaptively. Specifically, thermodynamic interactions between the enzyme-polymer conjugate and solvent were varied as a function of temperature by utilizing a thermoresponsive polymer. When recycled via sequential dissolution and precipitation, the enzyme did not lose any activity. This approach enables the benefits of both increased activity of homogeneous biocatalysis and improved processability of heterogeneous biocatalysis in non-native solvents.

Acknowledgements

There are many people without whom the work presented in this thesis would not have been possible. First and foremost, I would like to thank my advisors, Dr. Joel Kaar and Dr. Mark Stoykovich. Their questions and ideas kept me from getting lost in the minutiae. They constantly challenged me and gave me every opportunity to try something new.

I would also like to thank past and present members of the Kaar and Stoykovich labs, Joseph Plaks, Samantha Summers, James Weltz, David Faulon, Andres Chaparro, Rebecca Falatach, Louis Sacks, Alaksh Choudhury, Dr. Kelsey MacConaghy, Dr. Sukwon Jung, Dr. Chunlin He, Dr. Erik Nordwald, Nuria Cordina, and Kate Morrissey, for all their support along the way. I would also like to thank my undergraduate research assistants, Christopher Phenicie, Elijah Holland, and Andrew Tice, for their hard work and long hours in the lab.

My roommates, Dr. Matthew McBride, Sherry D'Andrea, and Samantha Summers, have been particularly important in getting me through grad school. I would like to especially thank Sam, whose strength, resilience, and optimism are inspirational.

I would like to thank my committee members, Dr. Jennifer Cha, Dr. Jerome Fox, and Dr. Yifu Ding. It should come as no surprise to my friends and family that our committee meetings ran longer than expected on account of my verboseness.

I would like to acknowledge the NSF GRFP and GAANN programs for financial support, as well as the Nanomaterials Characterization Facility, the Colorado Nanofabrication Laboratory, and the Keck Lab for access to instruments and additional technical support. Additionally, I would like to thank the innumerable staff, administrators, graduate students, and post-doctoral scholars who provide the foundation of the CHBE department. Special thanks to the eternally jovial Dominique De Vangel, who somehow makes sure every graduate student is accounted for.

Finally, I would like to thank my friends, family, and teachers who recognized and encouraged my love of learning from a young age. I am eternally grateful to my parents and sisters; whose unconditional support and encouragement gave me the self-confidence and resolve to get through grad school. Most importantly, Elise Wummer has been by my side to celebrate in the successes and endure the lows of graduate school. Her love and support has provided more inspiration and motivation than I could possibly have asked for.

TABLE OF CONTENTS

List of Tables

List of Figures

Chapter 1: Introduction

Bottom-up self-assembly is a process wherein objects, whether atoms, molecules, or particles, spontaneously associate into well-defined geometries. As a result, bottom-up processes are typically capable of producing nanostructures quickly, in high throughput, and at low cost. In particular, the self-assembly of block copolymers (BCPs) has generated great interest as a bottom-up route to fabricating dense periodic arrays of features below the limits of conventional optical lithography (5-50 nm). Advances in polymer science, especially in living radical polymerizations, have enabled unprecedented sequence control in BCP synthesis.[1–5] This results in a staggering number of possible equilibrium morphologies achievable by BCP self-assembly.

In typical applications of BCP self-assembly, the resulting nanostructures are at thermodynamic equilibrium and so a specific material will result in only a single geometry across the entire sample. While this has shown promise in manufacturing devices which require dense periodic arrays of monodisperse features such as bit-patterned media, it presents challenges in utilizing BCP self-assembly to manufacture highly complex devices which require diverse nanostructures in close proximity. For example, as we continue to push Moore's law into the future we require more creative nanoscale architectures to achieve heterogeneous integration and 3-dimensional system in packaging with exceedingly low defect density.

Specialized approaches have shown BCP self-assembly of up to two distinct morphologies in a single continuous film. One such approach relies on kinetically trapping nonequilibrium morphologies of a single BCP material.[6,7] However, trapping nonequilibrium morphologies often leads to high defect densities and significant roughness at the interface between phase separated domains that complicates device manufacture. While very precise control over the nonequilibrium morphologies can be achieved with electron-beam irradiation, this is notoriously slow and

therefore not feasible for high throughput manufacturing. Another approach involves two materials deposited in a multistep exposure-and-development process.[8] However, this approach requires separate BCP materials for each desired morphology and domain size. It would therefore be desirable to alter the morphology and domain spacing of self-assembled BCP nanostructures *in situ* utilizing an additive method that results in equilibrium nanostructures. This would decrease the number of both manufacturing steps and necessary materials, therefore reducing the overall complexity of the manufacturing process.

To this end, in this thesis a facile layer-by-layer technique is demonstrated to selectively tune morphology and domain spacing of nanostructures self-assembled by BPC materials in a single continuous thin film. This approach uses sequential deposition and mixing of BCP and/or homopolymer layers to form well-mixed BCP blends that results in equilibrium nanostructures. Nanostructure is then fixed in spatially defined regions of the film via photoinduced crosslinking using standard photolithographic techniques to achieve diverse morphologies and sizes in contiguous regions of the film. Furthermore, this approach is compatible with existing methods of directed self-assembly to achieve defect-free self-assembly[9,10] as well as soft lithography techniques such as microcontact printing[11] and electrohydrodynamic jet printing.[12] This method also enables the selective and hierarchical functionalization of the self-assembled nanostructures which may be used in the development of ultrahigh-density biosensors or other applications where the ability to pattern a diverse set of chemical functional groups across multiple length scales is necessary.[13,14]

A particularly fascinating form of self-assembly is the intramolecular self-assembly, or folding, of proteins. The function of most proteins, whether membrane, fibrous, or globular, is ultimately derived from the self-assembly of the primary polypeptide sequence into the secondary

structure, which results in folding of the tertiary structure, that can, in turn, lead to quaternary structure such as oligomerization. One possible exception to this is intrinsically disordered proteins, in which the function may derive primarily from the dynamics of the protein rather than the structure.[15] Of particular interest, though, are enzymes: catalytically active proteins capable of remarkable selectivity and extraordinary catalytic efficiency.

In nature, many important synthetic and metabolic pathways rely on multistep biotransformation reactions catalyzed by a number of different enzymatic active sites. This may result from intramolecular tunnels that direct the flow of intermediates from one active site to the next,[16] electrostatic channels on the surface of multienzyme complexes,[17,18] or even from simple colocalization effects.[19] It is exceedingly difficult to design *de novo* enzymes, and so artificially engineering intramolecular tunnels is currently not feasible as a strategy. Even engineering of artificial supramolecular enzyme complexes remains difficult as protein-protein interactions are still not fully understood. Rather, a straightforward approach is to simply colocalize the enzymes to a synthetic scaffold. This approach had been used in biocatalysis,[20,21] enzyme-mediated electrocatalysis (*i.e.*, enzymatic biofuel cells),[22,23] biosensing,[24] and synthetic biology.[25] While colocalization of enzymes to synthetic scaffolds is relatively straightforward, the influence of enzyme density and spatial arrangement on surfaces is a matter of some debate.[26,27] Specifically, the role of enzyme density and spatial arrangement on diffusion of intermediates between enzymes is poorly understood.

Given the interest in improving multienzyme cascade reactions on surfaces, the dependence of overall cascade activity on the density and arrangement of enzymes on a two-dimensional surface is explored numerically in this thesis. Random, linear striped, and hexagonal arrangements of the sequential enzymes are considered due to the availability of fabrication

techniques for heterogeneously functionalizing surfaces with such patterns (*i.e.*, BCP self-assembly). Specifically, the impact of geometric arrangement and density is analyzed for a two-enzyme cascade in both the diffusion-limited (where the overall reaction rate is limited by molecular transport of the substrate and intermediate molecules) and reaction-limited (where the overall reaction rate is limited by the enzymatic turnover of the substrate and intermediate) regimes. The results presented here ultimately bring into question the rationale for using highly sophisticated techniques to pattern enzymes with nanometer precision. Rather, it seems that in densely packed systems, as are common for use in biocatalysis, random immobilization is just as efficient as highly ordered arrangements, significantly simplifying the engineering of such systems.

Whereas the immobilization of enzyme cascades on surfaces has promising applications, when it comes to large-scale biocatalysis it is generally more favorable to utilize enzymes in bulk solution. By using non-aqueous solvents as media for biocatalytic reactions, the portfolio of feasible biotransformations may be greatly expanded. Specifically, utilizing non-aqueous solvents avoids water-dependent side reactions, shifts equilibrium to favor synthesis over hydrolysis, increases solubility of hydrophobic substrates and products, and can even enhance or alter regio- and enantio-specificity.[28–30] Hydrophobic ionic liquids (ILs) are particularly interesting as reaction media for biocatalysis. Hydrolytic enzymes have shown interesting properties in hydrophobic ILs[31–33] compared to other hydrophobic organic solvents. However, while the benefits of ILs as solvents for non-aqueous biocatalysis have been well documented,[30] enzyme activity in ILs, like other non-aqueous solvents, is generally lower than in aqueous environments. One of the dominant factors that contributes to low activity of enzymes in anhydrous hydrophobic ILs is poor solubility

of the enzyme. As a result, the dry (*i.e.*, lyophilized) enzyme is typically suspended as macroscopic aggregates in the IL, but this leads to significant diffusional limitations.

Covalently tethering polymers to enzymes provides a promising approach to dissolving enzymes in ILs. However, very few different polymer chemistries have been explored for this purpose with virtually all cases relying on poly(ethylene glycol) (PEG). In order to effectively solubilize the resulting enzyme-polymer conjugate, it is desirable to utilize a highly IL-soluble polymer to overcome the significant unfavorable enzyme-IL interactions that prevent solubility of the pure enzyme. The synthesis and identification of IL-soluble polymers for use in ion gels for gas separations and ion-conducting electrolyte membranes for battery and fuel cell applications has received considerable attention[34,35] and this body of work makes polymer selection relatively straightforward.

While such an approach can lead to fully soluble biocatalyst with dramatically enhanced activity, the ease of separation and recyclability of insoluble heterogenous enzymes has been viewed as a key benefit of biotransformations in ILs. This tradeoff between solubility and recyclability diminishes the overall benefit of the more active homogeneous enzyme-polymer conjugate. One would ideally wish to take advantage of both the higher activity in the homogeneous state and the recyclability of the heterogeneous state. This can be achieved by utilizing a stimuli-responsive polymer that is highly soluble under certain conditions relevant for the biotransformation but can be made insoluble by application of an external stimulus, such as temperature.

Strategies to both improve the solubility of enzymes in hydrophobic ILs as well as control the phase behavior (*i.e.*, solubility) of enzyme-polymer conjugates are presented in this thesis. Using controlled radical polymerization techniques, a simple and general conjugation scheme is

presented to attach various polymers to the surface of enzymes via covalent modification. First, the impact of polymer chain length on solubility of the enzyme-polymer conjugate in a hydrophobic IL is explored in detail. Light scattering techniques are used to assess the impact of polymer modification on colloidal stability of the enzyme-polymer conjugate as well as to measure molecular-level interactions between the polymer and the IL. Enzymatic activity of the enzyme-polymer conjugates is assessed as a function of polymer molecular weight, revealing that increases in enzymatic activity are strongly correlate with improvements to conjugate solubility. Then, a thermoresponsive polymer is used with upper critical solution temperature (UCST) type phase behavior to dynamically control the solubility of the resulting enzyme-polymer conjugates using solvent temperature as a control. Recyclability of the conjugates is demonstrated by cycling the conjugates between the soluble and insoluble state and measuring activity retention as a function of this cycling. Interestingly, thermoreversible shuttling of the conjugates between the IL phase and an aqueous phase is also shown as an exciting and novel approach to achieve direct phase transfer of the catalytically active enzyme-polymer conjugate.

Chapter 2: Background

2.1 Block Copolymer Self-Assembly

2.1.1 Block Copolymer Phase Separation

Block copolymers (BCPs) are a class of macromolecule that is formed by covalently joining chemically distinct homopolymers to form 'blocks' within the copolymer chain. The simplest case is an A-B diblock copolymer composed of two constitutive blocks, though advances in polymer science have allowed for increasingly complex molecular architectures including triblock copolymers, star block copolymers, miktoarm star copolymers, bottlebrush copolymers, and others (**Figure 2.1**).[36–40] Depending on the thermodynamic compatibility of the blocks in the solid state, microphase separation of A-B diblock copolymers into A-rich ad B-rich domains may occur. In the absence of the covalent bond joining the A and B blocks, this phase separation would result in poorly controlled macroscale phase separation. However, this covalent bond forces an extended interface between A-rich and B-rich domains that is proportional in surface area to the number of polymer chains.

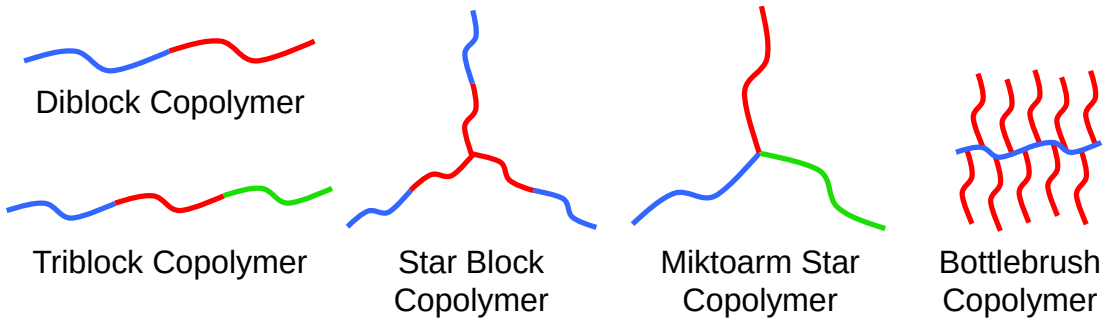

Figure 2.1 Schematic representation of different copolymer architectures.

The driving forces behind phase separation are balanced by an elastic restoring force that arises from entropic penalties associated with ordering of the BCP that results from this forced interface. This causes the material to spontaneously adopt extended periodic nanostructures driven

by the thermodynamic minimization of free energy that can be described by two simple parameters: the product χN, where χ is the Flory-Huggins interaction parameter and N is the degree of polymerization, and the relative volume fraction of the blocks, $\phi_A (= 1 - \phi_B)$. The one-dimensionally periodic lamellar pattern is most thermodynamically stable for roughly symmetric diblock copolymers. As the BCP becomes more asymmetric, significant curvature is introduced at the interface allowing greater conformational flexibility to the majority block on the convex side of the interface. This results in hexagonally packed cylindrical domains at intermediate degrees of asymmetry and eventually spherical domains of the minority block embedded in a matrix of the majority block as asymmetry is increased further. There is even a small window for a three-dimensionally periodic bicontinuous phase known as the gyroid. Phase diagrams describing these morphologies as a function of both χN and ϕ_A can be characterized empirically[41] or may be determined theoretically.[42] **Figure 2.2** shows representative SEM images and schematic phase diagrams of structures self-assembled by poly(styrene-*block*-(methyl methacrylate)), a widely studied BCP.

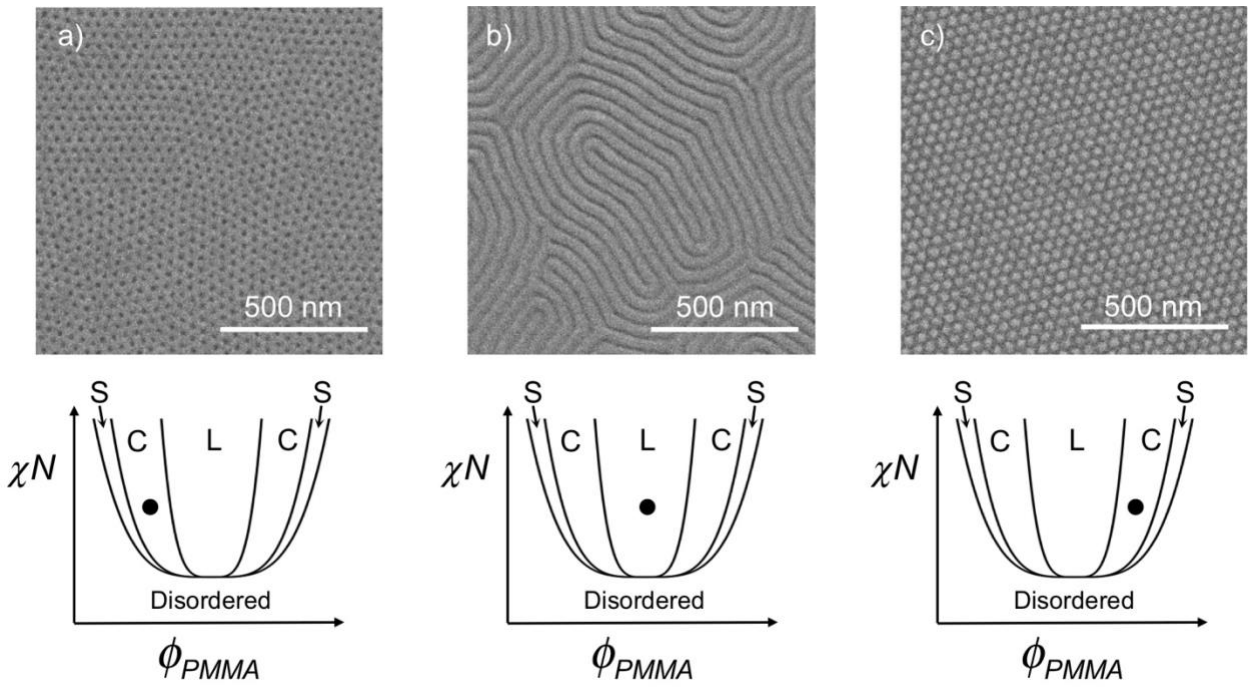

Figure 2.2 SEM images and phase diagrams of structures self-assembled by poly(styrene-*block*-(methyl methacrylate)) (PS-*b*-PMMA) of similar total molecular weight with varying degrees of asymmetry. The light and dark colors in the SEM images correspond to the PS and PMMA domains, respectively. Schematic phase diagrams illustrate the composition of the pictured block copolymers. The lamellar, cylindrical, and spherical phase windows are denoted as L, C, and S, respectively. a) PS-*b*-PMMA containing 20-*b*-50 kg mol^{-1} and ϕ_{PMMA} = 0.70 self-assembles to form PMMA-rich cylinders in a PS matrix. b) PS-*b*-PMMA containing 47-*b*-53 kg mol^{-1} and ϕ_{PMMA} = 0.50 self-assembles to form lamellar structure. c) PS-*b*-PMMA containing 46-*b*-21 kg mol^{-1} and ϕ_{PMMA} = 0.29 self-assembles to form PS-rich cylinders in a PMMA matrix. All structures are oriented perpendicular to the substrate surface.

Whereas the relative length of each block determines the morphology, the total length of the BCP is intuitively related to the size of the domains as shown in **Figure 2.3**. Between 1974 and 1981, Takeji Hashimoto and coworkers published a series of papers in which they explored the various factors that affect the structure and size of self-assembled BCP domains.[43–47] They determined theoretically and verified experimentally that $D \propto N^{2/3}$ where D is the domain spacing (*i.e.*, period) of phase separated domains and N is the molecular weight of the block copolymer. Consider briefly a symmetric lamellar-forming diblock copolymer (*i.e.*, $\phi_A = \phi_B = {}^1/_2$). Assuming the polymer is incompressible and domains are composed of pure A or B (*i.e.*, the interfacial region is very thin), then we can simplify contributions to the free energy per chain to

two components: $F/k_BT \propto (D/2)^2/Na^2 + (\gamma/k_BT)\sigma$ where γ is the interfacial tension of between A and B domains and σ is the surface area per chain at the interface. The first term accounts for free energy contributions associated with stretching of the chains to a half period (approximated as Hookian) and the second term accounts for contributions due to interactions at the interface between the two domains. By noticing that $\sigma D/2 = Na^3$, the free energy becomes $F/k_BT \propto (D/2)^2/Na^2 + (\gamma/k_BT)(2Na^3/D)$ and minimization with respect to D shows $D \propto N^{2/3}$.

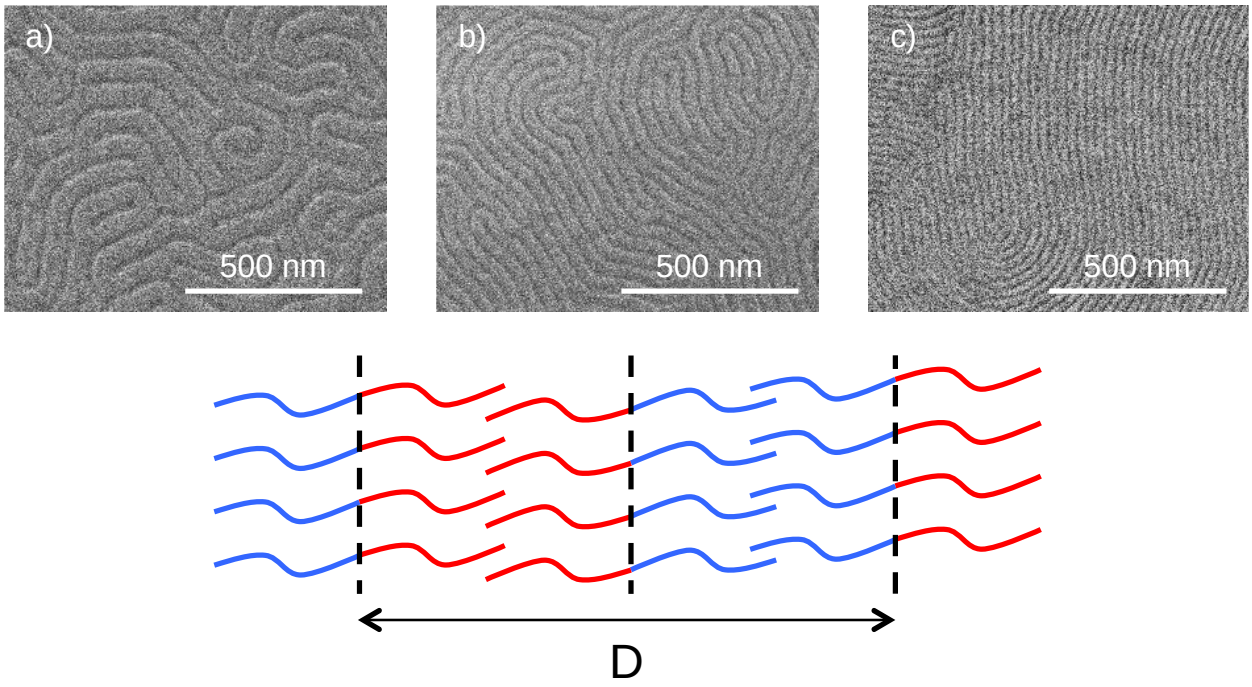

Figure 2.3 SEM images of lamellar structures self-assembled by PS-*b*-PMMA block copolymers with similar ϕ_{PMMA} and varying molecular weights and schematic representation of ordered lamellar domains where D represents the domain spacing. a) 85-*b*-91 kg mol^{-1}, ϕ_{PMMA} = 0.49, b) 47-*b*-53 kg mol^{-1}, ϕ_{PMMA} = 0.50, c) 25-*b*-26 kg mol^{-1}, ϕ_{PMMA} = 0.48. Light and dark colors in SEM images correspond to PS and PMMA domains, respectively.

2.1.2 Block Copolymer Blends

While advances in living polymerizations allow for very precise control over molecular weight and volume fraction of each block, synthesizing a library of block copolymers to provide

a continuum of self-assembled structures is prohibitive. To alleviate these synthetic demands, diblock copolymer blends can be used to tune both the size and morphology of self-assembled structures.[48–53] Interestingly, the same scaling law applies to BCP blends by simply using the average molecular weight of the system. That is, $D_B \propto (\sum_i x_i N_i)^{2/3}$ where D_B is the domain spacing of the blend, and x_i and N_i are the mole fraction and molecular weight of species i, respectively.[49,54] This means that we can access a continuum of domain spacings by simply using the appropriate ratio of two BCP materials. Mayes *et al.*, for example, achieved domain spacings ranging from 16 nm to 52 nm by blending two poly(styrene-*b*-(methyl methacrylate)) BCPs with molecular weights of 29.8 and 120 kg mol^{-1}. However, it should be noted that BCPs differing in molecular weight by more than a factor of 5 are not likely to be miscible and will result in coexisting macroscopic domains with differing domain spacing.[49,50]

In addition to blending of multiple BCPs, symmetric blending of an A-B diblock copolymer with equal volume fractions of the corresponding A/B homopolymers increases the domain spacing as a function of the total volume fraction of the added homopolymer blend, ϕ_h.[55,56] Liu *et al.* thoroughly characterized ternary blends of poly(styrene-*b*-(methyl methacrylate))/polystyrene/poly(methyl methacrylate) in thin films and found the increase in lamellar spacing was well-described by the empirical relation $D_B = D_0/(1-\phi_h)^{\beta}$ where D_B is the domain spacing of the ternary blend, D_0 is the domain spacing of the pure BCP, and β is linearly dependent on the ratio of molecular weights of the BCP and homopolymer.[57] This increase in domain spacing is the result of homopolymers partitioning into the corresponding blocks of the phase separated BCP domains.

Importantly, there are upper limits on both β and ϕ_h. When homopolymer molecular weight is lower than that of the BCP (i.e., β is small), the homopolymer is evenly distributed

throughout the corresponding lamellar domain. As the relative molecular weight of the homopolymer increases, the homopolymer begins to be preferentially excluded towards the center of the lamellar domains until, at a sufficiently large value of β, the homopolymer is completely excluded and will not swell the lamellar domains.[55] Therefore, there is an upper limit to the value of β at which the homopolymer will no longer increase domain spacing, and typical applications should rely on homopolymers with molecular weights no more than five times that of the BCP. Additionally, as ϕ_h is increased, the lamellar structure eventually gives way to the formation of a microemulsion. Limitations on both β and ϕ_h ultimately restrict the maximum extent to which the natural domain spacing of the pure BCP can be extended.

Similarly, blending an A-B diblock copolymer with a single homopolymer (A or B) can be used to modify the equilibrium morphology. As characterized previously in the bulk,[58] increasing the volume fraction of homopolymer can elicit an order-order transition between microphase separated domains such as from lamellar to cylindrical structures. This phenomenon is also due to the partitioning of the homopolymer into the appropriate domain. As the homopolymer content increases, the effective volume fraction of that block also increases causing changes to BCP equilibrium morphology similar to what is observed for pure BCP systems.

2.1.3 Block Copolymer Self-Assembly for Fabrication

This precise control that can be achieved over both morphology and domain size in phase-separated BCPs has generated great interest as a bottom-up route to fabricating dense periodic arrays of features below the limits of conventional optical lithography. In order to be useful as a fabrication technique, the BCP patterns must be transferred into a functional material such as electronic, optical, magnetic, or semiconducting materials.[59–64] In many of these applications, a

thin film (<100 nm) of self-assembled BCP acts similarly to a traditional photoresist serving as either a template or a mask for either deposition of material or etching into the underlying substrate. In a typical approach, the BCP is first self-assembled followed by selective removal of one of the BCP domains to expose the underlying substrate. Additive or subtractive processes such as vapor phase deposition or etching, respectively, may then be used to transfer the pattern into the functional material on the substrate surface.

Standard implementations of BCP lithography use a single BCP material in the thin film, and thus allow for self-assembly into only a single equilibrium morphology with regular structure and dimension. While this has shown promise in fabricating devices that rely on dense periodic arrays of nanoscale features such as magnetic bit patterned media[65,66] and multigate field effect transistors,[67] sometimes more control over the pattern geometries and dimensions is required lithographically. For example, Fresnel zone plates used to focus x-ray light consist of nanoscale concentric rings with a gradient in dimension from large central rings to small outer rings and simultaneously patterning interconnect lines and patterning vias for integrated circuits would require precise control over BCP morphology and domain size.

Specialized approaches have demonstrated the self-assembly of up to two distinct morphologies (*i.e.*, lines and dots) in a single film. One particularly interesting approach is to utilize direct photoinduced ordering. Daga *et al.* utilized a BCP-additive blend that was initially disordered, but, upon photoconversion of the additive, the blend spontaneously self-assembled.[68] Though, this approach is not easily generalizable as it requires the design of an additive with highly specific interactions to induce order in the BCP film. Onses *et al.* have demonstrated the use of electrohydrodynamic jet printing to directly print BCPs of various molecular weights and compositions.[12,69] However, ultrahigh resolution registration of differing BCP 'inks' for printing

of a continuous thin film is difficult. Furthermore, co-diffusion at the interface between printed BCP materials will lead to interfacial broadening during annealing.

Another more general approach is to utilize crosslinking of the BCP to fix structure in well-defined regions and modulate morphology or domain spacing in uncrosslinked regions. For example, Ober,[7,70] Ross,[6,71] and coworkers have used swelling of a single domain with a selective solvent vapor to perturb both the morphology and domain spacing away from equilibrium. Once the desired non-equilibrium morphology was formed, electron beam lithography was utilized to crosslink well-defined regions of the film. Morphology could then be modified again in uncrosslinked regions by a different solvent vapor to yield distinct morphologies in close proximity. However, only slight perturbations to self-assembled structure is possible by this method. He and Stoykovich also utilized selective crosslinking to deposit two BCP materials with different domain spacing in close proximity.[8] In this process, optical lithography was utilized to crosslink well-defined regions of an epoxide-functionalized BCP thin film. Unexposed regions could be removed and replaced with a second material with differing domain spacing or morphology. However, such multistep exposure-and-develop processes adds additional complexity and it would be desirable to modulate the morphology and domain spacing in an all-additive process. Despite the significant progress made by these specialized approaches, achieving diverse equilibrium nanostructures in contiguous regions of a continuous thin film in a high-throughput process remains a challenge.

2.2 Enzyme Nanostructures

2.2.1 Naturally Occurring Multienzyme Complexes

There are many important synthetic and metabolic pathways in nature which rely on multistep biotransformation reactions. Some enzymes involved in these pathways may have low substrate specificity and require a high local concentration of substrate to be effective as catalysts. However, some intermediates involved in such multistep pathways are highly reactive or toxic, requiring low global concentrations to prevent undesired side reactions or even cell death.[72–74] Furthermore, directing metabolic flux to specific pathways is critical for regulating redox potential, biosynthesis, and signal transduction in cells.[75]

As a result, there are many different techniques in biological systems to directly control the diffusion of intermediate compounds between active sites, referred to as substrate channeling, that result in high local concentration of intermediate compounds near the necessary enzymes without resulting in high global concentrations.[76] For example, tryptophan synthase is an $(\alpha,\beta)_2$ heterotetramer with a linear arrangement of subunits $\alpha/\beta/\beta/\alpha$. The α subunit first cleaves a carbon-carbon bond in indole 3-glycerol phosphate to produce indole which subsequently undergoes a condensation reaction with serine at the β subunit to form tryptophan. Interestingly, the active sites on α and β subunits are linked by a 2.5 nm intramolecular tunnel which facilitates direct transfer of the indole intermediate. Upon substrate binding, a lid closes over the α subunit and a rotation of the α subunit with respect to the β subunit restricts solvent access to the tunnel.[77,78] Similar tunnels are found in carbamoyl phosphate synthase,[79] glutamine phosphoribosylpyrophosphate amidotransferase,[80] asparagine synthase,[81] and others.[16] Such tunnels prevent diffusion of intermediate compounds to the bulk, which protects the intermediate from side reactions and also results in high local concentration of intermediate near the second active site.

Another common motif in nature is the metabolon, a noncovalent assembly of enzymes that work in concert to produce a product. One example is the Krebs tricarboxylic acid cycle (TCA) metabolon,[82,83] a complex of all eight Krebs cycle enzymes. Recent evidence[84] has confirmed theoretical predictions[85,86] that a highly positively charged domain is formed on the surface of at least the mitochondrial malate dehydrogenase-citrate synthase-aconitase subcomplex which connects the active sites of all three enzymes. As the intermediate compounds in the TCA cycle are highly negatively charged, attractive electrostatic interactions substantially increase the local concentration of intermediates near the active sites resulting in the improved sequential catalytic performance of the metabolon.[18] Other metabolons include the de novo biosynthesis of purine,[87,88] isoprenoids,[89] amino acids,[90] and flavonoids[91] as well as fatty acid oxidation[92] and the carboxysome.[93] While the specific molecular-level interactions leading to enhanced activity in each metabolon are not fully understood, it is likely that intermediates are channeled between active sites.

The above examples result from highly specific protein-protein interactions that give rise to new domains (*i.e.*, tunnels or electrostatic bridges) in the assembled enzyme or enzyme complex. Perhaps a more intuitively simple approach is the colocalization of multiple enzymes involved in a catalytic cascade mechanism onto a scaffold in the absence of direct substrate channeling between enzymes. One such example is the cellulosome, a hierarchical complex of cellulolytic enzymes found on the surface of some bacteria. The cellulosome consists of the scaffold protein, scaffoldin, which contains multiple cellulase-binding-domains termed cohesions, and various cellulases, which each contain a cohesin-binding-domain called a dockerin. The modular nature of cohesion-dockerin interactions allows for species-specific variations in the selection and ordering of enzymes immobilized to scaffoldin.[94,95] The end result is a multienzyme

complex allowing for the synergistic deconstruction of cellulose and hemicellulose to form glucose.[21] Additionally, mitogen-activated protein kinases (MAPKs) are arranged on scaffolding proteins. In a typical MAPK signaling pathway an upstream MAP kinase kinase kinase kinase (MAP4K) is activated which then stimulates a MAPK module consisting of three MAPKs (MAP3K, MAP2K, and MAPK) immobilized to a scaffolding protein. The activated module can then be transported to different regions of the cell to carry out different functional responses based on which scaffold is used. Interestingly, these scaffold proteins help to insulate the module from cross-talk or signal drift that may result from adjacent signaling pathways that utilize the same or similar signaling molecules. Furthermore, the close proximity of the components of the MAPK module allows for rapid signal transmission.[96]

2.2.2 Engineering Multienzyme Complexes

While important advancements have been made in *de novo* protein design and understanding protein-protein interactions,[97] the design of tunnels or electrostatic channeling domains in fully synthetic metabolons remain inaccessible as generalized techniques to improve activity in coupled enzyme cascade reactions. However, it is rather straightforward to design synthetic scaffolds that allow researchers to place enzymes in well-defined geometries. For example, Chen and coworkers took advantage of the cohesion-dockerin motif present in the cellulosome to assemble linear arrangements of artificial enzyme complexes on the surface of yeast cells.[20] Using this technique, they assembled alcohol dehydrogenase, formaldehyde dehydrogenase, and formate dehydrogenase on scaffoldin to produce an artificial methanol oxidation cascade. This was displayed on the surface of the cells and demonstrated a 5-fold increase in the rate of NADH production when compared to free enzyme. Furthermore, Dueber *et*

al. utilized synthetic protein scaffolds bearing interaction domains from metazoan signaling proteins to recruit enzymes labeled with their cognate peptide ligands.[98] As a result, a three-enzyme cascade was immobilized to the scaffold resulting in a 77-fold increase in mevalonate production in *E. coli*.

2.2.3 Proximity Channeling

In principle, such scaffolding techniques do not result in any form of direct substrate channeling, such as is present in intramolecular tunnels or electrostatic domains. Rather, observed activity enhancements in enzyme cascades immobilized to scaffolds have generally been explained in terms of 'proximity channeling,' where a shorter distance between the active sites of coupled enzymes leads to faster transfer of the intermediate substrate and therefore enhanced activity of the cascade. Therefore, it is interesting to consider what role distance between active sites plays in determining the overall activity of an enzyme cascade. In particular, DNA origami (*i.e.*, the folding of DNA to create well-defined nanostructures) has been used to coimmobilize glucose oxidase (GOx) and horseradish peroxidase (HRP) while systematically controlling the inter-enzyme distance. In this enzyme cascade, GOx first uses oxygen to oxidize glucose, producing glucono-δ-lactone and hydrogen peroxide (H_2O_2), followed by the oxidization of another substrate (commonly 2,2'-azino-bis(3-ethylbenzothiazoline-6-sulfonic acid) (ABTS)) with H_2O_2 by HRP. By taking advantage of DNA origami, Fu *et al.* created individual GOx/HRP pairs on DNA tiles with six inter-enzyme distances ranging from 10 nm to 65 nm.[27] A several-fold rate enhancement was observed for every inter-enzyme distance compared to free enzyme, however, activity was strongly inversely correlated with inter-enzyme distance. The largest activity enhancement of ~15-fold over free enzyme was observed for enzymes with 10 nm spacing while an activity

enhancement of only ~2.5 was observed for enzymes with 65 nm spacing. In a similar technique, Wilner *et al.* tethered GOx and HRP to a DNA origami ribbon with a precisely controlled distance between GOx-binding and HRP-binding domains.[99] When separated by a 6 nm distance, a 16-fold rate enhancement was observed over free enzymes in solution at the same concentration. On increasing the distance from 6 nm to 17 nm only a small activity loss was observed as the cascade maintained ~83% activity compared to the 6 nm separation. In both of these cases the dependence of activity on inter-enzyme distance was interpreted as being the result of proximity channeling.

Consider an isolated pair of two enzymes, such as GOx and HRP, immobilized to a scaffold. The probability that H_2O_2 diffuses directly to HRP before diffusing off into bulk solution scales as $P \propto R_{HRP}/r$ where P is the probability of encountering HRP, R_{HRP} is the radius of HRP, and r is the inter-enzyme distance (while the naïve assumption is that the probability should scale with $1/r^2$ due to the solid angle subtended by the origin and HRP, Howard C Berg discusses this in detail in his excellent book Random Walks in Biology[100]). However, this means that the probability that H_2O_2 diffuses from GOx into the bulk solution is proportional to $1 - R_{HRP}/r$, and so over time the concentration of H_2O_2 builds up in bulk solution. Therefore, the total flux of H_2O_2 diffusing to HRP can be divided into two components: H_2O_2 diffusing directly from GOx proportional to R_{HRP}/r and H_2O_2 diffusing from the bulk solution proportional to $1 - R_{HRP}/r$. At short times the concentration of H_2O_2 in the bulk solution is low, so the flux of H_2O_2 diffusing directly from GOx dominates and there is a significant rate enhancement for cascades with shorter inter-enzyme distances. Eventually the majority of the total flux of H_2O_2 going to HRP comes from the bulk and all benefit from proximity of GOx to HRP is lost. Idan and Hess explored this effect in detail and estimated the time over which a benefit may be observed as $t = V/4\pi Dr$, where V is the total reaction volume and D is the diffusion constant of the intermediate.[101]

Importantly, the presence of competing side reactions prevents the buildup of intermediates in bulk solution. For example, in the crowded and complex environment of the cell, most intermediates will be consumed by side reactions. In this case, the flux of intermediates diffusing directly from the first enzyme to the second enzyme always dominates over the flux of intermediates from bulk solution. Therefore, colocalization of enzyme cascades in vivo, such as the above-mentioned examples of Chen and Dueber, can still be an effective way to improve overall activity of cascade reactions. Though in the case of GOx/HRP enzyme pairs immobilized to DNA scaffolds, there are no competing side reactions. Yet, Fu and Wilner demonstrated long-lived rate enhancement of greater than an order of magnitude by colocalizing the enzyme pairs on DNA scaffolds. To address this discrepancy, Zhang *et al.* proposed that the negatively charged DNA scaffolds alter the pH in the near-enzyme environment, altering the inherent kinetics of GOx and HRP.[26] The pH near the surface of the negatively charged DNA structures is lower than in bulk solution due to the attraction of positively charged protons, a phenomenon which has been well-understood for decades.[102] Both GOx and HRP have pH optima at lower pH than that used by Fu (pH 7.5) or Wilner (pH 7.4), possibly explaining the rate enhancement of the cascade reaction on DNA scaffolds.

While proximity effects may not have a significant effect on the maximum cascade throughput for isolated enzyme pairs, Idan,[103] Castellana,[104] Buchner[105,106] and coworkers have concluded that there may be long-lived effects to colocalization of enzymes in densely packed systems. The presence of many enzyme targets in close proximity may reduce the probability that intermediate molecules make it into bulk solution, and potentially leads to long-term or even permanent rate enhancement. Furthermore, it is unclear how the distribution of enzymes (*i.e.*, geometric arrangement) can be used to further drive long-lived activity enhancements in enzyme

cascades. While reaction-diffusion models have been developed in attempts to study such effects, they treat the enzymes as a continuum with a homogeneous density defined by the enzyme concentration in the bulk, and therefore are unable to capture the behavior of inhomogeneous enzyme distributions that arise in enzymatic cascades immobilized in well-defined spatial arrangements. Therefore, a model that treats enzymes and intermediate molecules as discrete entities could provide important insights and elucidate the role of local density and spatial arrangement of coupled enzymes on the rate of product formation.

2.3 Tuning Enzyme-Solvent Interactions

2.3.1 Enzymes in Non-Native Solvents

Enzymatic biocatalysis in non-native solvent environments presents exciting opportunities in organic synthesis. Utilizing non-aqueous solvents prevents contaminating bacterial growth, avoids side reactions of water-sensitive compounds, increases the solubility of hydrophobic substrates, shifts chemical equilibrium to allow synthesis of compounds that may not be favorable in water, and, because enzymes are generally insoluble in non-aqueous media, they can be readily collected by filtration and recycled.[28,107] Furthermore, when suspended in the organic solvent, the insoluble enzyme can withstand extreme temperatures.[108] The solvent environment has even been shown to effect substrate specificity and enantioselectivity of enzymes.[109] There is substantial evidence that the structure and catalytic mechanism of enzymes is independent of the solvent environment[110–113] and so the altered stereoselectivity of enzymes in organic solvents has been attributed to altered protein dynamics in such solvents[114,115] while altered substrate specificity is explained by changes to thermodynamics of substrate binding in various solvents.[109] Therefore,

engineering the solvent environment for biotransformations provides a great deal of control over the end product.

Ionic liquids (ILs), which consist only of ions and are liquid below 100 °C, are of particular interest as solvents for biotransformations.[30,116,117] Often considered to be green solvents, ILs are non-volatile, thermally stable, and are good solvents for a wide range of compounds.[118,119] Interestingly, the physical and solvent properties of ILs can be tuned by changing the cation/anion pairing enabling solvent engineering as an additional technique to modulate enzyme function. While various enzymes have been used in ILs, such as oxidoreuctases[120–122] or lyases,[123] hydrolases are by far the most widely used for organic synthesis in ionic liquids with applications including chromatography-free racemic resolution of alcohols,[124–126] enantioselective transesterification,[127] and enantioselective acylation.[128–130] Hydrolytic enzymes have shown interesting properties in hydrophobic ionic liquids such as enhanced activity[31,32,130] and stability[33,131] compared to other organic solvents. For example, Persson and Bornscheuer found that esterase from *B. stearothermophilus* had a half-life of 8 hours in hexane but retained 100% activity after 10 days in the hydrophobic ionic liquid 1-butyl-3-methylimidazolium hexafluorophosphate ([BMIM][PF_6]).[33]

2.3.2 Improving Enzymatic Performance: Achieving Homogeneous Biocatalysis in Non-Native Solvents

In aqueous solution, enzymes fold as a result of intramolecular forces including the hydrophobic effect (in which proteins fold to from a hydrophobic core), polar interactions, and electrostatics. By putting a folded enzyme in a non-native solvent, the balance of intramolecular forces can be significantly impacted. Typically, folded enzymes have hydrophilic (*i.e.*, polar or charged) residues on the surface which have highly unfavorable interactions with hydrophobic

organic solvents. However, the low dielectric environment of the hydrophobic solvent increases the thermodynamic stability of intramolecular polar and electrostatic interactions on the surface of the enzyme which leads to structural rigidity.[132] Interestingly, this is true even in ILs – despite their ionic nature, many ILs form low-dielectric environments.[133] This increased structural rigidity helps explain the above-mentioned observation that many enzymes have enhanced stability in non-native solvent environments. Unfortunately, interactions between enzyme and solvent molecules are not always thermodynamically favorable and enzyme phase separation is a common problem in most solvents.[134] While the enzyme can be suspended in the solvent as a dried powder, this effectively reduces the concentration of enzyme that is accessible to substrate and results in lower enzyme activity. Therefore, to expand the utility of enzymes in non-native solvents it is of interest to consider methods to improve enzyme solubility.

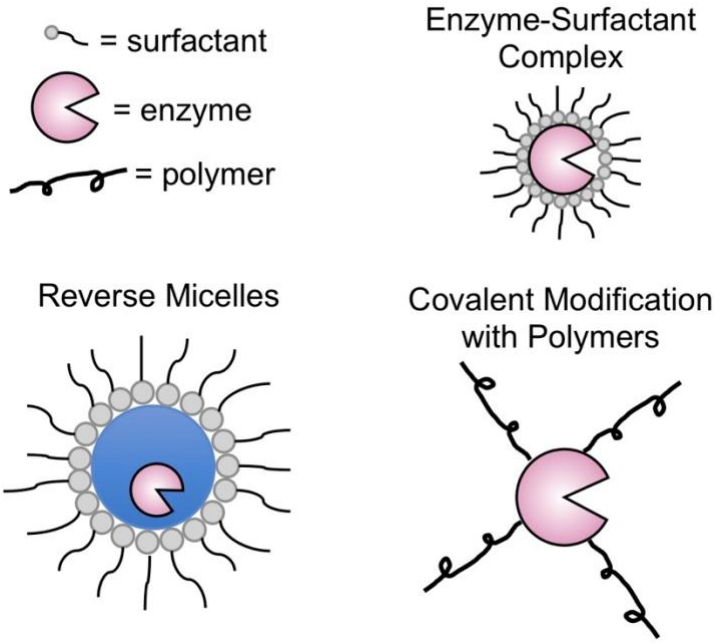

Figure 2.4 Schematic representation of three strategies to improve enzymatic activity in non-native solvents.

Perhaps the most obvious answer is to utilize a biphasic system where the enzyme is maintained in a reverse micelle.[135–137] The water-immiscible solvent then serves as a reservoir for hydrophobic substrates and products while preserving known enzyme function inside the aqueous micelles. However, this approach maintains the enzyme in an aqueous phase making anhydrous reactions impossible and this approach can only be used in water-immiscible solvents. Furthermore, the presence of high concentrations of surfactant and large interfacial surface areas can lead to enzyme inactivation.[138]

A more generalizable approach is the use of enzyme-surfactant complexes.[139–144] A typical preparation results from mixing of the enzyme with a surfactant in aqueous solution followed by precipitation or lyophilization of the noncovalent enzyme-surfactant complex to remove water. The powder can then be dissolved in the solvent of choice. For example, Goto *et al.* utilized the nonionic surfactant glutamic acid dioleyl ester ribitol amide to form surfactant-coated lipase.[139] They then compared the activity of lipase from *Pseudomonas* sp. by measuring esterification of lauric acid and benzyl alcohol in isooctane under three conditions: when suspended as lyophilized powder, in reverse micelles, and in a soluble surfactant complex. The surfactant complex of lipase had significantly higher activity, reaching nearly 100% conversion in under 30 minutes compared to the suspended powder which took 3 days to reach 90% conversion. Interestingly, the reverse micellar system leveled off after 40 minutes at less than 50% conversion, suggesting that the presence of water in the reverse micelles prevented complete esterification, likely due to a competing hydrolysis reaction in the presence of water. Surfactant complexes of five different lipases showed large activity enhancement over suspended lyophilized powder of each enzyme. Similar techniques have been used to study horseradish peroxidase,[141,142] myoglobin,[143] and glucosidase[144] in various non-aqueous solvent environments. However, the noncovalent nature of

such complexes presents a challenge for use in a continuous process as surfactant could dissociate from the enzyme surface leading to enzyme aggregation and inactivation.

Instead, the covalent attachment of amphiphilic polymers to enzymes forming enzyme-polymer conjugates presents a promising approach to improve enzyme solubility and activity in non-native solvents. There are a number of advantages to covalent modification of the enzyme with the solubilizing polymer. First, the polymer will not dissociate from the enzyme. As a result, enzyme-polymer conjugates are in principle recyclable whereas enzyme-surfactant complexes may not be. Second, covalent attachment enables the formation of enzyme-polymer conjugates with polymers that do not form strong interactions with the enzyme, greatly increasing the scope of possible polymer chemistries that can be used. In the case of surfactant complexes, the surfactant must interact strongly with at least portions of the enzyme surface in aqueous solution or no complex is formed. These strong interactions can lead to enzyme inactivation. Third, specific amino acid residues on the surface of the enzyme can be targeted for covalent attachment of the polymer. This precise control stands in contrast to the poorly understood noncovalent interactions leading to enzyme-surfactant complex formation.

Selecting a polymer that is highly soluble in a given solvent will drive the resulting enzyme-polymer conjugate into solution. For example, Castillo *et al.* showed that covalent attachment of poly(ethylene glycol) (PEG) to subtilisin Carlsberg increased enzyme activity in 1,4-dioxane by up to two orders of magnitude which correlated with increased structural dynamics of the enzyme-PEG conjugate as measured by hydrogen-deuterium exchange.[145] At increasing levels of functionalization (*i.e.*, more PEG molecules per enzyme) both activity and structural dynamics increased, indicating that the enzyme became more solvated with more polymer chains per enzyme. Though, interestingly, the enantioselectivity of a transesterification reaction was

reduced for the enzyme-polymer conjugate, likely a result of the increased structural flexibility of the conjugate. Konieczny *et al.* demonstrated that the covalent attachment of various poly(2-oxazoline) derivatives could solubilize 14 different enzymes in various solvents including THF, chloroform, toluene, DMF, methanol, and ethanol.[146,147] While many of the enzymes were deactivated by covalent attachment of the polymer, lipase B from *Candida antarctica*, laccase, horseradish peroxidase, and α-chymotrypsin all showed activity enhancement in organic solvents compared to the unmodified enzyme, which was suspended as lyophilized powder in the given solvent. Cummings *et al.* demonstrated the use of poly(2-(dimethyl amino)ethyl methacrylate) to solubilize α-chymotrypsin in acetonitrile and dichloromethane, as characterized by dynamic light scattering.[148] The enzyme-polymer conjugate exhibited good substrate binding with water-like K_M values in acetonitrile. In addition, enzymatic activity of the enzyme-polymer conjugate was more than two orders of magnitude greater than the unmodified enzyme in acetonitrile. It was interpreted that the molecular solubility of the enzyme-polymer conjugate resulted in tighter binding of the substrate and increased activity. Nakashima *et al.* reported that covalent crosslinking of subtilisin with a branched PEG derivative enhanced the solubility of the enzyme in various imidazolium ILs.[149,150] Though the attachment of linear PEG was significantly less effective[149] and linear PEG has proven ineffective in solubilizing enzymes in other ILs.[31]

Controlled radical polymerization techniques, such as atom transfer radical polymerization (ATRP) or reversible addition fragmentation chain transfer (RAFT), allow for straightforward synthesis of linear polymers with conserved chain ends.[151] Therefore, polymers can be synthesized with chemical groups on the inactive chain end, such as the amine-reactive N-hydroxysuccinimide ester. Alternatively, the active chain end can be utilized for post-polymerization modification. For example, RAFT chain transfer agents (CTAs) can be cleaved to expose a thiol which can be

coupled to an enzyme by disulfide exchange or reacted to heterobifunctional linkers containing a maleimide group. This results in a reactive polymer which can be reacted with the enzyme in an approach often referred to as 'grafting-to.'[152] In this approach, the polymer can be synthesized using traditional methods in organic solvents and the polymer product is easily characterized. However, steric hindrance can limit the number of polymers per enzyme (*i.e.*, the grafting density of polymer chains).

Alternatively, the CTA or ATRP initiator can be covalently attached to the enzyme prior to polymerization, enabling a 'grafting-from' approach in which the polymer is grown from the enzyme surface.[153] In this approach the grafting density can be significantly increased over grafting-to. However, often the polymerization must be conducted in water due to limitations in enzyme solubility. Furthermore, characterization of the resulting polymer is difficult, and may necessitate digestion of the enzyme to release free polymer for characterization. Finally, some enzymes are sensitive to the high monomer concentration or the presence of radical species near the enzyme surface which can lead to enzyme inactivation.

2.3.3 Polymers in Solution

To better understand how to rationally design an enzyme-polymer conjugate for enhanced enzymatic performance in non-native solvents, let's first consider the solubility of polymers in dilute solution. As is the case in BCP self-assembly, the Flory-Huggins interaction parameter, χ, is an important parameter when discussing polymer solubility in solution. First derived from a lattice model, χ quantifies the change in free energy resulting from contact dissimilarity between polymer repeat units and solvent molecules:

$$\chi = \frac{(z-2)\Delta\varepsilon_{12}}{k_b T}$$

where z is the number of lattice sites and $\Delta\varepsilon_{12}$ is the interchange energy, $\Delta\varepsilon_{12} = \varepsilon_{12} - \frac{1}{2}(\varepsilon_{11} + \varepsilon_{22})$ where ε_{ij} is the contact energy of species i and j. Based on this lattice model, the free energy of mixing for a polymer is simply:

$$\Delta G_m / k_B T = N_1 \, ln \, \phi_1 + N_2 \, ln \, \phi_2 + N_1 \phi_2 \chi$$

where N_1 and ϕ_1 are the number and volume fraction of solvent molecules and N_2 and ϕ_2 are the number and volume fraction of polymer chains. The first two terms result from the entropy of mixing while the final term is the result of enthalpic contributions. Since both N_1 and ϕ_2 are positive quantities, large values of χ lead to large positive contributions to ΔG_m and smaller values of χ will result in polymers with more thermodynamically favorable mixing with the solvent (*i.e.*, more soluble). Then, by taking the partial derivative with respect to N_1 and a few algebraic maneuvers, we can write the chemical potential as:

$$\frac{(\mu_1 - \mu_1^0)}{k_B T} = -\left[\frac{\phi_2}{x} + \left(\frac{1}{2} - \chi\right)\phi_2^2\right]$$

where x is the number of repeat units in the polymer. Since χ is related to the excess chemical potential, it can be calculated using techniques that directly measure excess chemical potential such as static light scattering. The intensity of scattered light at a fixed angle, θ, can be described by the following equation:

$$\frac{KC}{R_\theta} = \frac{1}{M_W} + 2A_2 C$$

where R_θ is the excess Rayleigh ratio, C is the polymer concentration, M_W is the weight-average molecular weight of the polymer, A_2 is the second virial coefficient, and K is a constant defined by:

$$K = \frac{4\pi^2 n_0^2 (\frac{dn}{dc})^2}{N_A \lambda_0^4}$$

where n_0 is the index of refraction of the solvent, n is the index of refraction of the solution containing solute, λ_0 is the wavelength of incident laser light, and N_A is Avogadro's number. The Flory-Huggins interaction parameter, χ, can then be calculated from the expression:

$$\chi = \frac{1}{2} - \frac{\bar{V}_s}{\left(\rho_p^0\right)^2} A_2$$

where ρ_P^o is the density of the polymer, $\bar{V}_S$ is the partial specific volume of solvent, and A_2 is the second virial coefficient.

This simple theory can be used to predict equilibrium phase behavior of the polymer in the solvent. The critical value of the interaction parameter, χ_C, at which phase separation will be thermodynamically favored can be determined by setting the first, second, and third derivatives of the chemical potential to zero resulting in:

$$\chi_c = \frac{1}{2} + \frac{1}{\sqrt{x}} + \frac{1}{2x}$$

This reveals that as the polymer gets very large (*i.e.*, as $x \to \infty$), $\chi_c \to \frac{1}{2}$. Therefore, the interaction parameter is a quantitative measure of solvent quality. When χ is near or above ½ the solvent is of poor quality for the polymer and when χ is significantly less than ½ the solvent is said to be a good solvent.

Given the simplicity of Flory-Huggins theory, it shouldn't be surprising that there are many limitations. Our end goal is to covalently attach polymers to the surface of enzymes as a means to improve solubility of the entire enzyme-polymer conjugate. So, let's consider the limitations of Flory-Huggins theory in this context. We must first recognize that an enzyme-polymer conjugate is a very complex, semi-structured copolymer. This significantly complicates our calculation of

the contributions to entropy on mixing from the polymers, as one end of each polymer chain is tethered to the structured enzyme component which reduces the number of available states for the polymer. Secondly, Castillo *et al.* have demonstrated that attaching polymer chains to an enzyme can alter the enzyme dynamics,[145] which would impact our calculations of contributions to entropy of mixing from the enzyme in an unspecified way that, based on their results, is clearly dependent on the number of attached polymer chains and presumably on the molecular weight of each polymer chain. Furthermore, χ is assumed to be concentration-independent, which is probably not a big problem in dilute solutions of soluble polymers which will have a relatively homogeneous distribution of polymer chains throughout the solution. However, when one chain end is attached to the surface of the enzyme, there is a strong concentration gradient of polymer segments as a function of distance from the surface.[154] This is caused by the convex curvature of the surface: the volume per polymer chain increases as a function of distance from the surface, which results in lower polymer concentration. Finally, specific polymer-solvent, polymer-enzyme, enzyme-solvent, and higher-order interactions are not accounted for.

Such limitations to Flory-Huggins theory mean that *a priori* estimation of an effective interaction parameter, χ_{eff}, between the enzyme-polymer conjugate and solvent is unlikely to be accurate. However, by measuring χ of the polymer in the selected solvent, we can begin to understand how our choice of polymer will impact the solubility of the conjugate. Specifically, to solubilize an insoluble enzyme, we want to choose a polymer with χ significantly below ½ to compensate for the unfavorable enzyme-solvent interactions. This means choosing a polymer made from monomers with highly favorable interactions with the solvent. Furthermore, from the lattice model it is obvious that the total contribution to free energy of mixing from polymer-solvent contacts is proportional to the number of those contacts. So, in a more qualitative sense, increasing

the proportion of conjugate-solvent interactions which are favorable by increasing the number of polymers per enzyme or increasing polymer length should improve the total thermodynamic favorability of conjugate dissolution. This is supported by the observation that the structural dynamics of subtilisin in 1,4-dioxane correlated with the number of soluble polymers per enzyme.[145]

2.3.4 Improving Enzyme Processability: Stimuli-Responsive Polymers to Leverage Homogeneous and Heterogeneous Biocatalysis

In non-native solvents enzymes are traditionally used as heterogeneous catalysts, which facilitates their separation and recycling, by simply suspending the lyophilized powder or immobilizing the enzyme to a solid support such as a particle or resin. To enhance the utility of enzymes for chemical transformations in non-native solvents, one would ideally wish to combine the activity of a homogeneous biocatalyst with the ease of separation of a heterogeneous biocatalyst. One way this can be realized is by modifying the enzyme with stimuli-responsive polymers that undergo significant changes to χ as the result of the application of an external stimulus. In this approach, the thermodynamic interactions between the enzyme-polymer conjugate and solvent may be tuned using an external 'switch' to turn solubility on or off based on such changes to χ.

Polymers may be designed to respond to many external stimuli such as light,[155–157] pH,[158,159] or ionic strength,[160] though the most common technique is to utilize thermoresponsive polymers. In principle, all polymers are thermoresponsive, meaning that the miscibility of the polymer in a given solvent is temperature-dependent. This is because, while χ was first derived as a temperature-independent enthalpic contribution to free energy, χ is actually itself a free energy

term and can be approximated as $\chi = A + B/T$ where A and B are constants. A phase diagram can then be constructed by measuring the temperature at which phase separation is observed (*i.e.*, the cloud point) as a function of polymer concentration, as shown schematically in **Figure 2.5**. When B is positive, χ is inversely proportional to temperature and the maximum of the cloud point curve is referred to as the upper critical solution temperature (UCST) (**Figure 2.5a**). This means that the polymer will only be soluble at temperatures above the phase boundary. When B is negative, however, this relationship is reversed, and the minimum of the cloud point curve is referred to as the lower critical solution temperature (LCST) such that the polymer is soluble at temperatures below the phase boundary (**Figure 2.5b**).

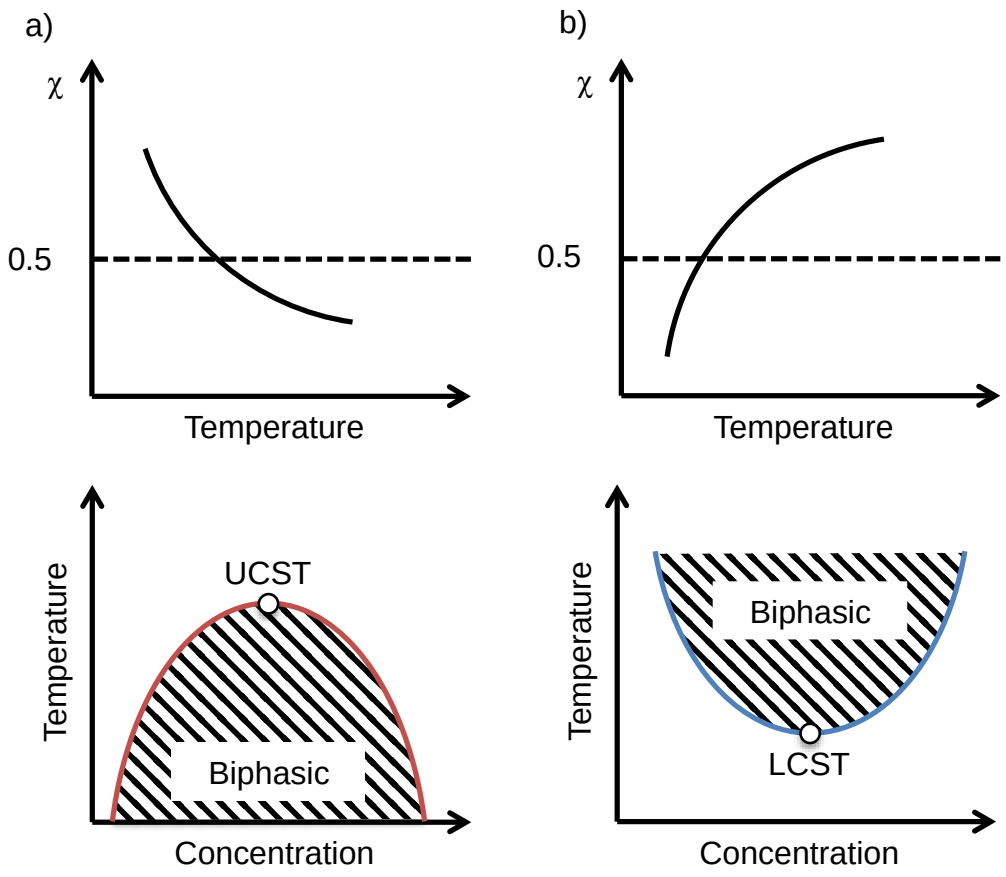

Figure 2.5 Schematic representation of the temperature dependence of χ and representative phase diagrams. a) UCST-type phase behavior results when χ decreases with temperature. b) LCST-type phase behavior results when χ increases with temperature.

UCST-type phase behavior is relatively simple to make sense of given the simple equation for the free energy of mixing:

$$\Delta G_m = \Delta H_m - T\Delta S_m$$

Since the entropic component is typically positive and weighted by T, the solubility of the polymer depends mainly on the magnitude of ΔH_m, which is also normally positive. So, as temperature is lowered, the favorable contributions from the entropic term become smaller and phase separation will occur, resulting in UCST-type phase behavior. However, in specific examples the change in entropy on mixing is actually negative, making the entropic component to free energy unfavorable.

For example, poly(N-isopropyl acrylamide) in water exhibits LCST-type behavior. The structuring of water molecules around the hydrophobic isopropyl group leads to loss of entropy on solvation. However, hydrogen bonding between the amide group and water provides favorable enthalpic interactions. So, as temperature is increased, the unfavorable entropic term dominates, and phase separation is observed. Another example is poly(benzyl methacrylate) in the ionic liquid 1-ethyl-3-methylimidazolium bis(trifluoromethanesulfonly)imide. The LCST-type behavior is attributed to $\pi - \pi$ stacking of the positively charged aromatic imidazolium rings with the benzyl group from the polymer side chain, which lead to unfavorable loss of entropy on solvation.[161] While these examples are the result of highly specific intermolecular interaction between polymer side chain and solvent, LCST-type behavior is actually commonly observed when approaching the critical temperature of the solvent. This can be rationalized by considering that solvation of the polymer requires solvent molecules to condense on the polymer. As temperature increases and the solvent expands, the entropic penalty of solvation becomes too great and eventually solvation is entirely entropically unfavorable.

By covalently modifying enzymes with thermoresponsive polymers, the enzyme may be miscible in the reaction solvent at the desired temperature for reaction, and yet be readily separated by changing the temperature. There are many examples of this approach for enzymatic biotransformations in aqueous solution.[162–169] However, there are very few examples in organic solvents. As proof-of-concept, Liu and co-workers[170–173] modified cytochrome c and various lipases with Pluronic, a commercially available thermoresponsive poly((ethylene oxide)-*block*-(propylene oxide)-*block*-(ethylene oxide)) triblock copolymer, which facilitated solubilization and recycling of the enzymes due to the UCST-type phase behavior of Pluronic in some organic solvents. When solubilized, each enzyme-polymer conjugate was more than an order of magnitude

more active than the unmodified form of the enzyme and was successfully recycled multiple times. In this approach, the enzyme-polymer conjugate was dissolved in toluene and recycled via cooling the sample from 40 °C to 4 °C at which temperature the conjugate precipitated. This approach was also explored in acetonitrile and methyl isobutyl ketone, although the enzyme-polymer conjugate could only partially be recovered from acetonitrile. This is because the Pluronic used to make the conjugates will have a different χ in acetonitrile compared to toluene. While these examples highlight the potential utility of this approach, the scope of solvent environments in which these approaches were demonstrated was narrow. Furthermore, the extent to which χ may be rationally tuned was not fully explored. Therefore, it is interesting to consider how tuning polymer chemistry may enable the orthogonal benefits of homogeneous and heterogeneous biocatalysis in non-native solvents.

Chapter 3: Objective and Specific Aims

3.1 Objective

The objective of this work was to utilize polymeric materials for bottom-up self-assembly of nanostructured surfaces and functionalize catalytically active enzymes for improved performance and recyclability in non-aqueous media. The first aim of this work was to develop a simple process to allow for quantitative control over both domain size and morphology of equilibrium nanostructures self-assembled from block copolymer phase separation in thin films. Using the resulting nanostructured thin films as inspiration, the effect of nanopatterning enzymes that form a cascade reaction was explored. Whereas surface-immobilized enzymes have promising applications, the use of enzymes as homogeneous biocatalysts, *i.e.* when dissolved in bulk solution, is generally more attractive for use in chemical synthesis. Enzymatic biotransformations in organic solvents are of particular interest, but the effectiveness of enzymes in organic solvents is limited due to phase separation of enzymes in such solvents. Therefore, building off the expertise developed from studying block copolymer phase separation, enzymes were covalently modified with polymers to tune their solubility, and therefore activity, in non-aqueous solvents. Finally, the enzyme-polymer conjugates were made highly temperature sensitive by covalent modification with thermoresponsive polymers. A method to quantitatively tune the phase behavior of such thermoresponsive enzyme-polymer conjugates was then demonstrated.

3.2 Specific Aims

3.2.1 Aim 1: Develop and Evaluate a Facile Method to Spatially Control the Self-Assembly of Block Copolymer Materials

Enabling spatial control over morphology and domain spacing in phase-separated block copolymer thin films would allow the fabrication of complex nanoscale devices by block

copolymer lithography. We have addressed multiple challenges in this area. First, we developed a simple layer-by-layer technique to quantitatively control both the domain size and the morphology of equilibrium nanostructures in self-assembled block copolymer thin films. Importantly, mixing of a small number of polymeric components allows the domain size to be tuned across a continuum. Second, we show that such equilibrium nanostructures can be fixated in arbitrary regions of the film as defined by 365-nm optical lithography. Contiguous regions of lines and dots with varying domain spacing are demonstrated in a continuous thin film. Third, we characterize the mixing and lateral transport of polymeric materials in the multilayer blending process.

3.2.2 Aim 2: Elucidate the Role of Dimension and Spatial Arrangement of Enzymes on the Activity of Coupled Biocatalytic Reactions on Structured Surfaces

Using the nanostructures from aim 1 as inspiration, the effects of nanoscale patterning of enzymes involved in coupled biocatalytic reactions were explored numerically. Monte Carlo simulations were used to track the molecular trajectories of the reaction species and to investigate the turnover frequency of individual enzymes on the surface. Diffusion-limited and reaction-limited conditions were considered for the various spatial arrangements of enzymes inspired by morphologies accessible by block copolymer self-assembly. In addition to the geometric arrangement, the density of enzymes was varied on the surface to explore effects of inter-enzyme distance on cascade activity.

3.2.3 Aim 3: Synthesize Covalent Enzyme-Polymer Conjugates and Apply them in Improving Enzymatic Biocatalysis in Ionic Liquids

The utilization of enzymes in ionic liquids has attracted a great deal of attention due to the unique solvent properties of ionic liquids. However, enzymes are generally poorly soluble in ionic liquids which significantly reduces enzymatic activity. We hypothesized that covalent

modification of enzymes with ionic liquid-soluble polymers would enhance enzyme solubility, and therefore activity, in ionic liquids. This hypothesis was tested using the understanding of phase separation developed in aim 1. Ionic liquid-soluble polymers were used to solubilize enzymes and explore the effects of solubilization on enzymatic activity. Light scattering techniques were then used to measure molecular-level interactions between the polymer and ionic liquid as well as to study the effects of the covalently attached soluble polymer on the aggregation behavior of the enzyme-polymer conjugate. These results were used to understand the mechanism of activation of the enzyme in the ionic liquid.

3.2.4 Aim 4: Tune Molecular-Level Interactions Between Enzyme-Polymer conjugates and Solvent to Enable Recyclability of Enzymes Catalysts

One of the main benefits of utilizing heterogeneous catalysts is the ease of catalyst recycling. Whereas enzyme activity was significantly enhanced in aim 3 by covalently modifying the enzyme with soluble polymers, the resulting homogeneous biocatalyst could not be recycled. It was therefore beneficial to control the phase behavior of the biocatalyst in the solvent. The enzyme-polymer conjugates were made highly temperature sensitive by utilizing a polymer with an upper critical solution temperature (UCST) in the ionic liquid over the temperature range of interest. The UCST was tuned quantitatively by copolymerization with an ionic liquid-soluble monomer, allowing the design of an enzyme-polymer conjugate that phase separated at the specified temperature. The enzyme-polymer conjugate was then collected by precipitation or extraction into aqueous solution. Importantly, enzymatic activity retention was demonstrated after precipitation cycling. Lastly, thermorevesible shuttling was demonstrated of the enzyme-polymer conjugate between ionic liquid and aqueous phases.

Chapter 4: Accessing the Spectrum of Block Copolymer Morphologies in Thin Films Through Facile and Localized Multilayer Self-Assembly

4.1 Abstract

Self-assembly at the molecular- and nanoscale-levels enables the facile preparation of periodic arrays of the constitutive building blocks. However, self-assembled structures are often too regular and the single-step preparation of nanostructures with diverse shapes and dimensions in close proximity, necessary for potential lithographic applications such as integrated circuits and zone plates, is impossible. We altered the morphology and domain spacing of self-assembled nanostructures in block copolymer blends utilizing a facile multilayer mixing method coupled with photolithography to locally control blend composition. Multilayer mixing of a small number of polymer components resulted in contiguous regions of lines and dots of varying domain spacing. The ability to pattern diverse nanostructures in close proximity in a simple layer-by-layer process provides exciting opportunities for nanofabrication.

4.2 Introduction

Block copolymer lithography in thin films has developed into a potential replacement for top-down optical photolithography for nanopatterning at sub-22 nm dimensions[174]. Microphase separation of A-B diblock copolymers into ordered domains of A and B is driven by the thermodynamic minimization of free energy, which causes the material to spontaneously adopt extended periodic nanostructures that can be described by two simple parameters, χN and ϕ_A, where χ is the Flory-Huggins interaction parameter, N is the degree of polymerization, and ϕ_A is the volume fraction of the A block of the polymer.[40] Phase diagrams for many copolymer pairs have been characterized empirically,[41] or may be determined theoretically,[42] and typically consist of

spherical, hexagonally packed cylindrical, and lamellar ordered morphologies as well as a small window for a bicontinuous phase known as the gyroid.[40]

Standard implementations of block copolymer lithography use a single material in the thin film (*i.e.*, typically a pure diblock copolymer[175] or diblock copolymer blends[176,177]), and thus allow for self-assembly into only a single morphology with a regular structure and dimension specified by χN and ϕ_A. While this has shown promise in fabricating devices that rely on dense periodic arrays of nanoscale features such as magnetic bit patterned media[65,66] and multigate field effect transistors,[67] sometimes more control over the pattern geometries and dimensions is required lithographically. For example, Fresnel zone plates used to focus x-ray light consist of nanoscale concentric rings with a gradient in dimension from large central rings to small outer rings. Simultaneously patterning interconnect lines and vias for integrated circuits would prove equally challenging using a single block copolymer material. Specialized approaches have demonstrated the self-assembly of up to two distinct morphologies (*i.e.*, lines and dots) in a single film, although they rely on either a single material that switches between tunable non-equilibrium morphologies[6,70] or two materials deposited in a multistep exposure-and-development process[8]. Moreover, while advances in living polymerizations allow for very precise control over the molecular weight and volume fraction of each block, synthesizing a library of block copolymers to provide a continuum of self-assembled structures is prohibitive. Ultimately, alternative approaches that reduce both the number of processing steps and synthetic demands are required to fabricate diverse nanostructures in thin films from self-assembled block copolymers.

Here we introduce a facile layer-by-layer approach and materials to selectively tune the morphologies and dimensions of nanostructures self-assembled by block copolymers in spatially defined regions of a continuous thin film. The approach, as outlined in **Figure 4.1a**, uses the

sequential deposition and mixing of block copolymer and/or homopolymer layers to finely tune the composition of the self-assembling material. When combined with photolithographic techniques, spatially defined regions of specific self-assembled nanostructures are achieved. Specifically, to start the process, a block copolymer film of well-defined composition is prepared from a crosslinkable poly(styrene-*block*-(methyl methacrylate-*random*-glycidyl methacrylate)) copolymer (PS-b-ePMMA) via spin casting (Fig. 1a, Step 1)[8]. Solvent annealing is then used to rapidly self-assemble the block copolymer into its characteristic morphology, as defined by the copolymer composition (Step 2). Photo-initiated crosslinking of the epoxide functionalities in the block copolymer film in specific areas may be achieved by 365 nm optical lithography and used to locally fixate the nanostructures (Step 3). Subsequent layers of block copolymer, homopolymer, or homopolymer blends of polystyrene (PS) and poly(methyl methacrylate) (PMMA) may then be deposited, with volume fractions that either match or differ from that of the underlying block copolymer layers (Step 4 or 4', respectively). Upon sufficient annealing, the layers become mixed in the regions of the film that have not been fixated and the self-assembled morphologies adapt to the new locally–defined compositions (Step 5). In the crosslinked and fixated regions of the film, mixing does not occur and the nanostructure is not modified. This provides localized control over the block copolymer composition, therefore allowing for the self-assembly of diverse morphologies and dimensions in neighboring regions of the continuous film. Steps 3-5 may be repeated as many times as desired, until the structure of the entire film is fixated at which point no additional mixing may be accomplished.

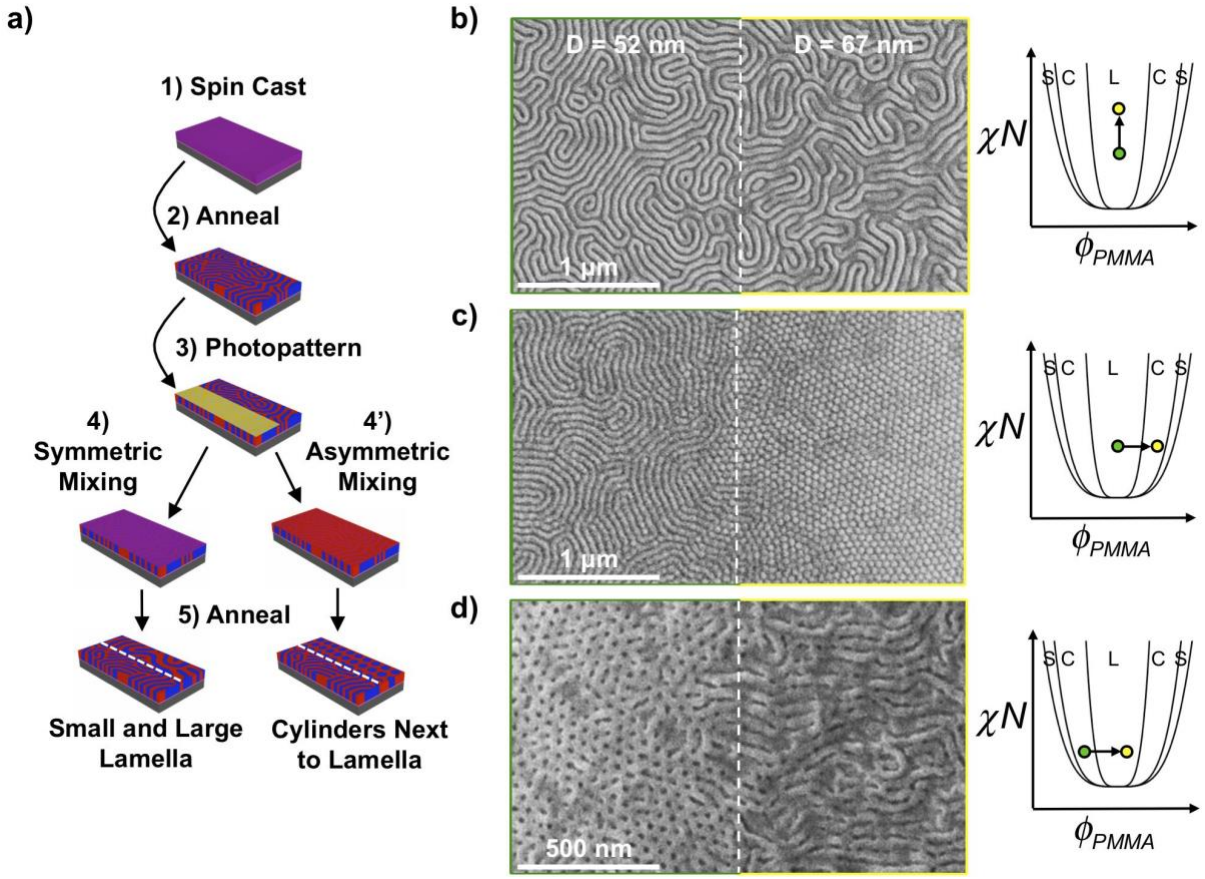

Figure 4.1 Multilayer mixing of block copolymer films to access the self-assembly of diverse morphologies and dimensions in neighboring regions. (a) Schematic illustration of the multilayer mixing process and materials. The block copolymer domains are shown in red while the second layer that is mixed into the structure may have a composition that matches (purple film in Step 4 using block copolymers or a blend of homopolymers) or differs (red film in Step 4' using a homopolymer) from that of the underlying phase separated film. (b-d) Scanning electron micrographs of continuous films of self-assembled PS/PMMA block copolymer materials with spatially diverse morphologies and dimensions formed by bilayer blending of a neat block copolymer with a symmetric blend of PS and PMMA (b), or just PMMA (c,d). The initial material and self-assembled structure is outlined in green, while the second structure self-assembled after localized blending is outlined in yellow. Schematic phase diagrams on the right illustrate the compositional and morphological transitions that are accomplished by the bilayer blending process, from the initial system in green to the blended system in yellow. The lamellar, cylindrical, and spherical phase windows are denoted as L, C, and S, respectively. The light and dark colors in the SEM images correspond to the PS and PMMA domains, respectively.

4.3 Results and Discussion

The top-down scanning electron microscopy (SEM) image in **Figure 4.1b** captures the self-assembled nanostructures accessed by the multilayer mixing of block copolymer systems with symmetric compositions (**Figure 4.1a**, Step 4). Crosslinkable PS-b-ePMMA (47-b-67 kg/mol, ϕ_{PMMA} = 0.56) was deposited as the first layer, while the second layer consisted of an equal volume

fraction of PS (20.8 kg/mol) and PMMA (21.2 kg/mol) homopolymers. The lamellar structure formed by the neat crosslinked PS-b-ePMMA had a domain spacing of 52 nm, as determined by 2D-FFT image analysis, and was fixed in specific locations in the film by photopatterning (left, outlined in green). During annealing the polymers were sufficiently mobile for the layers to mix in the uncrosslinked regions (right, outlined in yellow), resulting in the formation of ternary block copolymer-homopolymer blends of symmetric composition. The homopolymers partitioned into the corresponding block copolymer domains and, for the molecular weights used here, were preferentially excluded to the center of the lamellar domains.[55] The lamellar domains became swollen with homopolymer to a domain spacing of 67 nm, which is analogous to an increase in the effective degree of polymerization of the block copolymer (N), as illustrated schematically in the phase diagram of **Figure 4.1b**. Examination of the resulting equilibrium lamellar structures indicate that they are contiguous in the film and exhibit domain connectivity across the photolithographically defined boundary (indicated by the white dashed line).

The multilayer blending technique may also be applied to induce the self-assembly of diverse morphologies in a continuous thin film, as shown in **Figure 4.1c**. Mixing a lamellar-forming PS-b-ePMMA layer (47-b-67 kg/mol, ϕ_{PMMA} = 0.56) with a layer containing only PMMA (21.2 kg/mol), such that a blend with an asymmetric composition was produced (**Figure 4.1a** Step 4'), resulted in a lamellar to cylindrical phase transition in the uncrosslinked regions (**Figure 4.1c**, left→right). The cylindrical morphology has PS cylinders in a PMMA matrix because of swelling of the block copolymer structures with excess PMMA; similarly, blending of the base layer with a second layer of PS homopolymer may result in cylindrical morphologies of the opposite tone. Likewise, alternative starting points in the phase diagram may be used to access nanostructures with different morphologies and dimensions. **Figure 4.1d** demonstrates the application of a

crosslinkable cylinder-forming PS-b-ePMMA (49-b-17 kg/mol, ϕ_{PMMA} = 0.26) as the base layer that, upon blending with PMMA homopolymer from the second layer, transitions from a cylindrical to a lamellar structure. In these blends, the introduced homopolymer preferentially partitions into the PMMA domain of the block copolymer, thereby increasing the total volume fraction of the PMMA domain[55] and changing the interfacial curvature of the self-assembled structures.

The block copolymer compositions upon blending with the multilayer mixing method, as well as the resulting dimensions and self-assembled morphologies, are dependent on the relative thickness of each layer. Fortunately many approaches for the deposition of thin films with excellent control (sub-1 nm) over film thickness are available, including spin coating as used here. **Figure 4.2** characterizes the dimension and morphology changes elicited by the mixing of two distinct layers to yield self-assembling block copolymer blends of well-controlled composition. A 45 nm thick base layer of symmetric PS-b-ePMMA (47-b-67 kg/mol, ϕ_{PMMA} = 0.56) was used in each example and allowed to self-assemble into lamellar nanostructures. Without crosslinking the base layer, second layers composed of symmetric PS/PMMA homopolymer blends (**Figure 4.2a**), PS-b-PMMA copolymer (**Figure 4.2b**), or PMMA homopolymer (**Figure 4.2c**) were subsequently deposited and mixed until the new equilibrium morphologies were achieved.

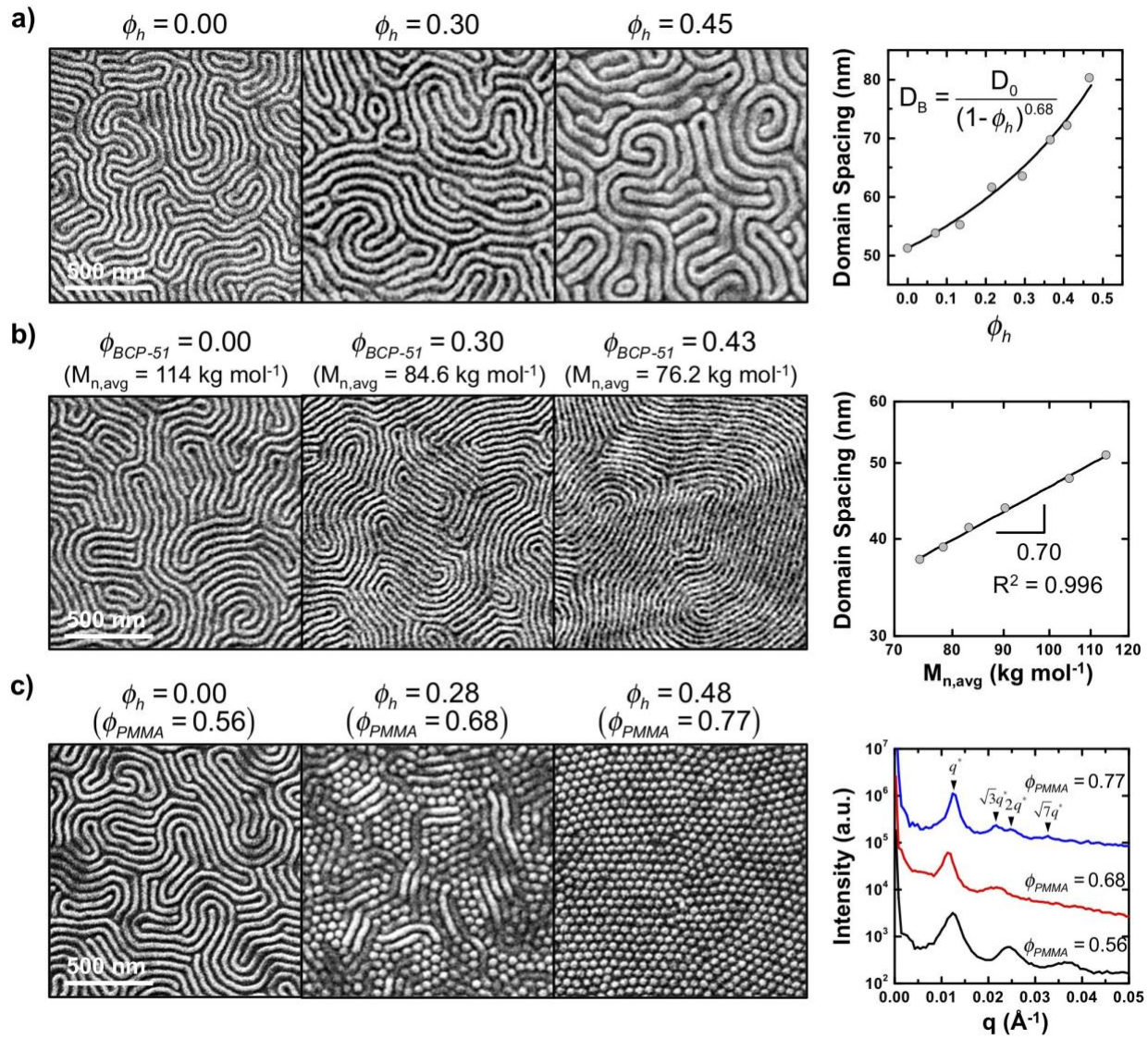

Figure 4.2 Continuous tuning of domain spacing and morphology by multilayer mixing. **(a)** Multilayer mixing of a lamellar-forming block copolymer with symmetric amounts of PS and PMMA homopolymers. SEM images are labeled with total volume fraction of added homopolymer, ϕ_h. The domain spacing, as measured from 2D-FFT analysis of SEM images, is a function of ϕ_h (R^2 = 0.987). **(b)** Multilayer mixing of lamellar-forming block copolymer (M_n = 114 kg/mol) with a smaller block copolymer (M_n = 51 kg/mol) of similar composition. Images are labeled with the volume fraction of added smaller block copolymer, ϕ_{BCP-51}, as well as the average molecular weight in the thin film. Domain spacing is a function of average molecular weight as presented on a log-log scale with best-fit line (R^2 = 0.996). **(c)** Multilayer mixing of lamellar-forming block copolymer with pure PMMA. Images are labeled with the volume fraction of PMMA homopolymer, ϕ_h, and total PMMA volume fraction in the thin film, ϕ_{PMMA}. Scattering profiles generated by 2D-FFT analysis of the SEM images are also included.

Performing symmetric blending with equal volume fractions of the corresponding PS/PMMA homopolymers, as in **Figure 4.2a**, produced lamellar structures with characteristic

dimensions (*i.e.*, domain spacings) dependent on total volume fraction of the added homopolymer blend, ϕ_h (**Figure 4.2a**). The lamellar domain spacing was determined by 2D-FFT analysis of the top-down SEM images and ϕ_h was calculated from ellipsometric measurement of the layer thicknesses. The domain spacing was increased from 52 nm to 80 nm by blending up to $\phi_h = 0.47$ without significantly altering the nanostructure morphology. In addition, the increase in lamellar spacing was well-described by the empirical relation from the literature:[57]

$$D_B = \frac{D_0}{(1-\phi_h)^\beta}$$

where D_B is the domain spacing of the ternary blend, D_0 is the domain spacing of the pure block copolymer system, ϕ_h is the total volume fraction of homopolymer in the blend, and β is linearly dependent on the ratio of molecular weights of the block copolymer and homopolymer.[57] For the system blended here, β = 0.68 as indicated by the best-fit curve in the plot in **Figure 4.2a**, which is consistent with values reported in the literature (β = 0.69)[57] for similar ternary blends self-assembled in thin films deposited from a single pre-blended solution. Furthermore, the as-cast morphology shows macrophase separation of homopolymer (**Figure A.1**) whereas the annealed films regain lamellar morphology. These results suggest that the multilayers were thoroughly mixed during annealing and that the constitutive components were redistributed uniformly throughout the thickness of the film.

Although the nanostructure dimensions can also be increased by blending with block copolymers of similar composition but of higher degrees of polymerization, homopolymers are more readily available and provide the opportunity (as demonstrated below) to easily incorporate functional side groups that can be used to form hierarchically patterned nanostructured surfaces. However, block copolymer and homopolymer blends are usually incapable of decreasing the domain spacing.[56] Block copolymer–block copolymer blends, on the other hand, provide

opportunities to modulate the domain spacing by blending the base layer with copolymer of either higher or lower molecular weight. **Figure 4.2b** shows the reduction of lamellar spacing from D_0 = 52 nm for the base layer (M_n = 114 kg/mol) to D_B = 37 nm for the blend by the addition of a symmetric PS-b-PMMA with a total molecular weight of 51 kg/mol. Significantly above the order-disorder transition ($\chi N \gg 10.5$ for symmetric diblock copolymers),[40] the equilibrium domain spacing of block copolymers scales approximately as the molecular weight to the 2/3 power.[46] Similarly, the period of miscible binary blends of lamellar-forming block copolymers with differing molecular weights scales simply as the effective number-average molecular weight of the system to the 2/3 power:[54]

$$D_B \sim (\sum_i x_i M_{n,i})^{2/3}$$

where x_i and $M_{n,i}$ are the mole fraction and molecular weight of species i, respectively. Bilayer mixing of the symmetric block copolymer systems was observed here to form lamellae with domain spacings that scale with the average molecular weight to the 0.70 power, in good agreement with the theoretical prediction and experimental observations in the bulk.

In addition to tuning domain spacing, multilayer mixing of asymmetric blends of a block copolymer and single homopolymer can be used to modify the equilibrium domain geometry. As characterized previously in the bulk,[58] increasing the volume fraction of homopolymer and the asymmetry of the blend can elicit an order-order transition (OOT) between microphase separated domains such as from lamellar to cylindrical structures (**Figure 4.2c**). In blends with overall PMMA volume fractions ranging from ϕ_{PMMA} = 0.64 to 0.73, a biphasic region with both cylindrical and lamellar structures was observed (**Figure 4.2c**, middle SEM image). Only the hexagonally packed cylindrical phase was self-assembled when multilayers with more PMMA homopolymer were mixed to achieve a ϕ_{PMMA} greater than 0.73 (**Figure 4.2c**, rightmost SEM

image). These observations were confirmed by 2D-FFT analysis of the scanning electron micrographs, where the peaks at $q^*, \sqrt{3}q^*, 2q^*,$ and $\sqrt{7}q^*$ that appear for systems with higher ϕ_{PMMA} are indicative of hexagonal symmetry.

Multilayer mixing with both homopolymer and block copolymer additives in thin films reproduce the morphologies observed experimentally and predicted theoretically for such materials in the bulk, including a gyroid phase (**Figure A.2**), confirming that blends formed via the novel multilayer mixing approach are well-mixed and self-assemble into equilibrium nanostructures that persist throughout the film. This conclusion is surprising, especially given that the morphologies self-assembled by block copolymers in thin films are often found to be process[178] and pathway[179] dependent, but critical to the success of the multilayer process. Molecular diffusion and mixing of components in uncrosslinked regions must thus occur uniformly normal to the substrate, typically through films ~100 nm or thinner. Moreover, in implementations where the block copolymer composition and structure is varied across the film using photolithography to locally fixate the nanostructures, the added components are found to not be mixed and do not cause changes in composition in the crosslinked regions (as indicated by a consistent morphology). Instead, lateral diffusion of the overlying layers away from the crosslinked regions, and into adjacent uncrosslinked regions, occurs in a dewetting process requiring in-plane transport over distances of hundreds of nm to hundreds of μm. Although undoubtedly there is a thin wetting layer (a few nanometers) of the added homopolymers or block copolymers on the surface of the crosslinked regions, as templated by the chemical nanopatterns presented by the crosslinked regions,[177] a significant amount of material must be moved large distances during the rapid annealing process.

Solvent annealing,[179] performed by swelling the polymer films by 100~200% in an environment of saturated solvent vapor, provides even the blends with the highest molecular weight polymers sufficient mobility to undergo both mixing and lateral transport. **Figure 4.3** characterizes the rate of lateral diffusion in a bilayer blending process during solvent annealing. Optical lithography was used to define periodic 10 μm wide crosslinked lines (90 μm spaces between lines) in a self-assembled PS-b-ePMMA base layer of 45 nm in thickness. A second layer 23 nm thick was deposited and contained equal volume fractions of PS (20.8 kg/mol) and a fluorescently-labeled random copolymer of PMMA (12.0 kg/mol). Samples were annealed for varying times from 0 to 120 min, and the surface was characterized by profilometry (**Figure 4.3a**) and fluorescence microscopy (**Figures 4.3b and 4.3c**). Initially, the crosslinked domains were approximately 20 nm thicker than the surrounding film, due to the partial solvation and removal of some uncrosslinked material (typically 30-33%) from the base layer during spin coating of the second layer. The difference in thickness decreased from 20 to 5 nm and peaks broadened from 20 to 30 μm full width at half maximum as a function of annealing time, indicating bulk transport of second layer away from the crosslinked regions. Fluorescence micrographs of the patterned film and corresponding mean fluorescence intensity profiles across the crosslinked lines reveal the spatial distribution of fluorescently-labeled homopolymer during annealing (**Figures 4.3b,c**). Fluorescence microscopy data shows a 10 μm dark band that does not widen but has decreasing fluorescent intensity with annealing, indicating that the homopolymer diffuses away from the crosslinked regions during annealing and is redistributed throughout the remainder of the film.

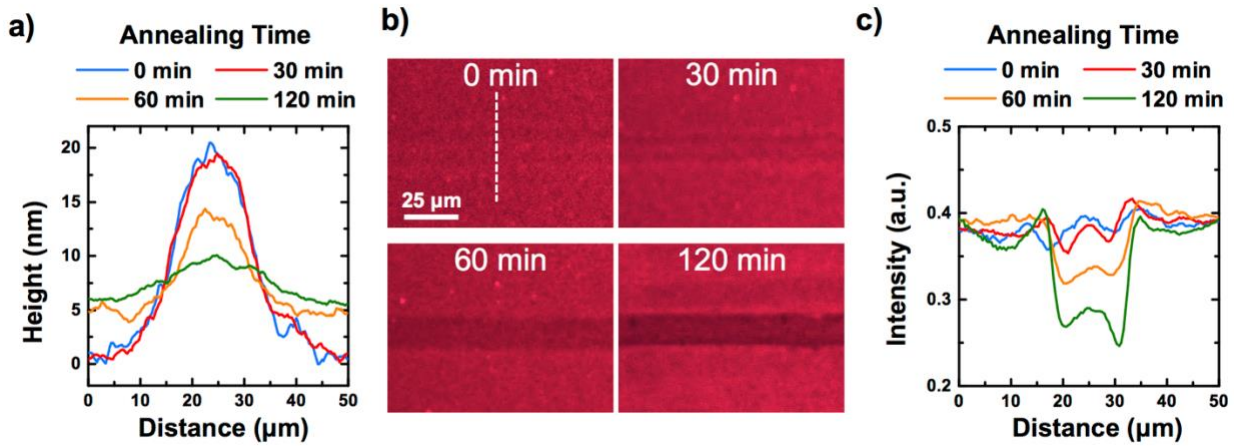

Figure 4.3 Lateral diffusion and blending of polymeric components during the multilayer mixing process. A bilayer system consisting of a first layer of PS-b-ePMMA with a 10 μm wide crosslinked stripe and a second layer containing both PS and fluorescently-labeled PMMA was characterized at varying annealing times by **a** profilometry and **b, c** fluorescence microscopy. A time of 0 min refers to the as-deposited bilayer system prior to solvent annealing. (**a)** One-dimensional traces (as illustrated with the dotted white line in **b**) of the surface topography across a 10 μm wide crosslinked stripe. (**b)** Representative fluorescent microscopy images at varying annealing times and (**c)** the corresponding fluorescence intensity profiles across the 10 μm wide crosslinked stripe averaged in the direction parallel to the stripe.

Substrate wettability is also a critical consideration in the multilayer blending process, especially when the self-assembly of morphologies from across the phase diagram are targeted in the continuous film. Lamellar and cylindrical nanostructures, with orientations perpendicular to the substrate, are particularly desirable given their suitably for pattern transfer processes but are challenging in the same film due to the differences in surface energies that lead to neutrality in domain wetting.[180] **Figure 4.4** demonstrates localized blending to yield three distinct self-assembled morphologies, as produced by mixing and photopatterning of trilayer films. The first layer that was deposited consisted of a blend of block copolymers that formed PS-rich cylindrical domains followed by a second layer of lamellar block copolymer, and a third layer of PMMA homopolymer. The PS-rich cylinders to the PMMA-rich cylinders that were self-assembled span a wide range of block copolymer compositions (ϕ_{PMMA} = 0.30 to 0.73, respectively), and each morphology had perpendicular orientations controlled by the same neutral substrate wetting layer.

The neutral wetting layer used throughout consisted of a crosslinked mat of a random copolymer of PS and PMMA with 58 mol% PS that had previously been optimized for lamellar-forming PS-b-PMMA systems of symmetric composition, and that thus also provided the best balance in surface energy for asymmetric systems that were PS-rich and PMMA-rich. It might be anticipated, however, that blending to compositions with even more extreme asymmetry or the selection of brushes of different surface energy would lead to the self-assembly of films with nanostructures of mixed orientation. Such systems with controlled orientation in addition to controlled morphology may also be valuable, for example by presenting surface accessible nanostructures over only certain portions of the film.[181]

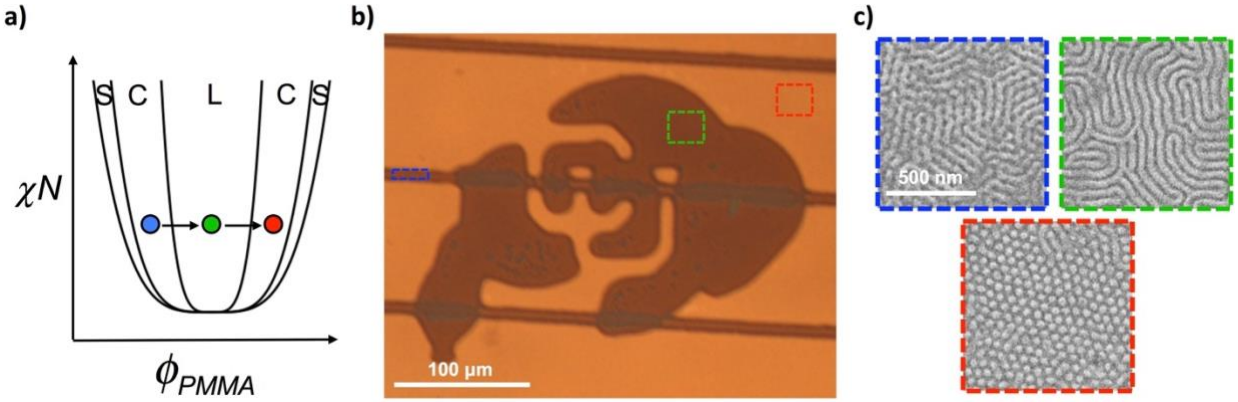

Figure 4.4 Mixing and photopatterning of block copolymer multilayers to achieve localized control over self-assembled morphologies. **(a)** The schematic phase diagram on the left illustrates the compositional and morphological transitions accomplished by a multilayer blending process, and which was characterized by (**b)** optical microscopy and (**c)** scanning electron microscopy. The initial system highlighted in blue through the sequential blended systems highlighted in green and red span morphologies including PS-rich cylinders, lamellae, and PMMA-rich cylinders, respectively. The sequential layers that were deposited consisted of a blend of PS-rich cylindrical and lamellar block copolymers (Layer 1), lamellar block copolymer (Layer 2), and PMMA homopolymer (Layer 3). The optical microscopy image shows crosslinked stripe regions corresponding to Layer 1, the crosslinked buffalo logo corresponding to a blend of Layers 1 and 2, and the uncrosslinked background region consisting of a blend of Layers 1, 2, and 3. Regions containing PS-rich cylinders, lamella, and PMMA-rich cylinders are outlined in blue, green, and red dotted lines respectively. On right, SEM images show the characteristic nanostructures achieved in the outlined regions of corresponding color in the optical microscopy image. The light and dark colors in the SEM images correspond to the PS and PMMA domains, respectively.

Likewise, there are limits to the blend composition that must be briefly discussed. To start, the polymer components must be fully miscible as dictated by χN to allow for mixing. Therefore,

even when blending polymer components of the same composition, polymers of vastly different molecular weight should be avoided (*e.g.*, >5 fold different for pairs of block copolymers[49]) as incomplete mixing and inhomogeneous nanostructures of varying size would result. In addition, block copolymer-homopolymer blends form microemulsions at high homopolymer volume fractions (typically $\phi_h \gtrsim 0.5$)[57] (**Figure A.3**) and macrophase separate when enriched even further with homopolymer. Compositions with extreme homopolymer concentrations may fortunately be avoided during blending by dosing in additional block copolymer, as in **Figure 4.2b**, at any layer in the film.

4.4 Conclusion

In conclusion, multilayer mixing provides a facile approach for accessing the diverse morphologies and dimensions self-assembled by block copolymers in thin films and, when combined with photolithographic methods, allows for well-defined control of the material composition and nanostructures in spatially adjacent regions. Advantageously, the approach is compatible with existing photolithography and polymer film processing techniques, as well as with methods for directed self-assembly to achieve defect-free, long-range order using chemically nanopatterned surfaces[9] or topographically structured substrates.[10] Soft lithography such as microcontact printing,[11] electrohydrodynamic jet printing,[12] and other methods for depositing polymer components to the surface of films[182] also provide promising avenues for locally and rapidly tuning the materials and self-assembly. Another opportunity presented by the multilayer blending method is in selectively and hierarchically functionalizing the films, beyond that already demonstrated by the fluorescent dye-labeled polymers. Copolymer components functionalized with azides or alkynes for click-chemistry reactions or with the biologically relevant binding target biotin may be patterned across the film surface, which may be applied in ultrahigh-density

biosensors or tissue engineering where the ability to pattern a diverse set of functional groups across scales in a low cost and scalable manner is of critical importance.[14]

4.5 Experimental Methods

Preparation of neutral wetting substrates

Silicon wafers (Montco Silicon) were rinsed sequentially in deionized water, acetone (Fisher, 99.8%), and toluene (Sigma-Aldrich, >99.5%). A crosslinkable random copolymer (58 mol% styrene, 41 mol% methyl methacrylate, and 1 mol% glycidyl methacrylate) was synthesized in toluene by free radical polymerization using azobisisobutyronitrile (AIBN) as the initiator. A 0.1 wt% solution in toluene of this random copolymer was spin cast onto cleaned silicon wafers at 5000 rpm for 30 s and thermally treated at 190 °C for 60 min under 10 Torr vacuum. Samples were then sonicated in toluene for 5 min to remove excess polymer and resulted in a crosslinked mat 20 ± 0.25 Å thick.

Multilayer mixing of block copolymer thin films

Block copolymer films were annealed in a mixed solvent vapor of acetone and cyclohexane (Fisher, 99%) for 4 hr. Samples were subsequently baked at 90 °C for 30 min under 10 Torr vacuum to remove any remaining solvent and to densify the films. Homopolymer solutions in toluene of poly(methyl methacrylate) (21.2 kg mol^{-1}, PDI = 1.07, Polymer Source) and/or polystyrene (20.8 kg mol^{-1}, PDI = 1.07, Polymer Source) were then spin-cast at varying film thicknesses, followed by a second solvent annealing for 4 hrs. Poly(styrene-*b*-(methyl methacrylate)) (51 kg mol^{-1}, PDI = 1.06, φ_{PMMA} = 0.48, Polymer Source) solutions and trilayer films were deposited and processed in a similar fashion.

Photopatterning

Epoxy-functionalized crosslinkable block copolymers (PS-b-ePMMA) (114 kg mol^{-1}, PDI = 1.38, φ_{PMMA} = 0.56; 66 kg mol^{-1}, PDI = 1.30, φ_{PMMA} = 0.26) were synthesized by sequential atom transfer radical polymerization (ATRP) as reported elsewhere.[8] Briefly, block copolymers were synthesized by sequential atom transfer radical polymerization (ATRP). Polystyrene macroinitiator was synthesized and purified before being used as the initiator to grow the poly(methyl methacrylate) block. Solutions of 1.0 wt% PS-b-ePMMA containing 0.05 wt% photoinitiator (Irgacure 290) were prepared in ethyl acetate. These solutions were used to spin cast thin films (~45 nm) of PS-b-ePMMA followed by solvent annealing. Solvent annealed block copolymer was baked at 90 °C for 30 min under 10 Torr vacuum, exposed to 365 nm UV for 1-2 min, and post baked at 130 °C for 2 min to crosslink the ePMMA domain of exposed regions of the block copolymer.

Characterization of thin film morphologies

Surface morphologies of the block copolymer films were imaged with a field-emission SEM (JEOL JSM-7401F) at 1 kV in gentle beam mode. Film thicknesses were determined by spectroscopic ellipsometry (J.A. Woollam VASE-VB 250) using a variable angle of 60°-80° and wavelengths from 500-800 nm. Surface topology was measured by using a Dektak 6M stylus profilometer with a 12.5 μm stylus tip. Periodicity of self-assembled nanostructures was determined by 2D-FFT image analysis of SEM images.

Fluorescence Microscopy

Poly((methyl methacrylate)-r-(2-isocyanatoethyl acrylate)) (PMMA-ICEA) was synthesized by free radical polymerization using AIBN as an initiator. Briefly, monomers methyl methacrylate (Acros, stabilized, 99%) and 2-isocyantoethyl acrylate (Sigma-Aldrich, stabilized, 98%) were purified on silica absorption columns. Monomers and initiator were dissolved in anhydrous toluene and heated to 80 °C for 48 hrs followed by purification by precipitating in hexanes. The resulting copolymer (M_n = 12 kg/mol, PDI = 1.43) contained 6 mol% 2-isocyantoethyl acrylate by ^{1}H NMR. PMMA-ICEA was then dissolved in anhydrous dimethyl sulfoxide (Biotium) and allowed to react with excess Alexa Fluor® 555 Cadaverine at 50 °C for 120 hrs followed by purification by precipitation in DI water. Dye-conjugated PMMA-ICEA was then dissolved in toluene and deposited and processed similar to other homopolymer solutions above. Samples were imaged by laser scanning confocal microscopy (Zeiss LSM5 Pascal) to visualize the spatial distribution of dye-functionalized PMMA-ICEA at varying annealing times.

4.7 Acknowledgements

This material is based upon work supported by the National Science Foundation Graduate Research Fellowship under Grant No. DGE 1144083 (G.R.C.). This work was performed in part at the University of Colorado's Nanomaterials Characterization Facility.

Chapter 5: Role of Dimension and Spatial Arrangement on the Activity of Coupled Biocatalytic Reactions on Scaffolds

Adapted from ACS Catalysis, 6, 5161-5169

5.1 Abstract

Despite broad interest in engineering enzyme cascades on surfaces (*i.e.*, for multi-step biocatalysis, enzyme-mediated electrocatalysis, biosensing, and synthetic biology), there is a fundamental gap in understanding about how the local density and spatial arrangement of enzymes impacts overall activity. In this work, the dependence of the overall activity of a cascade reaction on geometric arrangement and density of enzymes immobilized on a two-dimensional scaffold was elucidated using kinetic Monte Carlo simulations. Simulations were specifically used to track the molecular trajectories of the reaction species and to investigate the turnover frequency of individual enzymes on the surface under diffusion-limited and reaction-limited conditions for random, linear striped, and hexagonal arrangements of the enzymes. Interestingly, the simulation results showed that, under diffusion-limited conditions, the overall cascade activity was only weakly dependent on spatial arrangement and, specifically, nearest-neighbor distance for high enzyme surface coverages. This dependence becomes negligible for reaction-limited conditions, implying that spatial arrangement has only a minimal impact on cascade activity for the length-scales studied here, which has important practical implications. These results suggest that, at short length scales (*i.e.*, sub-10 nm dimensions) and high enzyme densities, sophisticated approaches for controlling enzyme spatial arrangement have little benefit over random immobilization. Moreover, our findings suggest that engineering artificial cascades with enhanced activity will likely require direct molecular channeling rather than relying on free molecular diffusion.

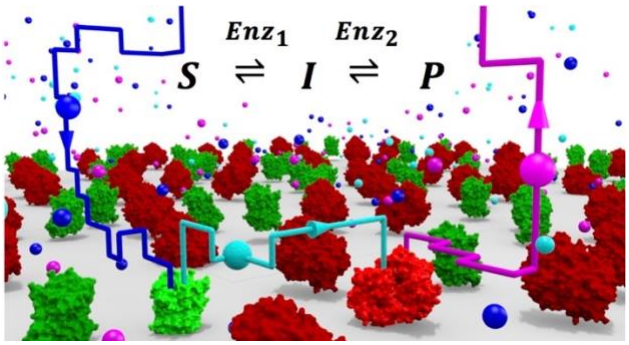

Figure 5.1 Graphical abstract: Scheme of the lattice kinetic Monte Carlo simulation used to study the effects of dimension and spatial arrangement of enzymes on the activity of coupled biocatalytic reactions.

5.2 Introduction

In nature, the efficiency of coupled enzymatic reactions and, more broadly, metabolic pathways, is enhanced via control over the spatial organization of enzymes on natural scaffolds. Specifically, within cells, enzymes involved in cascade reactions are frequently co-anchored to membrane surfaces,[183–185] microtubules,[186,187] filaments,[187] or scaffold proteins,[96] resulting in co-localization or, in some cases, compartmentalization of the enzymes at defined stoichiometry. Co-localization, in turn, enables the local concentration of substrates and intermediates to be modulated and facilitates the channeling of intermediates between sequential enzymes by various mechanisms including electrostatic interactions and molecular tunnels.[76] A notable example of such organization in nature is the co-anchoring of enzymes involved in the electron transport chain in the inner mitochondrial membrane in eukaryotic cells.[183] Similar examples include the co-localization of photosynthetic enzymes in the membrane of chloroplasts in plant cells[184] and complexes of cellulolytic enzymes found on the cell surface of bacteria or free in solution that degrade insoluble cellulose into soluble products.[188] The hierarchical assembly of these enzymes into cellulosome complexes, which have diverse architectures across bacterial species, is mediated by an integrating subunit known as scaffoldin.[185] Additionally, the co-binding of mitogen-activated protein kinases to non-catalytic scaffolding proteins such as Ste5 in *Saccharomyces cerevisiae* is a hallmark of MAPK signaling pathways, which leads to enhanced signal transduction.[96]

Inspired by examples from nature, the development of methods to engineer enzyme cascades on surfaces for various applications in biotechnology, including multi-step biocatalysis,[20,21,189,190] enzyme-mediated electrocatalysis (*i.e.*, in biofuel cells),[22,23,191] biosensing,[24,192] and synthetic biology,[98,193–195] have received considerable attention. Of particular interest has been the immobilization of enzyme cascades on surfaces using natural scaffolds or, alternatively, synthetic approaches that enable the inter-enzyme distance to be tightly controlled.[19,196] For example, native and synthetic metabolons have been immobilized on electrode surfaces to improve the current density of biofuel cells compared to first generation biofuel cells that contained a single immobilized oxidoreductase enzyme.[23,191] Moreover, Eguilaz and co-workers[24] co-immobilized cholesterol oxidase and horseradish peroxidase on a carbon nanotube-modified glassy carbon electrode to enable the detection of cholesterol. In this approach, cholesterol was initially oxidized by cholesterol oxidase to generate hydrogen peroxide, which was subsequently used to oxidize hydroquinone by horseradish peroxidase. The electrochemical reduction of the formed benzoquinone at the electrode surface generated a flow of electrons that could be detected as an electrical signal.

A number of approaches have been reported for the preparation and functionalization of synthetic scaffolds to control the distance between co-immobilized enzymes. Specifically, DNA origami has been used to co-immobilize enzyme cascades such as horseradish peroxidase/glucose oxidase[27,99] and xylose reductase/xylitol dehydrogenase[197] to surfaces while systematically controlling the inter-enzyme distance, which was shown to have a significant impact on the overall rate of the coupled enzymatic reaction. More recently, alternative approaches for co-immobilizing proteins with defined spatial organization have been investigated, including photolithography,[198] microcontact printing,[199] and electron beam lithography.[200,201] Although it has not yet been

demonstrated with multiple proteins, one can also envision multi-functionalized self-assembling materials such as block copolymers[13,202] as being useful for patterning proteins and enzyme cascades on surfaces. It is important to note that the aforementioned techniques enable the preparation of scaffolds for enzyme immobilization with a diverse range of enzyme densities (*i.e.*, two isolated enzymes for tiles of DNA origami to highly packed surfaces of enzymes prepared by photolithography) and with widely disparate distances between co-immobilized enzymes (*i.e.*, 1~10 nm scale for DNA origami, 10~100 nm scale for electron beam lithography, and 1~100 micrometer scale for microcontact printing and photolithography).

In spite of the evidence that the inter-enzyme distance of immobilized enzymes impacts the overall reaction rates for sparse enzyme pairs, the influence of spatial organization of enzymes in densely packed arrangements is an open question. Specifically, there is a fundamental gap in understanding how the local density and spatial arrangement of coupled enzymes affects the diffusion of intermediates between the enzymes and thus the ultimate rate of product formation. Idan and Hess developed a numerical model that couples Fickian diffusion with Michaelis-Menten kinetics to understand the impact of inter-enzyme distance on pairs of isolated enzymes.[101] While this model was extended to explore the impact of inter-enzyme distance for arrays of enzyme pairs, this effect was only considered for a single three-dimensional arrangement. Similar reaction-diffusion models have been developed to determine optimal enzyme arrangements in dense systems such as the cytoplasm of a cell,[104–106] and the rate of product formation was found to be highly dependent on enzyme co-localization. These reaction-diffusion models, however, treat the enzymes as a continuum with a homogeneous density defined by the enzyme concentration in the bulk, and therefore are unable to capture the behavior of inhomogeneous enzyme distributions that arise in enzymatic cascades immobilized in well-defined spatial arrangements.

In this work, we explore the dependence of the overall activity of a cascade reaction on the geometric arrangement and density of the enzymes immobilized on a two-dimensional scaffold. Using a kinetic Monte Carlo simulation, we reveal spatial organizations of the enzymes that lead to enhanced rates by quantitatively comparing the concentration profiles of reaction species and the turnover frequency of individual enzymes, both under diffusion-limited and reaction-limited conditions. Random, linear striped, and hexagonal arrangements of the sequential enzymes were considered, in part, due to the availability of fabrication techniques for heterogeneously functionalizing supports with such patterns. Ultimately, the results presented here inform the design of the spatial arrangement of enzymes in coupled biocatalytic reactions and suggest that the greatest rate enhancements require placement of the enzymes with nanometer-level precision.

5.3 Computational Methods

Lattice Monte Carlo simulations were performed to describe the reaction kinetics and molecular diffusion of a multi-enzyme cascade reaction. Molecular diffusion was modeled by independent random walks of individual molecules of substrate (S), intermediate (I), and product (P) along the lattice. The solvent medium was taken to be non-interacting and non-participatory in the enzyme reactions, and therefore was not treated explicitly. Reactions were modeled according to equations 5.1 and 5.2 below:

$$Enz_1 + S \underset{k_{-1}}{\overset{k_1}{\rightleftharpoons}} Enz_1S \overset{k_{cat,1}}{\rightarrow} Enz_1 + I \qquad \textbf{(5.1)}$$

$$Enz_2 + I \underset{k_{-2}}{\overset{k_2}{\rightleftharpoons}} Enz_2I \overset{k_{cat,2}}{\rightarrow} Enz_2 + P \qquad \textbf{(5.2)}$$

where Enz_1 and Enz_2 represent the sequential enzymes and k_i indicates the rate constant for each elementary step i. These rate constants were used to define reaction probabilities, rp_i, for the

elementary steps. When modeling a diffusion-limited system, all forward probabilities (rp_i for > 0) were set to 1 to achieve the fastest turnover rates (*i.e.*, $k_{cat,1} = k_{cat,2} \approx 7.30 \times 10^8$ s^{-1}). To model reaction-limited systems, complex formation was assumed to be instantaneous while the unimolecular reaction probabilities were approximated by $rp_i = k_i \Delta t$.[203] Here Δt was approximately 1.37 ns per simulation step, as calculated by measuring the mean square displacement of freely diffusing molecules along a lattice with a step size of 1 nm and assuming a small molecule diffusion constant of 10^{-10} m^2/s. In both diffusion-limited and reaction-limited conditions, reverse probabilities (rp_i for $i < 0$) were specified to be 0, which is justified given that, in general,[204] $k_1 >> k_{-1}$ and $k_2 >> k_{-2}$ and the concentrations of I and P are much lower than S at low conversions.

The kinetic Monte Carlo simulations were implemented in MATLAB® (MATLAB R2015b (8.6.0), The MathWorks, Inc., Natick, Massachusetts, USA) and run on personal computers. Sequential enzymes Enz_1 and Enz_2 were represented as two-dimensional circles with diameters of 5 nm and were placed simultaneously on the surface of the scaffold ($z = 0$) according to the desired geometric arrangement. At the start of each simulation, substrate molecules were distributed randomly throughout the three-dimensional lattice at a concentration of 0.1 mM. Free molecules in the simulation box were moved randomly to one of the neighboring lattice sites, with an average move of 1 lattice site per molecule per simulation step. Periodic boundary conditions were applied for the simulation box in the *x* and *y* directions. Molecules that diffused across the upper *z* boundary were specified to enter the bulk of the solution and replaced by a molecule of a type (*i.e.*, S, I, or P) randomly selected based on the relative concentrations in the bulk, such that the number of molecules in the simulation box remained constant. Free molecules that reached the $z = 0$ surface of the simulation box were checked to determine whether they encountered an available enzyme

and, if so, complexation to the enzyme was evaluated based on the reaction probabilities specified in Equations 5.1 and 5.2. Each enzyme was limited to being engaged with only one molecule at a time. Molecules bound to enzymes were also evaluated at each time step to determine whether they became unbound from the enzyme or were converted to product based on the reaction probabilities.

Simulation details for the different enzyme arrangements are as follows:

Dense Random Arrangement of Enzymes - Enzymes were positioned on the scaffold by randomly selecting their coordinates while prohibiting enzymes from overlapping. Total enzyme densities ranging from 1.9×10^{-4} to 240×10^{-4} enzymes/nm^2 were simulated with a stoichiometric ratio of each enzyme (*i.e.*, [Enz_1]:[Enz_2] = 1:1). A cubic lattice with a lattice spacing of 1 nm was used in all cases, and the simulation box was 200 x 200 x 5,000 nm^3 or 400 x 400 x 5,000 nm^3 depending on the enzyme density.

Dense Patterned Arrangements of Enzymes - Enzymes were positioned on the scaffold by randomly selecting their coordinates from within defined regions of the patterned scaffold and while prohibiting enzymes from overlapping. The enzyme density was fixed at 240×10^{-4} enzymes/nm^2. Cubic and hexagonal lattices were used for patterned arrangements with linear and hexagonal symmetry, respectively, each with lattice segment lengths of 1 nm. The simulation box had a volume of 200 x 200 x 5,000 nm^3 for linear arrangements with pattern periods of 10 to 200 nm. The simulation box was increased to 800 x 100 x 5,000 nm^3 and 1,600 x 100 x 5,000 nm^3 for linear periods of 800 and 1600 nm, respectively. For hexagonal arrangements, the simulation box was a rhombohedron with dimensions of 200 x 200 x 5,000 nm^3 for hexagonal center-to-center distances (*i.e.*, periods) of 10 to 100 nm and 400 x 400 x 5,000 nm^3 for hexagonal center-to-center distances of 200 nm.

Isolated Pairs of Enzymes – One enzyme of each type was positioned a fixed distance apart, set to vary from 5 to 50 nm, at the center of a simulation box with dimensions of 100 x 100 x 5000 nm^3 for all simulations. A cubic lattice with a lattice spacing of 1 nm was used. Periodic boundary conditions were applied for the substrate S molecules, but in order to capture the reaction kinetics and molecular diffusion of a truly isolated pair of enzymes, the trajectories of all intermediate I and product P molecules were tracked outside of the box and allowed to react only if they were within the simulation volume (*i.e.*, periodic boundary conditions were turned off for the I and P components).

The simulations were run to 10^8 steps and 4-5 distinct simulations (*i.e.*, distinct enzyme distributions, initial molecule configurations, and stochastic sampling) were performed for each condition to ensure that the results were statistically significant. Throughout the simulations, the total concentration of each component was recorded. Cascade activity was calculated as the slope of a linear fit of the concentration from the final 2.5×10^7 steps of each simulation, and the activities were averaged over individual replicates. Error bars are reported as one standard deviation from the average of these replicates. The frequency and type of each elementary reaction step was recorded for each enzyme.

5.4 Results and Discussion

The impact of the spatial arrangement of surface-immobilized sequential enzymes on the overall activity of a theoretical enzyme cascade was investigated using kinetic Monte Carlo simulations. Specifically, using the kinetic Monte Carlo simulations, this impact was analyzed for a two enzyme cascade in both the diffusion-limited (where the overall reaction rate was limited by molecular transport of the substrate and intermediate molecules) and reaction-limited (where the overall reaction rate was limited by the enzymatic turnover of the substrate or intermediate)

regimes. In nature, there are many examples of enzymes that are diffusion-limited (*e.g.*, superoxide dismutase and catalase,[205] which may be used in a cascade configuration to reduce reactive oxygen species to water) as well as those that are reaction-limited (*e.g.*, horseradish peroxidase and glucose oxidase, a commonly used enzyme cascade that reduces oxygen to water),[206] making it relevant to study both cases. The basis for the simulations is illustrated in **Figure 5.2**. In the simulation, the free molecular diffusion of the substrate (S), intermediate (I), and product (P) was modeled as a random walk in a three-dimensional lattice space. Upon the successful interaction of S with the first enzyme (Enz_1), the resulting I is converted to P via the successful diffusion of I to the second enzyme (Enz_2). To understand the impact of the density of the enzymes on the surface, the surface coverage of Enz_1 and Enz_2 was varied, which, in turn, alters the average nearest-neighbor distance between the enzymes. Additionally, for the diffusion-limited case, the reactions at Enz_1 and Enz_2 were assumed to be instantaneous, whereas, for the reaction-limited case, Enz_2 was assigned a lower k_{cat} value resulting in the accumulation of I over time. In all simulations, the position of every S, I, and P molecule was tracked explicitly throughout the course of the simulations (1×10^8 simulation steps or ~137 ms), which allowed the traversed length of the molecular trajectories and the activity of every individual enzyme on the surface to be determined. Moreover, it was assumed that all of the enzyme molecules were active and stable over the entire simulation (*i.e.*, enzyme activity was constant at steady state), and, furthermore, that the impact of the immobilization and surface orientation on enzyme activity was negligible.

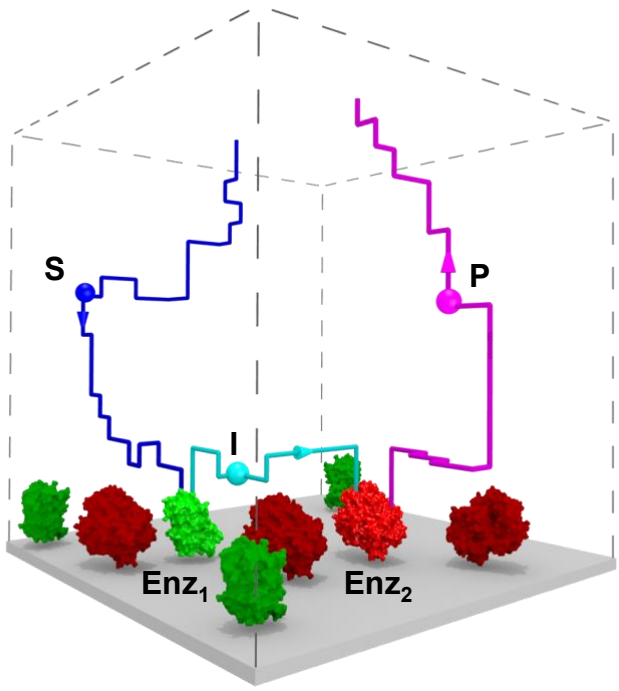

Figure 5.2 Scheme of the lattice kinetic Monte Carlo simulations used to investigate the impact of spatial arrangement on the overall reaction rate of the theoretical enzyme cascade. The scheme illustrates a representative cascade reaction involving the free molecular diffusion of substrate S (blue trajectory), intermediate I (cyan trajectory), and product P (purple trajectory), as well as the enzymatic turnover of S and I by the first enzyme (Enz_1 shown in green) and the second enzyme (Enz_2 shown in red) respectively. The dashed lines indicate the boundaries of the three-dimensional simulation box (not shown to scale) used to model the reaction-diffusion system.

5.4.1 Impact of Enzyme Surface Density on the Activity of an Enzyme Cascade Reaction

As an initial step in understanding the impact of the spatial arrangement on the overall activity of a theoretical enzyme cascade, the extent to which the density of enzyme randomly immobilized on the surface alters the rate of product formation was analyzed. Of note, at each surface density, half of the enzyme molecules on the surface were of type Enz_1 and the other half were of type Enz_2. Intuitively, in the diffusion-limited case investigated here first, one would expect that varying the surface coverage of enzymes would have a significant impact on the overall conversion of S to P at steady-state. This intuition is based on the presumption that decreasing the average nearest-neighbor distance between Enz_1 and Enz_2 would reduce the path length required

for I to diffuse prior to being converted to P. However, surprisingly, simulations with varying surface densities of Enz_1 and Enz_2 showed that this was not the case. Specifically, when varying the density of randomly immobilized Enz_1 and Enz_2 from 240 x 10^{-4} to 15 x 10^{-4} enzymes/nm^2 (**Figure 5.3a**), which corresponded to an increase in average nearest-neighbor distance between Enz_1 and Enz_2 (*i.e.,* inter-enzyme distance) from 6.9 to 25.7 nm, the rate of production of P decreased only slightly. **Figure 5.3b** shows the net turnover to product for the enzyme cascade, over the course of the simulation, as a function of the enzyme surface density. For all enzyme densities, a non-linear response was observed initially until steady-state concentrations and distributions of S, I, and P were reached at longer simulation times (~75 ms). The initial cascade activity exceeded the steady-state activity because at early simulation times the concentration of S close to the surface was higher than at steady-state. Over the course of the reaction, S was consumed and, in turn, depleted near the surface until a steady-state was reached. At steady-state, there was a constant gradient in the concentration of S between the bulk solution, where the concentration of S was high, and the near-surface environment, where the concentration of S was low. A gradient in P is also reached at steady-state, although, as expected, in the opposite direction, resulting in an approximately homogeneous density of total molecules in the simulation box.

The steady-state cascade activity was determined by fitting the slope of the linear region of the product conversion curve and was found to decrease from 1.45 ± 0.04 to 0.96 ± 0.08 product molecules/nm^2/s for the highest to lowest enzyme densities on the surface, respectively. On a relative basis, when normalized as in **Figure 5.3c** to the highest enzymatic activity case, the overall rate of product formation decreased by only 35% for the lowest enzyme surface coverage (*i.e.*, 1.875 x 10^{-4} enzymes/nm^2). Given that the enzyme density varies by greater than two orders of magnitude, such a finding was counterintuitive and, moreover, suggests that, in practice, similar

reaction rates may be achieved using relatively low surface coverages (*i.e.*, loadings) of enzymes compared to high surface coverages, which are typically used or suggested in practical applications. In part, the higher than expected activity at low enzyme surface coverage results from an increase in the steady-state concentration of I (**Figure A.4**), as I must probe greater portions of the surface to find Enz_2. Furthermore, it is interesting to note that, under diffusion-limited conditions, the enzymes at low surface coverages are more efficiently utilized as the turnover per enzyme is higher (**Figure A.5**).

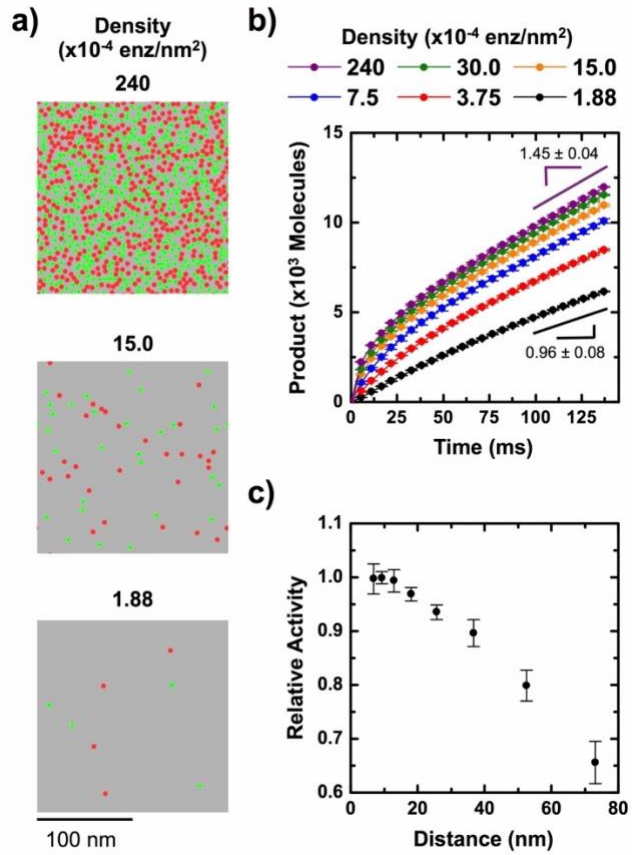

Figure 5.3 Cascade activity as a function of coverage for enzymes randomly immobilized on surfaces under diffusion-limited conditions. (**a**) Images of Enz_1 (green) and Enz_2 (red) immobilized on surfaces (gray) at total enzyme densities from 240 to 1.875 x 10^{-4} enzymes/nm^2. The ratio of Enz_1 to Enz_2 was 1:1 in each case. (**b**) Cumulative number of product molecules converted as a function of simulation time and enzyme surface density. Each curve is the average of four independent simulations. The cascade activity at steady-state was determined as an average of the linear fits of the individual simulations over times from 103 to 137 ms, as illustrated for the highest (purple) and lowest (black) enzyme coverages. The reported error bars indicate one standard deviation from the average. (**c**) Relative activity of the simulated enzyme cascade as a function of the average center-to-center distance between the nearest-neighbor sequential enzymes.

5.4.2 Impact of Enzyme Spatial Arrangement on the Activity of an Enzyme Cascade Reaction

To investigate the impact of the spatial arrangement of enzymes on the activity of the two enzyme cascade under diffusion-limited conditions, Enz_1 and Enz_2 were arranged in linear striped (*i.e.*, lamellar) and hexagonal geometries. These geometries were selected because of the ready availability of lithographic and self-assembly techniques for defining such patterns on surfaces. In the case of the linear striped geometry, Enz_1 and Enz_2 were positioned in alternating stripes with varying periodicity from 10 nm to 1.6 µm. For the hexagonal arrangement, Enz_1 and Enz_2 were positioned in the isolated circular domains and surrounding matrix, respectively. Additionally, as in the lamellar geometry, the hexagonal period was also varied. A visual depiction of the geometries and pattern periods used is shown in the left panels of **Figure 5.4a** and **b**. In all cases, a high enzyme surface density of 240×10^{-4} enzymes/nm^2 was chosen and the number of Enz_1 and Enz_2 molecules were equal, such that the size of both the Enz1 and Enz2 domains varied with the period of the patterned geometry. The minimum dimension of the enzyme patterns, for both geometries, was limited to be 5 nm, which is equal to the diameter of the simulated enzymes.

Comparison of the steady-state rate profiles for the production of P for the diffusion-limited case shows that, for both geometries, the overall activity of the theoretical cascade decreases with increasing period (**Figure 5.4a** and **b**). However, such differences were minimal, which was further illustrated by analyzing the relative difference in activity as a function of periodicity for each geometry (lower right panel for both cases). When the placement of Enz_1 and Enz_2 is inverted for the hexagonal case, the difference in activity is also negligible (**Figure A.6**). The difference in activity relative to the smallest period (10 nm), which was statistically significant, was greatest when the period of the spatial arrangement of enzymes on the surface exceeded ~1 µm. To further illustrate how changes in periodicity impact activity of the cascade, heat maps of the number of

turnover events for the individual enzyme molecules on the surface were generated (**Figure 5.5**). For small periodicities, much as for the random case (**Figure A.5**), the distribution of turnover events for the enzymes across the surface is largely uniform. However, as the periodicity increase, differences in the number of turnover events across the surface become more apparent. This is particularly true for Enz_2 where the highest number of turnover events occur at enzymes that are at the interface between the stripes. The difference in turnover events for enzymes at the interface relative to within the domains is most apparent for the 200, 800, and 1600 nm (**Figure A.7**) cases, although subtle differences in turnover events as a function of location can also be seen in the heat map for the 50 nm case. Such differences are not surprising given that, as I diffuses from the domain containing Enz_1, the initial molecules of Enz_2 that it encounters are at the interface between stripes. For Enz_1, this difference is not surprisingly smaller because the probability of S initially adsorbing in the stripe containing Enz_1 is 50%. As such, the dependence of the activity of Enz_1 on the diffusion of S from the stripe populated by Enz_2 is significantly lower than that of the activity of Enz_2 on the diffusion of I from the stripe populated by Enz_1.

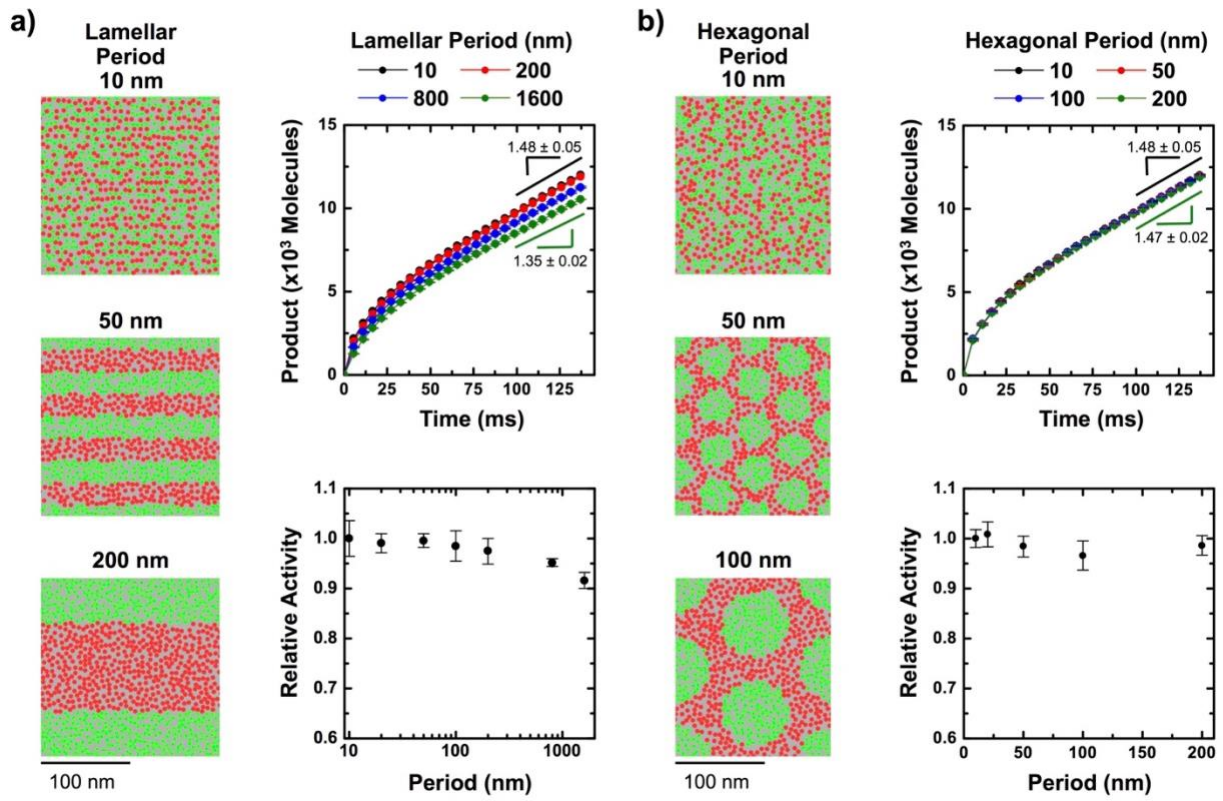

Figure 5.4 Cascade activity as a function of pattern period for enzymes immobilized on surfaces in (**a**) lamellar striped and (**b**) hexagonal spatial arrangements under diffusion-limited conditions. The images at the left of each panel show the positions of Enz_1 (green) and Enz_2 (red) immobilized on patterned surfaces (gray) with the denoted periodicity. A consistent total enzyme density of 240 x 10^{-4} enzymes/nm^2 and 1:1 ratio of Enz_1 to Enz_2 was used each case. The cumulative product formation as a function of simulation time and the relative activity as a function of pattern period are reported in the top and bottom graphs, respectively, of each panel.

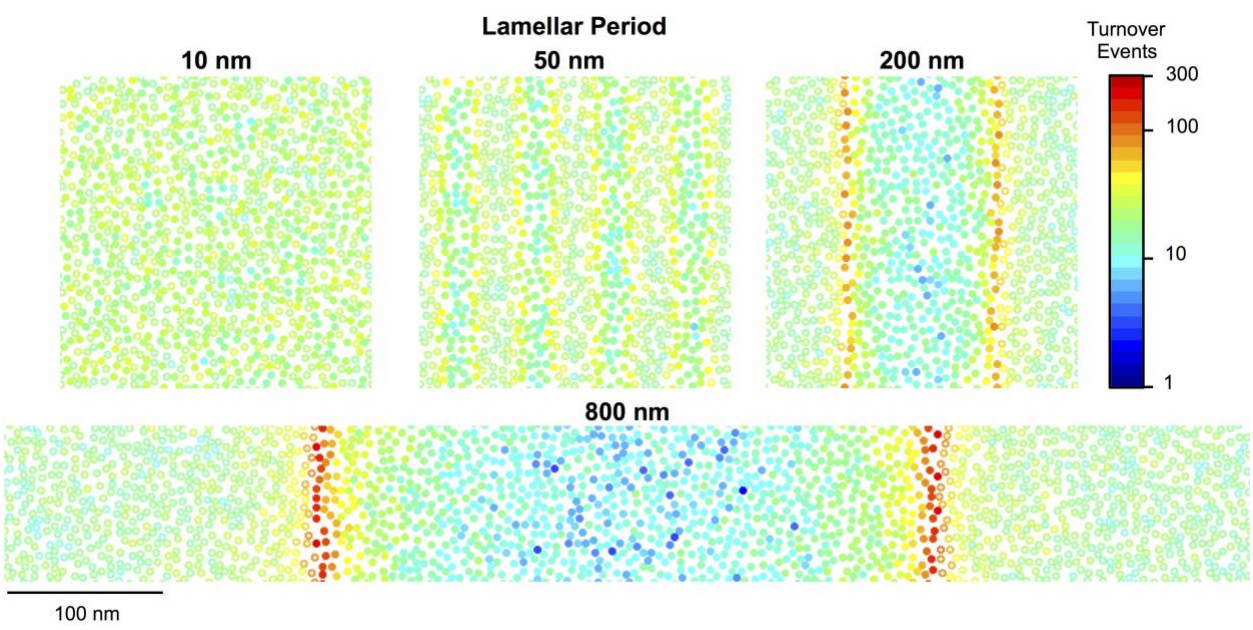

Figure 5.5 Heat map of activity for individual enzymes immobilized in lamellar spatial arrangements with periods from 10 to 800 nm under diffusion-limited conditions for representative simulations. Each enzyme is colored based on the number of reaction turnover events during the entire 137 ms simulation, as denoted by the colorbar, which is presented with a $\log_{10}$-scale. The open and closed circles represent individual molecules of Enz_1 to Enz_2, respectively. A total enzyme density of 240 x 10^{-4} enzymes/nm^2 and 1:1 ratio of Enz_1 to Enz_2 was used each case.

The overall cascade activity for the smallest period arrangements were statistically indistinguishable from the randomly distributed geometries at the same high enzyme density (1.48 ± 0.05 compared to 1.45 ± 0.04 product molecules/nm^2/s, respectively). A slight enhancement in activity for the smallest period arrangements is likely to be observed with additional statistics because the surfaces with control over the spatial arrangement of enzymes prohibit the formation of distinct clusters of Enz_1 and Enz_2, leading to a more homogeneous distribution of enzymes across the surface (see enzyme maps in **Figures 5.3a** and **5.4**). Such differences in the uniformity of enzymes across the surface and the local nearest-neighbor packing lead to small reductions in the average inter-enzyme distance, and thus the enhanced cascade reaction rates, for the spatially structured surfaces. This subtle effect is captured in **Figure 5.6**, which shows the radial distribution function for pairs of Enz_1 and Enz_2 in random and lamellar arrangements for a defined surface

density of enzymes (240 x 10^{-4} enzymes/nm^2) as well as the probability of I colliding with the surface at a given radial distance from Enz_1. The radial distribution function for the pairs indicates the probability of finding a pair of Enz_1 and Enz_2 molecules at a given distance apart relative to the average between any two enzymes (a value greater than 1 indicates a higher than average probability of Enz_1 and Enz_2 being co-localized at this distance). From these probabilities, the probability of I adsorbing to the surface and reacting at the location that it adsorbs at a given radial distance away from Enz_1 is also shown. Notably, the plot of the probability of I colliding with the surface at a given radial distance from Enz_1 follows a 1/r dependence, which has been reported previously.[100,101] As observed, the reaction probability at short inter-enzyme distances is enhanced for the 10 nm lamellar case compared to the random case, but is lower at inter-enzyme distances of ~8-12 nm, which is equivalent to one period. Conversely, the 800 nm lamellar case has a markedly lower reaction probability, especially at short inter-enzyme distances, which is consistent with the lower overall activity for the cascade.

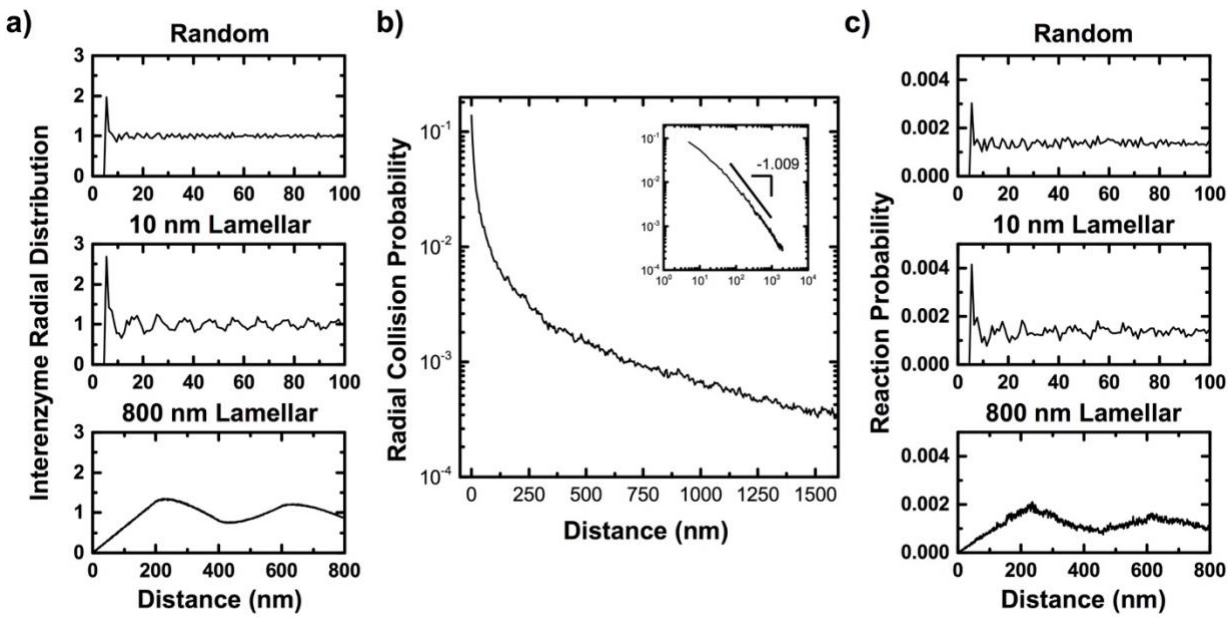

Figure 5.6 Local structure and probability of reaction as a function of distance between Enz_1 and Enz_2 molecules involved in a cascade reaction. (**a**) Radial distribution function for pairs of Enz_1 and Enz_2 molecules in random and lamellar spatial arrangements of enzymes with surface densities of 240 x 10^{-4} enzymes/nm^2. Each curve is the average of 5-10 distinct simulations. (**b**) Probability of an I molecule colliding with the surface at a radial distance from Enz_1 where the I molecule was generated. Inset shows the same data plotted on a log-log scale and the 1/r dependence. (**c**) Probability of an I molecule colliding and reacting with the surface as a function of radial distance from Enz_1 where the I molecule was generated.

In light of these findings, it can be concluded that engineering the arrangement of densely packed enzymes on surfaces has little impact on the overall activity of biocatalytic cascade reactions, and that a comparable turnover rate may be achieved by randomly immobilizing the enzymes on the surface. It is furthermore unlikely that specifically controlling the orientation of enzyme active sites on these densely packed surfaces would enhance cascade activity; the inter-enzyme radial distribution is radially symmetric and so the average distance over which an intermediate molecule must diffuse to encounter the sequential active site is independent of the radial orientation of the enzyme active sites. This has important practical implications on the immobilization of enzymes involved in cascade reactions. Specifically, our findings suggest that controlling the spatial arrangement of enzymes on the surface adds unnecessary complication and

challenges with little to no benefit on overall activity. Rather, it is clear that immobilizing enzymes with spatial arrangements having microscale dimensions, as most easily accessible using optical and soft lithography techniques, is particularly detrimental in terms of the cascade activity and making efficient use of the enzymes.

5.4.3 Impact of Enzyme Spatial Arrangement on Cascade Activity for the Reaction-Limited Case

Some enzymes cascades exhibit an overall activity that is limited by the turnover rate of the enzymes rather than the diffusion of S and I molecules. To understand the impact of enzyme spatial arrangement in such cases, the cascade activity was examined for the case where the activity of Enz_2 was limited. Specifically, a finite turnover rate (100 s^{-1}) was specified for Enz_2, while the turnover rate of Enz_1 was set to be several orders of magnitude higher (7 x 10^8 s^{-1} as in the diffusion-limited cases discussed above). Interestingly, the simulation results show that, under such conditions, there is no advantage (or penalty) to patterning the enzymes on the surface. **Figure 5.7a** shows that the overall activity of the cascade is independent of the spatial arrangement of enzymes on the surface, even for large pattern periods, and is equivalent to 1.17 ± 0.02 product molecules/nm^2/s or an average enzyme turnover of 98 ± 2 s^{-1}. At steady-state, I, which was generated faster than it was consumed, accumulated in the simulation box with the majority of Enz_2 in complex with I and thus unavailable to bind new molecules of I. Given the excess of I, the turnover of Enz_2 was thus constant across the lamellar stripe, even for the 800 nm period case as shown in **Figure 5.7b** (green curve), differing significantly from the diffusion-limited case where the interfacial enzymes were most active (red curve in **Figure 5.7b**).

Similar findings may be made for the reaction-limited case in which Enz_1 has a turnover rate many orders of magnitude slower than Enz_2, as shown in **Figure A.8**. The overall activity of the cascade is dictated by the limiting step and is measured to be 1.20 ± 0.03 and 1.15 ± 0.03

product molecules/nm^2/s for the random and 800 nm lamellar cases, respectively, matching the turnover rate specified for Enz_1. Furthermore, it is important to note that the distinction between the reaction-limited and diffusion-limited cases depends on the initial concentration of S in the simulation. As the concentration of S is increased, a transition from a diffusion-limited regime to one that is reaction-limited would eventually occur. This transition would result in a more uniform distribution of turnover events between molecules at the interfaces and within the stripes.

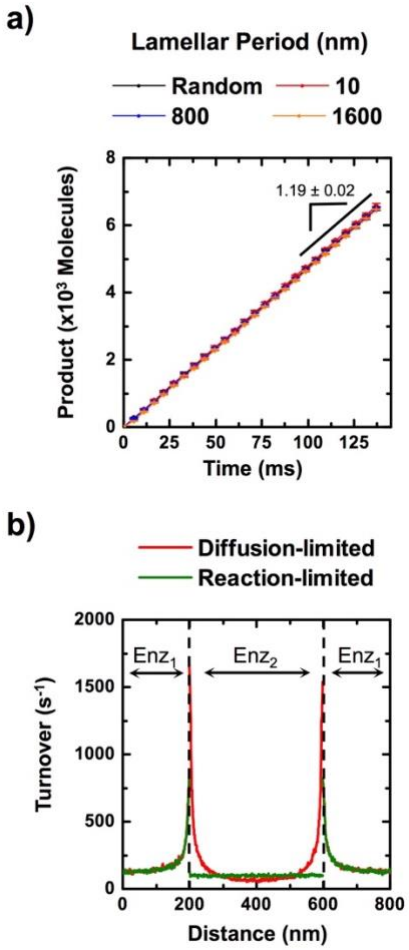

Figure 5.7 Cascade activity under reaction-limited conditions as a function of pattern period for enzymes immobilized on surfaces in random and lamellar arrangements. (**a**) Cumulative product formation as a function of simulation time and enzyme spatial arrangement. Each curve is the average of four independent simulations, with error bars reported as one standard deviation. (**b**) Average enzyme turnover as a function of position for the 800 nm period lamellar spatial arrangement under diffusion- and reaction-limited conditions. A total enzyme density of 240 x 10^{-4} enzymes/nm^2 and 1:1 ratio of Enz_1 to Enz_2 was used for all enzyme arrangements.

5.4.4 Isolated Pairs of Enzymes, Multi-enzyme Cascades, and Other Considerations

Although the influence of enzyme arrangement on cascade activity was minimal for densely packed systems, there was a significant difference for cascades involving isolated pairs of enzymes (**Figure 5.8a**). The diffusion characteristics of S and I along the surface are the same here as in densely packed systems, but for isolated enzyme pairs, it was significantly more difficult for I to find Enz_2, resulting in the accumulation of I in the simulation. The rate of I formation is the same for all cases, but, as shown in **Figure 5.8b**, the fraction of I converted to P scaled inversely with the distance between Enz_1 and Enz_2. These observations agree with results presented by Idan and Hess,[101] in which it was shown that the majority of P is formed from I that effectively diffuses from the bulk to Enz_2, rather than directly from Enz_1. This isolated arrangement of enzymes is relevant for many situations, and can be used to describe the behavior of enzymes immobilized on DNA scaffolds[27,207] and cases where the surface coverage of enzymes is extremely sparse. Notably, changes in the orientation of the active sites of isolated enzyme pairs would presumably impact the cascade activity, as observed previously, by altering the effective inter-enzyme distance.[208] Additionally, the magnitude of the apparent rate enhancement for the isolated case upon reducing the distance between Enz_1 and Enz_2 was similar to that observed experimentally.[27]

Our observations highlight the cumulative nature of the effect of inter-enzyme distance on the overall activity of the cascade. An understanding of this effect may be extrapolated to consider the impact of spatial arrangement on biocatalytic cascades with more than two enzymes. For example, when there are more than two reaction steps, one would expect the activity of the patterned case to be significantly less than that for the random case. The decrease in relative activity may be described by a power law relationship where the power is equivalent to the number of intermediate in the cascade. However, this decrease in activity as a result of molecular free diffusion may be overcome by channeling of intermediates between enzymes using electrostatic

bridges, attachment of intermediates to swinging arms,[209] or confinement in sub-cellular microenvironments.[210] As a result of channeling, the diffusion path length between enzymes is reduced, in effect creating a reaction-limited environment where the overall rate is not dictated by diffusion.

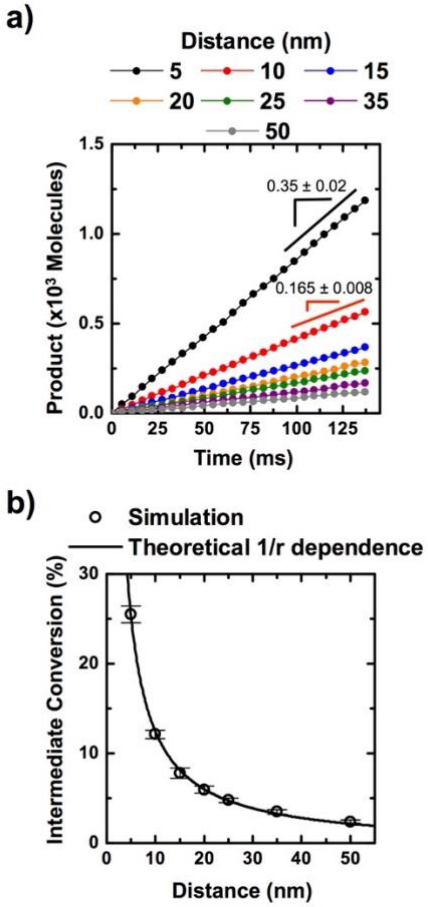

Figure 5.8 Cascade activity for a pair of isolated enzymes Enz_1 and Enz_2 with center to center distances of 5 to 50 nm under diffusion-limited conditions. (**a**) Cumulative product formation as a function of simulation time reported as the average of four independent simulations. (**b**) Relative fraction of I generated that is converted to P as a function of the distance between isolated enzymes Enz_1 and Enz_2. The error bars indicate one standard deviation of the simulation results.

While the cases presented here consider an equal number of each enzyme in a cascade, it is also of interest to briefly discuss the effects of imbalances in enzyme stoichiometry. For the

diffusion-limited case, the activity is determined by the path length required for S and I to encounter any Enz_1 and Enz_2 sites, respectively, which is related to the surface coverage of each enzyme. Imbalances in enzyme stoichiometry that alter the surface coverage of each enzyme (while maintaining a constant total surface enzyme density) result in increased distances that S or I must travel to encounter the enzyme with the lowest surface coverage, and therefore, as shown in **Figure A.9**, a marginal decrease in overall cascade activity. However, the activity of a reaction-limited cascade is determined primarily by the turnover number of the slowest enzyme and, as such, is less sensitive to changes in the required distance traveled by S and I. Thus, it is possible to increase the cascade activity by increasing the ratio of slow to fast enzymes immobilized on the surface, with an optimum existing when the total throughput of each enzymatic step of the cascade is equivalent. For example, as shown in **Figure A.10** for a reaction-limited system where Enz_1 and Enz_2 have turnover numbers of 10 and 100 s^{-1}, respectively, the cascade activity on a surface with a stoichiometric ratio of Enz_1 and Enz_2 (*i.e.*, $[Enz_1]:[Enz_2] = 1:1$) is significantly lower than that on a surface with enzyme stoichiometry of $[Enz_1]:[Enz_2] = 10:1$. These conclusions about optimizing immobilized enzyme stoichiometry, assuming constant total enzyme surface coverage, hold independent of the spatial arrangement of the enzymes for reaction-limited cascades.

5.5 Conclusions

In conclusion, kinetic Monte Carlo simulations of an enzyme cascade on a two-dimensional scaffold revealed spatial organizations of the enzymes that lead to enhanced overall reaction rates. The greatest rates were observed when the enzymes were positioned most closely, which was realized when arranged randomly and at high densities on the scaffold surface. These results bring into question the rationale for using sophisticated patterning techniques to control the spatial arrangement of densely packed enzymes. However, control of the orientation and position of

isolated enzyme pairs on the length-scale of the enzymes (*i.e.*, 1-10 nm), which effectively reduces diffusional constraints, is critical for enhancing cascade throughput, as reported previously.[27,101,196] In addition to biological cascades, these conclusions also apply to cascades involving inorganic heterogeneous catalysts such as tandem metal–metal oxides.[76,211] Furthermore, our findings may be extended to spherical or cylindrical compartments where dense packing and close arrangement of the catalytic sites is desirable for optimal activity. Our conclusions ultimately have important practical implications for the design of catalytic cascades on scaffolds and may simplify the engineering of such systems.

5.6 Acknowledgements

This material is based upon work supported by the National Science Foundation Graduate Research Fellowship under Grant No. DGE 1144083 (G.R.C.).

Chapter 6: Modification of Lipase with Poly(4-acryloylmorpholine) Enhances Solubility and Transesterification Activity in Anhydrous Ionic Liquids

Adapted from Biomacromolecules 19, 1324-1332

6.1 Abstract

Tuning the molecular interaction between enzymes and their solvent environment through polymer modification can greatly improve activity and thus utility in biocatalytic reactions. In this work, this approach was exploited to enhance the activity of lipase A (LipA) from *Bacillus subtilis* in anhydrous ionic liquids (IL), which are highly attractive solvents for biocatalysis. Specifically, we showed that the transesterification activity of LipA in anhydrous 1-butyl-3-methyl imidazolium hexafluorophosphate ([BMIM][PF_6]) was improved up to 19-fold via covalently conjugating the enzyme with the IL-soluble polymer poly(4-acryloylmorpholine) (PAcMO). The increase in transesterification activity correlated with an increase in LipA solubility in [BMIM][PF_6] as well as, notably, the number of conjugated PAcMO repeat units. Light scattering results further showed that the attachment of PAcMO disrupted the aggregation of LipA in aqueous buffer, which was used as a proxy to understand the mechanism of activation of LipA in IL, where aggregation was more pronounced. Additionally, using static light scattering, the Flory-Huggins interaction parameter (χ) for the polymer-IL interactions was determined (0.457). The favorable PAcMO-IL interactions presumably compensated for the unfavorable interactions between the enzyme and IL, which resulted in the improvement in dissolution and, in turn, activity due to reduced diffusional limitations. Through rationally considering χ, a similar approach may be used to tune the molecular interaction between other enzymes and ILs with other polymers, which has widespread implications for the enhancement of biocatalysis in ILs.

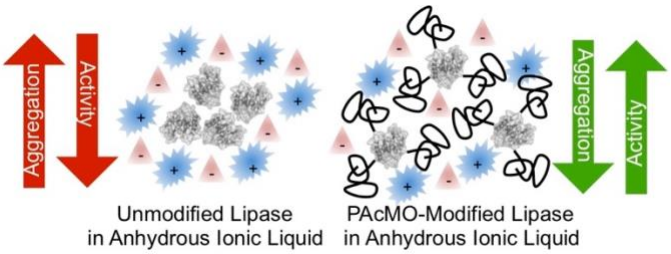

Figure 6.1 Graphical abstract: Covalent attachment of ionic liquid-soluble PAcMO to lipase improves solubility and activity of the enzyme in anhydrous ionic liquids.

6.2 Introduction

Although inherently delicate, enzymes are robust catalysts that function in a broad range of solvent environments, including non-aqueous media. By using non-aqueous solvents as media for biocatalytic reactions, the portfolio of feasible biotransformations may be greatly expanded.[28,107,212] The portfolio of such reactions has been even further broadened by the now decades old reports that enzymes retain activity in anhydrous ionic liquids (ILs).[30,116,117,213–216] However, while the benefits of ILs as solvents for non-aqueous biocatalysis have been well documented,[31,212,217,218] enzyme activity in ILs, like other non-aqueous solvents, is generally low. One of the dominant factors that contributes to low activity of enzymes in anhydrous hydrophobic ILs that generally support enzyme activity is poor solubility of the enzyme.[219] As a result, the dry (*i.e.*, lyophilized) enzyme is typically suspended as large aggregates in the IL, which effectively reduces the concentration of enzyme that is accessible to the substrate and only enzyme molecules on the outside of the aggregates catalyze the reaction. Additionally, because the substrate must diffuse from the bulk solvent to the surface of the enzyme aggregate, the activity of the enzyme may be hindered by mass transfer limitations.

Several approaches have been investigated to improve the solubility of enzymes in hydrophobic ILs, including covalent modification with amphiphilic polymers,[149,220–223] complexation with surfactants,[143,224] and entrapment in reverse micelles.[135–137] While these approaches have been investigated in ILs, their success has largely been limited and effective in

only isolated cases. For example, Nakashima and co-workers[149] reported that the covalent crosslinking of subtilisin with a comb-shaped poly(ethylene glycol) (PEG) enhanced the solubility of the enzyme in imidazolium ILs with the bis(trifluoromethylsulfonyl)imide anion, despite the large molecular weight of the PEG-modified crosslinked enzyme (~1 MDa). However, notably, the attachment of PEG has proven ineffective in solubilizing and boosting the activity of enzymes in other ILs.[31,225] More recently, Brogan and Hallet[143] showed that the formation of a non-covalent complex between an oligomeric PEG-based surfactant and cationized myoglobin increased the solubility of myoglobin, which is catalytically inactive, in pyrrolidinium ILs without perturbing the structure of myoglobin. However, previous work has shown that enzymes are inactivated by pyrrolidinium ILs[31] and the non-covalent nature of the complexes present challenges for use in biocatalysis since the surfactant could dissociate from the enzyme surface. Furthermore, Moniruzzaman and co-workers[135] demonstrated the solubilization of lipase and horseradish peroxidase in water-in-IL microemulsions and that the enzymes upon dissolution were active and stable. Despite this success, the activity of enzymes using this approach may be subject to partitioning of the substrate between the bulk IL and aqueous domain containing the enzyme.

While covalently tethering polymers to enzymes provides a promising approach to dissolving enzymes in ILs, very few different polymer chemistries for this purpose have been explored. As noted above, in virtually all cases, PEG or PEG-containing polymers have been used in this context,[149,220–223] leaving a vast wealth of possible polymer chemistries to be explored. Using different chemistries may allow the molecular-level interactions between the enzyme and IL to be more carefully tuned, resulting in enhanced thermodynamic solubility and, in turn, activity. Of direct relevance to this, the synthesis and identification of IL-soluble polymers for use in ion gels for gas separations and ion-conducting electrolyte membranes for battery and fuel cell

applications has received considerable attention.[34,35,226–228] A polymer that has been identified with high solubility in the hydrophobic IL 1-butyl-3-methyl imidazolium hexafluorophosphate ([BMIM][PF_6]), which is widely used for biocatalysis, is poly(4-acryloylmorpholinone) (PAcMO). This polymer was identified as soluble by screening 24 different polymers in four commonly used ILs.[229] Although the exact mechanism for solubility of PAcMO in ILs is unknown, the carbonyl oxygen of the amide bond in the acrylamide backbone may presumably hydrogen bond with the acidic hydrogen in the C_2 position of the imidazolium ring.[230] Given the high solubility of PAcMO in [BMIM][PF_6], it is interesting to consider its use to solubilize enzymes when covalently attached to the enzyme surface.

In this work, we investigated the covalent modification of enzymes with PAcMO as a novel strategy to enhance the solubility and overall activity of enzymes in hydrophobic ILs. This strategy was investigated using lipase A (LipA) from *Bacillus subtilis* as a model enzyme, which has been shown to catalyze alcoholysis reactions in the absence of bulk water, and has been used as a model enzyme to study the effects of ILs on enzyme structure and stability.[231,232] Using LipA as a model enzyme, the molecular weight of PAcMO and extent of functionalization of LipA were varied to study their effects on conjugate solubility and enzymatic activity in [BMIM][PF_6]. The impact of polymer length and the number of attached chains was analyzed via measuring the transesterification activity of LipA, which otherwise catalyzes the hydrolysis of esters in water. The enhancement in transesterification activity was correlated with increased solubility of LipA-PAcMO conjugates, which was dependent on the number of PAcMO repeat units on the enzyme. Additionally, light scattering was used to determine the impact of PAcMO modification on the colloidal stability of LipA, as well as the interactions of PAcMO with [BMIM][PF_6]. Our results

highlight the potential utility of PAcMO modification for tuning the molecular interactions between enzymes and ILs, which has widespread implications for biocatalysis.

6.3 Materials and Methods

Materials

4-cyano-4-(phenylcabonothioylthio)pentanoic acid N-succinimidyl ester, 2,2'-azobis(2-methylpropionitrile), 4-acryloylmorpholine (97%), 1,4-dioxane (anhydrous, 99.8%), 1-butyl-3-methylimidazolilum hexafluorophosphate (97%), molecular sieves (3 Å), toluene (≥99.5%) and 4-nitrophenyl butyrate (98%) were purchased from Sigma Aldrich. Ethanol (200 proof) was purchased from Decon Labs. Diethyl ether (99%) was purchased from BDH Chemicals. Chloroform (99.8%) was purchased from EMD Millipore. Reagents for the bicinchoninic acid assay and 2,4,6-trinitrobenzene sulfonic acid were purchased from Thermo Fischer Scientific. The gene encoding lipase A (LipA) from *B. Subitilis* was PCR-amplified from genomic DNA, which was kindly provided by Dr. Robert Batey (University of Colorado Boulder).

LipA Expression and Purification

LipA with a C-terminal polyhistidine tag was expressed in BL21 DE3 *E. coli* cells using ampicillin as a selective marker. Transformed cells were grown in LB to an OD of ~0.7 at 37 °C at 200 rpm and subsequently induced at 25 °C with 1 mM IPTG for 24 h. Cells were then harvested via centrifugation and lysed by homogenization in lysis buffer containing 50 mM sodium phosphate (pH 7.9), 200 mM sodium chloride, 5 mM imidazole, and 3 vol% glycerol. The resulting lysate was clarified by centrifugation and filtered with a 0.22 μm PES vacuum filter (Corning Inc.) before loading onto a Ni^{2+}-charged Bio-Scale Mini immobilized metal affinity chromatography cartridge (Bio-Rad). The enzyme was eluted in the same lysis buffer containing 250 mM imidazole

and subsequently dialyzed to remove imidazole prior to use. Enzyme concentration was determined using the bicinchoninic acid assay and corroborated by measuring optical density at 280 nm at which the theoretical molar extinction coefficient of the enzyme is 24,410 M^{-1} cm^{-1}.

Synthesis of NHS-terminated Poly(4-acryloylmorpholine)

N-hydroxysuccinimide (NHS)-terminated PAcMO was synthesized by RAFT polymerization using 4-cyano-4-(phenylcabonothioylthio)pentanoic acid N-succinimidyl ester as the chain transfer agent (CTA) and 2,2'-azobis(2-methylpropionitrile) (AIBN) as the radical initiator. Prior to polymerization, the AcMO monomer was purified on an alumina column to remove MeHQ inhibitor. Additionally, AIBN was recrystallized from methanol prior to use. Target molecular weights were calculated from the ratio of monomer to CTA. AcMO (0.728 M, 1.47 M, or 2.45 M), AIBN, and CTA were dissolved in anhydrous 1,4-dioxane at a 10:1 ratio of CTA to AIBN in Schlenk flasks. Oxygen was removed from the Schlenk flasks by three freeze-pump-thaw cycles. After the last freeze-pump-thaw cycle, the flasks were equilibrated to room temperature and submerged for 48-72 h in oil baths at 70 °C with mixing at 300 rpm. The resulting polymers were purified by precipitation into diethyl ether. Due to the high viscosity of the large molecular weight polymers, these samples were diluted in chloroform prior to precipitation in ether. Final products were obtained as powders by filtration and ranged in color from pink to off-white, depending on the molecular weight of the samples. Molecular weights and polydispersity index (PDI) of the polymers were determined by gel-permeation chromatography using an EcoSEC HLC-8320GPC (Tosoh) and PMMA standards for calibration.

Synthesis and Characterization of LipA-PAcMO Conjugates

To covalently modify LipA with PAcMO, NHS-PAcMO was added to LipA solutions (0.1 mg ml^{-1} in 50 mM sodium phosphate, pH 7.9, 200 mM sodium chloride, 3 vol% glycerol) at a 20:1 molar ratio of polymer-to-primary amine. The reaction was incubated at room temperature for 1 h with agitation (100 rpm) on a shaking table. Excess polymer was removed by conjugate purification by affinity chromatography using the same Ni^{2+}-IDA columns that were used for purification of LipA from cell lysate. Purified conjugates were then eluted with lysis buffer containing 250 mM imidazole and dialyzed to remove imidazole prior to further use. The concentration of enzyme in the conjugate samples was determined by bicinchoninic acid assay for which controls showed that the free polymer did not interfere with the assay results. To confirm and determine the extent of polymer modification, purified LipA-PAcMO conjugates were characterized by SDS-PAGE and the TNBSA assay. For SDS-PAGE analysis, enzyme samples were stained with either Coomassie or the fluorescent InVision™ stain (Thermo Fischer), which binds specifically to the polyhistidine tag of modified or unmodified LipA. For the TNBSA assay, a calibration curve of the number of free primary amines per enzyme molecule was generated using glycine as a standard. The extent of labeling was quantified by the loss of primary amines.

Hydrolysis of 4-nitrophenyl Butyrate

The activity of LipA and LipA-PAcMO conjugates in aqueous buffer was measured via monitoring the enzyme-catalyzed hydrolysis of 4-nitrophenyl butyrate. The initial rate of the hydrolysis of 4-nitrophenyl butyrate was specifically monitored by measuring the release of 4-nitrophenol spectrophotometrically at 420 nm over 1-5 mins at room temperature using an Evolution 260 Bio UV-Visible spectrophotometer (Thermo Scientific). The enzyme-catalyzed

reaction, which was monitored continuously in a 1 mL cuvette, was initiated via the addition of LipA or LipA-PAcMO (0.1-2.0 μg mL^{-1} final concentration) to a solution of 4-nitrophenyl butyrate (3 mM) in buffer (100 mM sodium phosphate, pH 8.0). Activity was quantified as the slope of the linear fit to the absorbance versus time data.

Transesterification of 4-nitrophenyl Butyrate with Ethanol

The activity of LipA and LipA-PAcMO conjugates was measured in [BMIM][PF_6] by monitoring the enzyme-catalyzed transesterification reaction between 4-nitrophenyl butyrate (100 mM) and ethanol (1 M, dried with 3 Å molecular sieves). LipA and LipA-PAcMO conjugates were lyophilized from 5 mM sodium phosphate (pH 8.0) for 24 h. Lyophilized powder was dissolved in [BMIM][PF_6] at 90 °C under vigorous mixing for 10 min. Water content was measured by Karl Fischer titration to be 0.081 ± 0.001 wt.% H_2O (59.7 ± 0.7 mM H_2O) (DL32 Coulometric KF Titrator, Mettler Toledo). The activity of LipA was measured at 1 mg mL^{-1} final enzyme concentration, while the activities of all LipA-PAcMO conjugates were measured at a final enzyme concentration of 0.1 mg mL^{-1}. The absorbance coefficient of nitrophenol was measured to be $\varepsilon_{420} = 0.697\ \mathrm{mM^{-1}\ cm^{-1}}$ in [BMIM][PF_6].

Dynamic Light Scattering Measurements

Dynamic light scattering (DLS) and static light scattering (SLS) was measured using a Litesizer™ 500 (Anton Paar). For DLS analysis of LipA-PAcMO conjugates, samples were prepared between 0.05 and 0.15 mg mL^{-1} enzyme in a 50 mM sodium phosphate (pH 7.9), 200 mM sodium chloride, and 3 vol% glycerol solution and filtered with a 0.1 μm PVDF filter prior to analysis (Durapore, Merck Millipore Ltd.). For DLS analysis of free polymer, PAcMO solutions

were prepared between 1 and 10 mg mL^{-1} in [BMIM][PF_6] and filtered with a 0.1 μm PVDF filter prior to analysis. Each data point consisted of at least six independent measurements of 10 s each. Histograms are shown as intensity-weighted size distribution.

Static Light Scattering Measurements

The second virial coefficient (A_2) was measured by Static Light Scattering (SLS) using a Litesizer™ 500 (Anton Paar). Debye plots were generated by measuring SLS intensity at a fixed angle $\theta = 90^{\circ}$ and fitting data to the following equation:

$$\frac{KC}{R_\theta} = \frac{1}{M_W} + 2A_2C$$

where R_θ is the excess Rayleigh ratio, C is the polymer concentration, M_W is the weight-average molecular weight of the polymer, and K is a constant defined by:

$$K = \frac{4\pi^2 n_0^2 (\frac{dn}{dc})^2}{N_A \lambda_0^4}$$

where n_0 is the index of refraction of the solvent, n is the index of refraction of the solution containing solute, λ_0 is the wavelength of incident laser light, and N_A is Avogadro's number. $dn/_{dc}$ of PAcMO in [BMIM][PF6] was measured as 0.1026 mL g^{-1} using an Abbe Mark II digital refractometer (Reichert-Jung). The Flory-Huggins interaction parameter (χ) was then calculated from the second virial coefficient:

$$\chi = \frac{1}{2} - \frac{\bar{V}_s}{(\rho_p^0)^2} A_2$$

where ρ_P^o is the density of the polymer, $\bar{V}_S$ is the partial specific volume of solvent, and A_2 is the second virial coefficient. Values of $\rho_P^o = 1.14\ \frac{g}{mL}$ and $\bar{V}_{[BMIM][PF_6]} = 208.3\ \frac{mL}{mol}$ were used.[233]

Polymer samples (M_n = 36.3 kg mol^{-1}, M_W = 41.9 kg mol^{-1}, PDI = 1.15) were prepared at various concentrations from 2.5 to 25 mg mL^{-1} and filtered with a 0.1 μm PVDF filter prior to analysis. Toluene was used as the reference material. The weight-averaged molecular weight was calculated as 49.0 kg mol^{-1} in [BMIM][PF_6], in good agreement with the weight-averaged molecular weight obtained by GPC.

6.4 Results and Discussion

6.4.1 Conjugate Synthesis and Characterization

To investigate the utility of PAcMO in solubilizing LipA in [BMIM][PF_6], PAcMO was initially synthesized by reversible addition fragmentation chain transfer (RAFT) polymerization. By using RAFT, a controlled radical polymerization method, the molecular weight and polydispersity of PAcMO could be precisely tuned. Briefly, PAcMO was synthesized using an NHS-modified dithiobenzoate chain transfer agent (CTA) and AIBN as a radical initiator in anhydrous 1,4-dioxane at 70 °C (**Figure 6.2**). Molecular weight was controlled by varying the ratio of CTA-to-AcMO monomer with a constant 10:1 molar ratio of CTA-to-initiator. Using these conditions, we synthesized PAcMO polymers with varying molecular weights, which ranged from 4.7 to 114 kg mol^{-1}, and had a PDI ≤ 1.20 as determined by GPC (**Table 6.1**). Additionally, the resulting polymers had a terminal NHS moiety, allowing for covalent attachment of polymer and LipA through the reaction of surface-accessible primary amines from lysine residues or the N-terminus of LipA. Similar "grafting to"[153,234] as well as "grafting from"[235] schemes in which the polymer is grown from the surface of the enzyme via RAFT by first attaching the CTA to the enzyme have been reported previously.

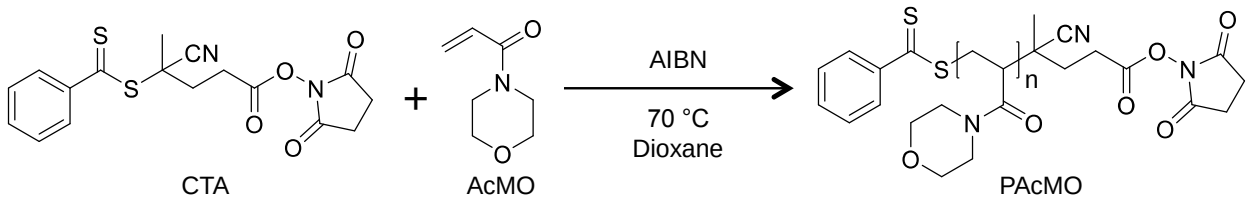

Figure 6.2 Overview of the synthesis of NHS-terminated PAcMO by RAFT polymerization.

Table 6.1 Polymerization conditions and characterization of PAcMO.

Polymer Sample Name	Concentrations $[I]_0:[CTA]_0:[M]_0$	Polymer M_n[a] (kg mol^{-1})	PDI[a]	Degree of Polymerization[b]
PAcMO-5k	0.1:1:40	4.7	1.07	31
PAcMO-10k	0.1:1:85	10.4	1.09	71
PAcMO-20k	0.1:1:180	20.2	1.10	140
PAcMO-36k	0.1:1:363	36.3	1.15	254
PAcMO-73k	0.1:1:709	72.6	1.15	512
PAcMO-114k	0.1:1:1476	114.0	1.20	805

[a]: Polymer molecular weight and PDI measured by GPC. [b]: Calculated from polymer, chain transfer agent, and repeat unit molecular weights.

Having synthesized PAcMO with varying molecular weights, the PAcMO polymers were reacted with LipA using a molar ratio of 20:1 polymer chains per reactive site (*i.e.*, primary amine) as shown in **Figure 6.3.** Importantly, while soluble in [BMIM][PF_6], PAcMO is also water soluble, which permitted the straightforward synthesis of LipA-PAcMO conjugates directly in aqueous buffer. After the conjugation reaction, LipA-PAcMO conjugates were purified via affinity chromatography by exploiting the C-terminal 6xhis tag fused to the recombinant LipA construct. Notably, the covalently attached polymer did not completely prevent binding of LipA-PAcMO conjugates through the 6xhis tag. Using this purification approach, the recovery of LipA-PAcMO conjugates ranged from >50% to 20% and was inversely correlated with the polymer chain length.

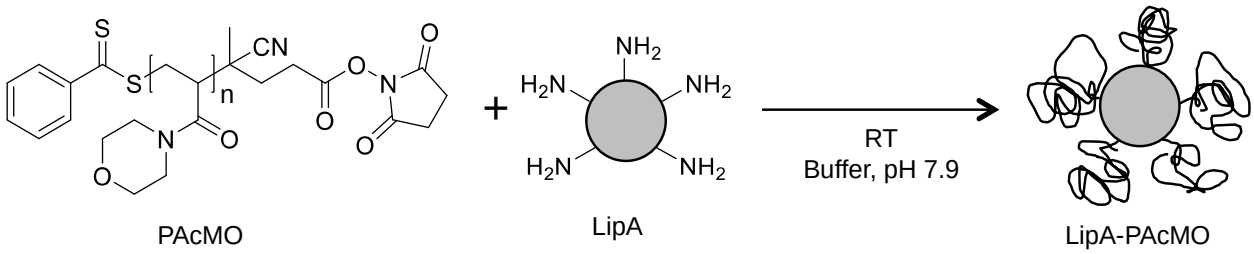

Figure 6.3 Conjugation of NHS-terminated-poly(4-acrylolymorpholine) to lipase A by NHS-amine coupling.

Analysis of the number of residual unreacted amine groups in LipA upon conjugation showed that, for each polymer, the number of attached polymers per enzyme was between 3 and 6.3 (**Table 6.2**). As expected, the number of attached polymers per enzyme was smallest for the highest molecular weight polymer and greatest for the smallest molecular weight polymer. This trend is consistent with the presumed impact of steric effects due to polymer size on the number of attached polymers per enzyme molecule. Notably, LipA has 12 primary amines, though only six of the lysines and the N-terminal amine are solvent accessible (as defined by having a solvent accessible surface area of >30% based on structural analysis using the Swiss-PDB Viewer) and thus likely to react with the polymer. Based on this, for the smallest molecular weight polymer, nearly all of the reactive amines were on average modified per enzyme molecule. Moreover, based on the number of attached polymers per conjugate and the molecular weight of each polymer, the theoretical total number of conjugated PAcMO repeat units increased with the size of the polymer reacted with the enzyme.

To further confirm the extent of modification upon conjugation with PAcMO, the LipA-PAcMO conjugates were analyzed by SDS-PAGE. For SDS-PAGE analysis, the LipA-PAcMO conjugates were stained with Coomassie (**Figure 6.4a**) as well as a fluorescent dye (**Figure 6.4b**), which has ultra-low background binding. Notably, in both gel images, the fraction of residual unmodified enzyme in each conjugate was negligible. Additionally, although the trend in the

increase in molecular weight of the conjugates was also consistent with that expected based on polymer size, the size and distribution of attached polymers could not be quantified due to smearing of the bands in lanes with the conjugates. Such smearing may be attributed to the impact of polymer attachment on SDS binding and electrophoretic mobility.

Table 6.2 Characterization of the extent of modification of LipA-PAcMO conjugates.

Conjugate Sample Name	Polymer M_n[a] (kDa)	Number of Polymers Per Enzyme[b]	Theoretical Total Molecular Weight (kDa)[c]	Theoretical Total Number of Repeat Units[d]
LipA	---	0	20.3	0
LipA-5k	4.7	6.3 ± 0.3	50 ± 1	196 ± 9
LipA-10k	10.4	5.4 ± 0.1	76 ± 1	383 ± 4
LipA-20k	20.2	4.7 ± 0.5	120 ± 10	660 ± 70
LipA-36k	36.3	6 ± 1	240 ± 40	1500 ± 200
LipA-73k	72.6	4.6 ± 0.4	350 ± 30	2400 ± 200
LipA-114k	114.0	3.0 ± 0.1	360 ± 10	2420 ± 80

[a]: Polymer molecular weight measured by GPC. [b]: Measured by TNBSA assay. [c]: Calculated using the measured number of polymers per enzyme, polymer molecular weight, and molecular weight of unmodified LipA. [d]: Calculated using the measured number of polymers per enzyme and number of repeat units per polymer.

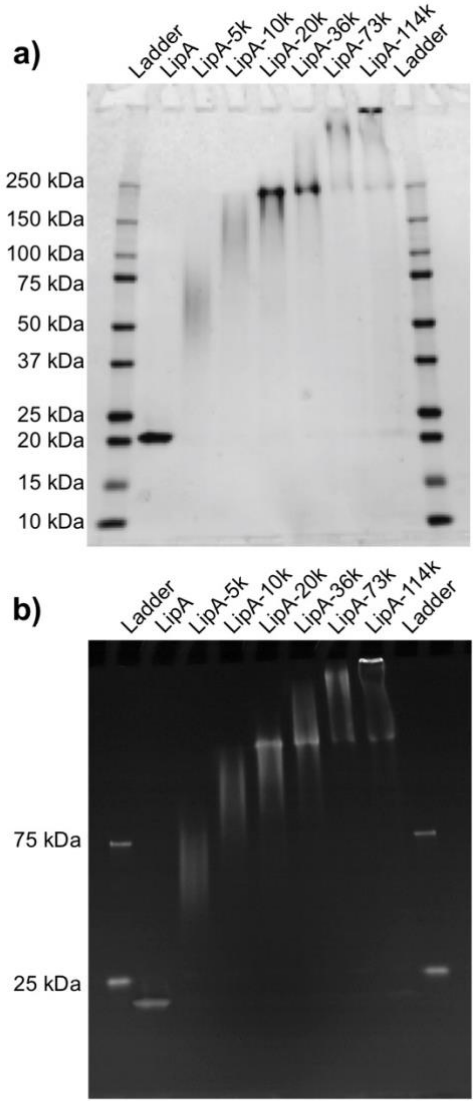

Figure 6.4 SDS-PAGE analysis of LipA and LipA-PAcMO conjugates stained with: a) Coomassie and b) InVision™ His-Tag In-Gel Stain. The InVision™ His-Tag In-Gel Stain is a fluorescent stain that specifically targets the C-terminal 6xhis-tag fused to LipA and LipA-PAcMO conjugates. Upon fluorescent staining, the gel was imaged using an excitation wavelength of 560 nm and emission wavelength of 590 nm. The 75 kDa and 25 kDa bands in the ladder are visible because they are intrinsically fluorescent.

6.4.2 Effect of PAcMO Modification on Transesterification Activity of LipA

To determine the impact of PAcMO modification on LipA activity in [BMIM][PF_6], the lipase-catalyzed transesterification of 4-nitrophenyl butyrate with ethanol was used as a model reaction. Specifically, the initial rate of the transesterification of 4-nitrophenyl butyrate with ethanol was measured spectrophotometrically for each of the conjugates as well as unmodified

LipA. We hypothesized that, given the solubility of PAcMO in [BMIM][PF_6], modifying LipA with PAcMO would reduce the aggregation of LipA in [BMIM][PF_6], thereby increasing activity. The solubility of LipA-PAcMO conjugates in [BMIM][PF_6] is presumably a result of the balance of favorable PAcMO-IL interactions and unfavorable LipA-IL interactions. As the extent of favorable PAcMO-IL interactions are increased relative to the unfavorable LipA-IL interactions, the solubility of the conjugates would be expected to increase. Therefore, conjugates with more total PAcMO repeat units were expected to be more soluble and have greater transesterification activity. Additionally, since LipA is insoluble in [BMIM][PF_6], even modest changes to conjugate solubility would presumably result in a large increase in transesterification activity. Cummings and co-workers[148] reported a similar approach to improve the molecular dissolution of chymotrypsin in acetonitrile. In this work, chymotrypsin was modified with poly(2-(dimethylamino)ethyl methacrylate) via a grafting-from approach, which resulted in substantial enhancement of chymotrypsin activity. Interestingly, the modified enzyme was also at least partially soluble in dichloromethane, chloroform, tetrahydrofuran, and acetone. The attachment of polymers that tune the interaction of proteins with aqueous environments[169,236–238] as well as stabilize enzymes through enzyme-polymer interactions[239–241] has also been reported. In related work, Chen and co-workers[242] also directly coupled poly(methacryloyloxyethylphosphorylcholine) to lysozyme in imidazolium ILs, which provided a favorable solvent environment for the zwitterionic polymer.

As hypothesized, the modification of LipA with PAcMO resulted in a dramatic increase in the transesterification activity of LipA in [BMIM][PF_6] relative to that of unmodified LipA (**Figure 6.5**). Modification of LipA with PAcMO-5k, in particular, resulted in an 8-fold increase in activity of the unmodified enzyme. This increase upon attachment of PAcMO-5k confirmed that

the conjugation of even a relatively small number of PAcMO repeat units had a significant impact on activity. As the total number of conjugated PAcMO repeat units increased for the larger conjugates, a further enhancement in activity was observed. The maximum enhancement in transesterification activity over the unmodified enzyme was observed for the LipA-114k conjugate (with the largest number of conjugated PAcMO repeat units), which amounted to a 19-fold increase in relative activity. The correlation between activity and number of conjugated PAcMO repeat units was presumably due to an increase in the fraction of the enzyme that was soluble in the IL. The fraction of soluble enzyme for the conjugates appeared to near a maximum for the largest conjugates, whereby increasing the number of PAcMO repeat units had a diminishing effect. Such a diminishing effect suggested that above a critical threshold, the addition of conjugated PAcMO repeat units had a reduced impact on the extent of PAcMO interactions with the IL.

While such enhancements in rate were observed for the transesterification activity of LipA upon PAcMO modification, such enhancements were markedly smaller in aqueous buffer (**Figure 6.5**). Compared to in [BMIM][PF_6], the relative hydrolysis activity of the LipA-PAcMO conjugates was only approximately 2-fold higher than that of unmodified LipA. Hydrolysis activity of LipA was measured in buffer using the same substrate (*i.e.*, 4-nitrophenyl butyrate) as was used in transesterification assays. The increase in the relative hydrolysis activity of LipA upon PAcMO modification was presumably due to the increase in colloidal stability of LipA, which tends to aggregate in buffer. Specifically, as in [BMIM][PF_6], modification of LipA with PAcMO reduced the extent of aggregation of LipA, which, in turn, increased the effective concentration of active LipA. However, given that the tendency to aggregate is greater in [BMIM][PF_6] compared to as in buffer, it is not surprising that the enhancement in activity was smaller in buffer relative to

in the IL. Of note, while the relative activity of the LipA-PAcMO conjugates was greater than that of unmodified LipA in buffer, the relative activity of the conjugates did not appear to depend significantly on the number of total PAcMO repeat units present in the conjugate (*i.e.*, the relative activity of the all of the conjugates was similar).

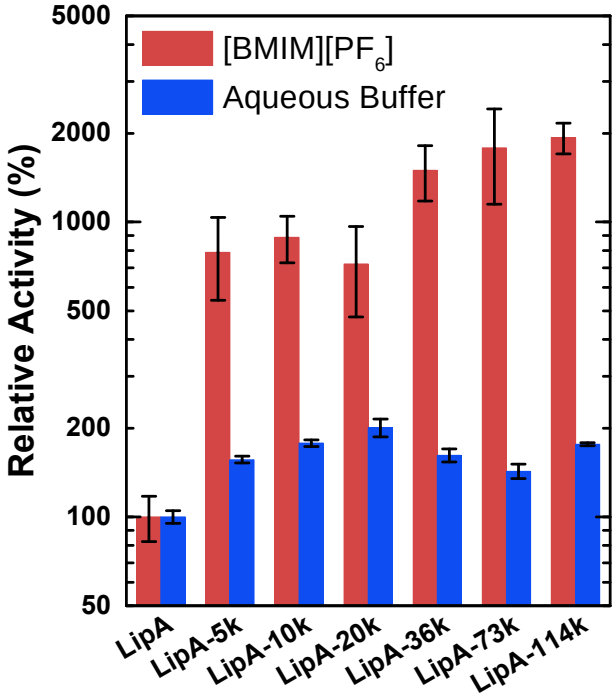

Figure 6.5 Relative activity of LipA-PAcMO conjugates compared to LipA. Transesterification activity (red) was determined in [BMIM][PF_6] at room temperature with 100 mM 4-nitrophenyl butyrate and 1 M ethanol. Hydrolysis activity (blue) was determined in 100 mM sodium phosphate buffer pH 8.0 with 3 mM 4-nitrophenyl butyrate. Error bars indicate one standard deviation for $n \geq 3$ separate experiments.

6.4.3 Solubility of LipA-PAcMO Conjugates in [BMIM][PF_6]

To confirm the impact of PAcMO modification on the solubility of LipA in [BMIM][PF_6], the solubility of the LipA-PAcMO conjugates in the IL was directly measured. Conjugate solubility in the IL was measured and compared to that of unmodified LipA by observing the sedimentation of the enzyme dispersed in the IL upon centrifugation. For unmodified LipA and smaller LipA-PAcMO conjugates, a pellet of insoluble enzyme was visually observed (**Figure**

6.6a). Conversely, for the largest LipA-PAcMO conjugates (*i.e.*, LipA-73k and LipA-114k), virtually no pellet was observed, indicating that the conjugates were mostly soluble, which correlated with the enhancement in activity observed previously. The extent of sedimentation was further quantified by measuring the difference in turbidity at 600 nm of the initial enzyme solution and the supernatant of the solution after sedimentation. **Figure 6.6b** shows the relative change (%) in optical density at 600 nm (ΔOD_{600}) for the unmodified and modified forms of LipA. As expected, ΔOD_{600} clearly decreased with increasing number of PAcMO repeat units in the conjugate, which is consistent with less sedimentation for the larger conjugates. The decrease in sedimentation with increasing number of conjugated PAcMO repeat units confirmed that the larger conjugates were indeed more soluble in the IL.

While the ΔOD_{600} generally correlated with the increase in relative transesterification activity of the LipA-PAcMO conjugates in [BMIM][PF_6], the ΔOD_{600} for LipA-5k as well as LipA-10k and unmodified LipA were virtually the same. This was particularly noteworthy since the relative transesterification activity of the LipA-5k and LipA-10k conjugates was considerably greater than that of unmodified LipA. As such, while the LipA-5k and LipA-10k conjugates still were aggregated in the IL, the size of the aggregates were likely much smaller than in the case of unmodified LipA. In this case, the aggregates of LipA-5k and LipA-10k would have a greater surface area, which, in turn, would correlate with an increase in the accessibility of active enzyme. Additionally, there was a sharp transition in ΔOD_{600} between LipA-36k and LipA-73k that was not reflected in the measured transesterification activity. A plausible explanation for this is that, while attachment of the 73k polymer enhanced solubility, such large polymers when attached to an enzyme may restrict enzyme dynamics, which are critical to substrate binding and turnover. It is also plausible that, due to a large polymer-rich corona around the enzyme, the larger polymers

impede substrate diffusion from the IL to the enzyme active site. Moreover, because the conjugates were lyophilized from buffer, buffer salts present in the conjugates, which did not dissolve in the IL, may have also contributed to the ΔOD_{600}. Such salts could not be removed entirely since they were required to maintain enzyme stability during and after polymer modification.

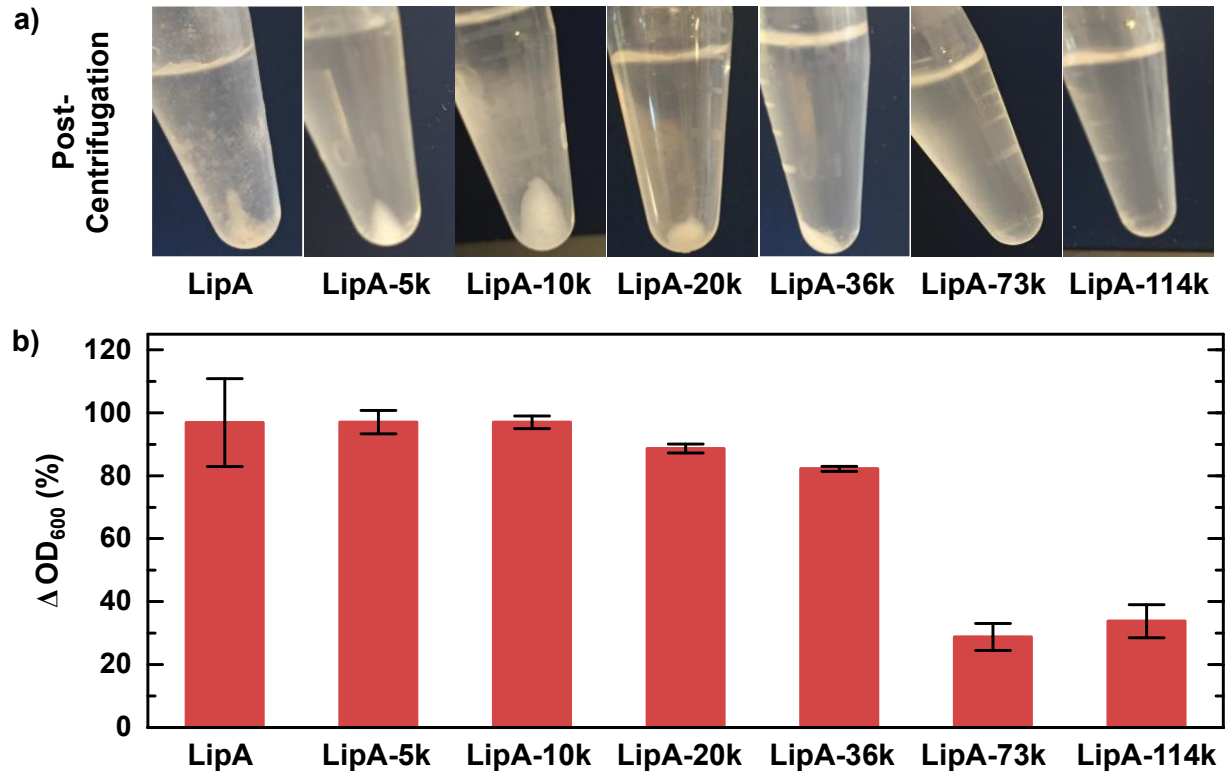

Figure 6.6 Solubility of LipA and LipA-PAcMO conjugates in [BMIM][PF_6]. a) Photographs of unmodified and PAcMO-modified LipA in [BMIM][PF_6] taken after centrifugation for 10 min at 16,873 g qualitatively show the amount of sedimentation of insoluble enzyme. For the unmodified LipA sample, an equivalent mass of enzyme to that of the mass of LipA-5k conjugate was used. b) Clarification of the suspension of unmodified and PAcMO-modified LipA in [BMIM][PF_6] was measured quantitatively by determining the relative change (%) in optical density at 600 nm (ΔOD_{600}) of each sample before and after centrifugation.

6.4.4 Effect of PAcMO Modification on LipA Aggregation

To further elucidate the impact of PAcMO modification on LipA solubility in [BMIM][PF_6], the size of LipA aggregates as a function of number of PAcMO repeat units was measured by DLS. While measuring the size of LipA aggregates in the IL was of particular interest,

characterization of LipA aggregates in the IL was not feasible by DLS due to the presence of insoluble buffer salts which themselves would appear as particles that were indistinguishable from the enzyme. Although this was not feasible, the impact of PAcMO modification on LipA aggregate size was characterized in aqueous buffer as a proxy for the effect in the IL.

Figure 6.7 shows the intensity-weighted distributions of radius measured by DLS for unmodified LipA and LipA-PAcMO conjugates in aqueous buffer. Unmodified LipA had a bimodal distribution with a small peak at 3.8 nm that represented monomeric enzyme and a larger peak at 73.4 nm that represented aggregated LipA. The extent of aggregation of LipA for the conjugates was reduced as the number of total PAcMO repeat units in the conjugates increased, which was evident by the disappearance of the larger peak. Specifically, the particle size distribution for the LipA-PAcMO conjugates gradually became unimodal, although the peak for the monomeric enzyme increased, which was expected because of the attached polymer chains. Notably, only a single peak was observed for the LipA-36k, LipA-73k, and LipA-114k conjugates, indicating that the level of aggregates in these conjugates was undetectable. These results confirm the disruption of large enzyme aggregates via PAcMO modification, and that the disruption of such aggregates was dependent on the size of the LipA-PAcMO conjugates. This dependence was presumably more pronounced in the IL, which would be consistent with the apparent increase in the activation of LipA in the IL relative to in buffer.

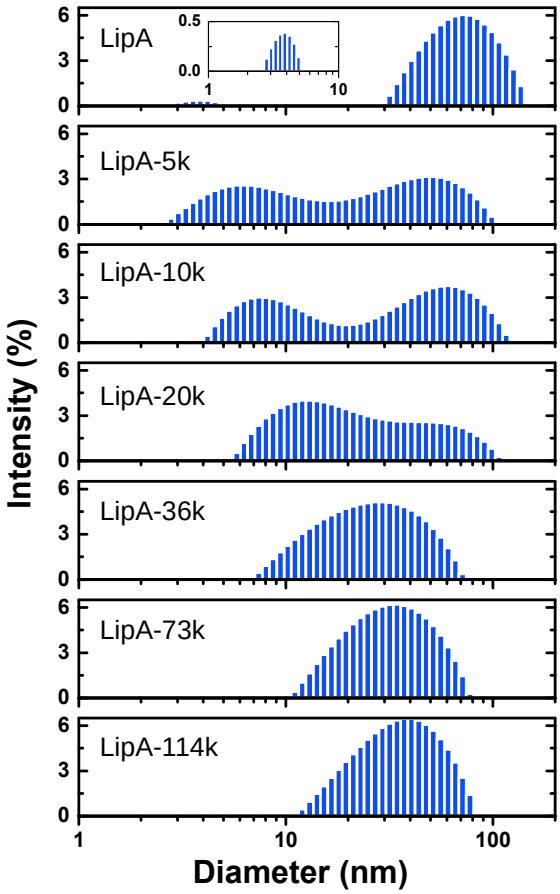

Figure 6.7 Intensity-weighted distributions of particle diameter for unmodified LipA and LipA-PAcMO conjugates in aqueous buffer measured by DLS. Inset in the unmodified LipA distribution is a magnification of the 1-10 nm diameter region. All samples were measured at 25 °C.

6.4.5 Characterization of the Molecular-level Interactions of PAcMO with [BMIM][PF$_6$]

The ability of the PAcMO polymer to solubilize the LipA conjugates depends primarily on the favorability of the molecular-level interactions between the polymer and its environment. The Flory-Huggins interaction parameter, χ, provides a good measure of the polymer-solvent interactions from which thermodynamic properties such as solubility arise. Static light scattering was used to measure an apparent $\chi = 0.457 \pm 0.003$ for PAcMO in [BMIM][PF$_6$] (**Figure 6.8a**). The measured χ being less than 0.5 suggests that PAcMO interacts relatively favorably with the

IL (as compared to LipA with the IL) and that it is the PAcMO-IL interactions that pull the LipA-PAcMO conjugates into solution. Likewise, the size distribution of PAcMO was measured by DLS in [BMIM][PF_6] to confirm that individual polymer molecules were dissolved in the IL and formed a stable solution. PAcMO-36k exhibited only one size distribution in [BMIM][PF_6] with a radius of hydration (R_h) of 6.2 nm, indicating that the polymer was dissolved and did not form aggregates in the IL. Subsequently, the samples were equilibrated for 24 h at room temperature and analyzed again by DLS. As shown in **Figure 6.8b**, there was no change in the measured size distribution and aggregates were not observed, therefore confirming the thermodynamic stability of the polymer-IL solution.

Alternative polymers to PAcMO with more favorable polymer-IL interactions (*i.e.*, lower effective χ) may further enhance LipA activity by reducing the amount of polymer required to solubilize the conjugates and increasing the active site accessibility. However, predicting the strength of polymer-IL interactions, and ultimately the solubility of polymers in ILs, *a priori* remains a challenge. Hildebrand solubility parameters may provide qualitative guidance for polymer selection; however, large discrepancies between the calculated and measured values of solubility parameters for ILs limits the applicability of this approach.[229,233,243–245] Instead, an empirical approach based on directly measuring χ with SLS and verifying molecular dissolution with DLS may be more useful to optimize protein-polymer conjugates for enhanced biocatalysis in ILs. Moreover, characterization of the molecular structure of polymers in ILs using techniques such as small-angle x-ray scattering (SAXS) and small-angle neutron scattering (SANS),[246] to determine, for example, the scaling of the radius of gyration with molecular weight, may be necessary to fully understand of the role of covalently attached polymers in tuning molecular-level interactions between protein conjugates and IL solvents.

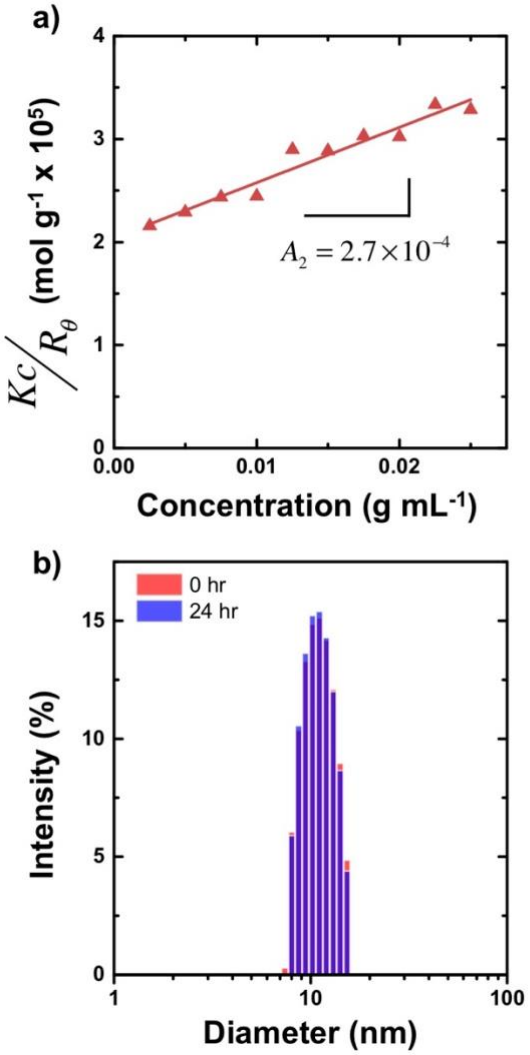

Figure 6.8 a) Debye plot of PAcMO-36k in [BMIM][PF_6] determined by SLS at 25 °C. The second virial coefficient, A_2, was determined as one half of the slope of $\frac{KC}{R_\theta}$ versus concentration. b) Intensity-weighted distributions of particle diameter measured by DLS for PAcMO-36k in [BMIM][PF_6] immediately (0 h) and 24 h after filtration with a 0.1 μm filter. The distribution in particle diameter at 24 h is shown overlaying that at 0 h, which is nearly identical to that at 24 h.

6.5 Conclusions

We have demonstrated that covalent modification of LipA with the IL-soluble polymer PAcMO was a successful and facile strategy to improve enzymatic solubility and activity in the anhydrous hydrophobic IL [BMIM][PF_6]. A clear dependence of conjugate activity on the number of attached PAcMO repeat units was observed in the IL with a maximum 19-fold rate enhancement for the conjugate containing the most PAcMO repeat units. The activity enhancement correlated with conjugate solubility in the IL, though it was not necessary to fully solubilize the conjugates to achieve activity enhancement, as shown by the 8-fold increase in activity of LipA-5k over LipA, which was only partially soluble. The greater numbers of favorable PAcMO-IL interactions in the larger conjugates helped to drive them into solution by tuning the molecular interactions between LipA and [BMIM][PF_6]. Specifically, the favorable PAcMO-IL interactions presumably compensated for the unfavorable interactions between the enzyme and IL, which resulted in the improvement in dissolution. Results of light scattering analysis also showed that PAcMO modification disrupted LipA aggregation, which presumably was more pronounced in the IL where the enzyme has a greater tendency to aggregate. While PAcMO modification led to enhancements in activity, such enhancement in activity on a per polymer unit basis may be improved by identifying polymers with smaller value of χ.

6.6 Acknowledgements

This material is based upon work supported by the National Science Foundation Graduate Research Fellowship under Grant No. DGE 1144083 (G.R.C.). Additionally, this work was partially supported by the research grant CBET 1454379 (to J.L.K) from the National Science Foundation.

Chapter 7: Exploiting the Benefits of Homogeneous and Heterogeneous Biocatalysis: Tuning the Molecular Interaction of Enzymes with Solvents via Polymer Modification

This chapter has been submitted to the Journal of the American Chemical Society

7.1 Abstract

The modification of enzymes with polymers holds tremendous promise as an approach to tune the molecular interactions of enzymes in diverse solvent environments. Here, we demonstrate the use of polymer modification to specifically modulate the thermoresponsive interactions of enzymes with non-native solvents. To demonstrate this approach, the model enzyme lipase (LipA) was modified with random copolymers of poly(acryloylmorpholine-*ran*-N-isopropyl acrylamide) (PAN). Modification of LipA with PAN permitted the reversible phase separation of LipA-PAN from 1-butyl-3-methylimidazolium hexafluorophosphate ([BMIM][PF_6]) in a temperature dependent manner. By varying the compositions of the copolymer, the temperature dependence of this phase separation could be quantitatively controlled between 16-76 °C. Above the temperature of the phase transition, the enzyme was soluble in the ionic liquid (IL), resulting in enhanced transesterification activity (*i.e.*, a 21-fold increase over unmodified LipA), whereas below the temperature of the phase transition, the enzyme could be readily separated and recycled. Remarkably, when recycled via sequential dissolution and precipitation as many as 10 times, the enzyme did not lose any activity. Using this approach, we also showed that the enzyme could be extracted into buffer as well as reversibly shuttled between buffer and the IL in response to changes in temperature. This approach ultimately permits the advantages of homogeneous and heterogeneous biocatalysis in non-native solvents to be exploited and may be readily extended to other enzymes, solvents, and external stimuli. Such an approach may further find application in

other fields, including bioseparations, self-assembly, drug delivery, and the regulation of protein trafficking.

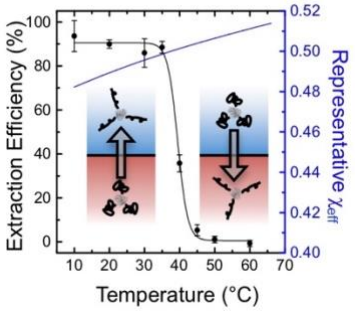

Figure 7.1 Graphical abstract: Covalent attachment of thermoresponsive polymers to an enzyme allows for thermoreversible extraction of the enzyme between an ionic liquid phase and an aqueous phase.

7.2 Introduction

Tuning the miscibility of enzymes in native and non-native solvent environments has important implications for the use of enzymes in industrial chemical transformations.[28,132,219] Traditionally, because the preparation and purification of enzymes can be costly, enzymes are used as heterogeneous catalysts, which facilitates their separation and recycling. The use of enzymes as heterogeneous catalysts frequently involves immobilizing the enzyme on a solid support, such as a particle or resin, which may also stabilize the enzyme against chemical and/or thermal denaturation.[247–249] However, while immobilization may improve enzyme recyclability, the attachment of the enzyme to a solid support can severely impact the activity of the enzyme.[248,250] For example, the activity of the enzyme when immobilized may be significantly affected by mass transfer and diffusional limitations as well as reduced active site accessibility.[251] In light of such limitations, there is considerable interest in developing novel approaches to simultaneously exploit the advantages of heterogeneous and homogeneous biocatalysis.

One approach to leverage the benefits of heterogeneous and homogeneous biocatalysis entails using responsive materials that permit the miscibility of the enzyme to be altered adaptively.

Specifically, in this approach, the thermodynamic interactions between the enzyme and solvent may be varied via modification with materials that have switchable properties. By modifying an enzyme with such materials, the enzyme may ideally be transferred between heterogeneous and homogeneous states in the reaction solvent. Using this approach, the enzyme may, in theory, be miscible in the reaction solvent while catalyzing the reaction, and yet be readily separated via changes in environmental conditions.[162–164] Such an approach is exemplified by the modification of enzymes with poly(N-isopropyl acrylamide), which has been shown to facilitate the reversible precipitation of enzymes from aqueous buffer upon changes in temperature.[165–169] More recently, this approach was demonstrated by Zhu and co-workers by modifying lipase and cytochrome c with a thermoresponsive triblock copolymer.[170,171,252] Modification with the thermoresponsive triblock copolymer permitted the temperature-dependent dissolution and precipitation of lipase and cytochrome c from organic solvents. While these examples highlight the potential utility of this approach, the scope of solvent environments in which these approaches were demonstrated was rather narrow. Furthermore, in these examples, the extent to which the thermodynamics of the molecular-level interactions between the modified enzyme and the solvent may be rationally tuned was not explored.

In previous work, we showed that the thermodynamics of the molecular interactions between lipase and the ionic liquid (IL) 1-butyl-3-methylimidazolium hexafluorophosphate ([BMIM][PF_6]) may be altered by modifying lipase with poly(acryloylmorpholine) (PAcMO).[253] The conjugation of PAcMO to the lipase enhanced the favorability of the thermodynamic interactions of the enzyme with the IL, which resulted in enhanced solubility. Due to the increased solubility in the IL, the transesterification activity of the enzyme increased by as much as 19-fold over that of the insoluble, unmodified enzyme. Notably, the increase in activity and solubility was

directly related to the number of PAcMO polymer repeat units, indicating that the ratio of repeat units-to-enzyme was critical. Although the interactions between lipase and [BMIM][PF_6] were altered, the ultimate success of this approach relies on the ability for such interactions to be varied in a reversible manner, such that the enzyme can be recovered and recycled as in the previous examples.

In this work, we investigated a novel approach to rationally tune the interactions of lipase and [BMIM][PF_6] in a thermoresponsive manner within a desired temperature range. This approach was based on the incorporation of NIPAAm repeat units into a PAcMO copolymer, which imparts an upper critical solution temperature (UCST) type phase behavior to the lipase-polymer conjugates between 16-76 °C. Specifically, lipase A from *Bacillus subtilis* (LipA) was covalently modified with random copolymers of poly(acryloylmorpholine-*ran*-N-isopropyl acrylamide) (PAN). By altering the ratio of AcMO-to-NIPAAm repeat units in PAN, the cloud point of the resulting enzyme-PAN conjugates in the IL could be reliably controlled.

Upon modifying LipA with PAN of varying compositions, the activity of LipA-PAN conjugates in [BMIM][PF_6] after repeated precipitation and re-dissolution was measured. In this way, the ability of the enzyme to be effectively transferred between heterogeneous and homogeneous states was shown, as was the retention of catalytic activity between precipitation/dissolution cycles. The sensitivity of the cloud point of LipA-PAN conjugates in [BMIM][PF_6] to the composition of PAN and solvent environment was also measured spectrophotometrically. Moreover, to further demonstrate the thermoresponsive recyclability of LipA-PAN conjugates in the IL, the temperature-dependent shuttling of the modified enzyme by liquid-liquid extraction between [BMIM][PF_6] and buffer was also demonstrated. Ultimately, this approach provides a framework to realize the orthogonal benefits of homogeneous and

heterogeneous biocatalysis in ILs, which have received considerable attention as solvents for biotransformations, as well as other types of reaction media for enzymes.

7.3 Materials and Methods

Materials

4-cyano-4-(phenylcarbonothioylthio)pentanoic acid N-succinimidyl ester, 2,2'-azobis(2-methylpropionitrile), 4-acryloylmorpholine (97%), 1,4-dioxane (anhydrous, 99.8%), 1-butyl-3-methylimidazolium hexafluorophosphate (97%), molecular sieves (3 Å), and 4-nitrophenyl butyrate (98%) were purchased from Sigma Aldrich. N-isopropylacrylamide (98%) was purchased from Tokyo Chemical Industry UK Ltd. Ethanol (200 proof) was purchased from Decon Labs. Diethyl ether (99%) was purchased from BDH Chemicals. Chloroform (99.8%) was purchased from EMD Millipore. Reagents for the bicinchoninic acid assay and 2,4,6-trinitrobenzene sulfonic acid were purchased from Thermo Fischer Scientific.

LipA Expression and Purification

LipA with a C-terminal polyhistidine tag was expressed in *Escherichia coli* and purified via affinity chromatography as previously reported.[253] Briefly, LipA expression was induced via addition of IPTG to BL21 DE3 cells harboring the gene for LipA in a pET-21B plasmid. Upon expression, the enzyme was purified from crude lysate using a Ni^{2+}-charged Bio-Scale Mini cartridge (Bio-Rad). The concentration of the resulting purified lipA was quantified using the bicinchoninic acid assay.

Reversible Addition Fragmentation Chain Transfer (RAFT) Synthesis of NHS-terminated PAN

N-hydroxysuccinimide ester (NHS)-terminated PAN was synthesized by RAFT as previously reported.[253] Briefly, monomers were purified before use and the copolymer composition was controlled by varying the ratio of AcMO-to-NIPAAm monomer in the reaction solution while keeping the monomer concentration constant at 2 M in 1,4-dioxane. After polymerization, the product was precipitated into diethyl ether and analyzed by GPC using an EcoSEC HLC 8320GPC (Tosoh) and 1H NMR using a Bruker Avance III 300 MHz NMR spectrometer.

Preparation of LipA-PAN Conjugates

LipA-PAN conjugates were prepared via reacting NHS-terminated PAN with LipA in aqueous buffer (50 mM sodium phosphate, pH 7.9, 200 mM sodium chloride, 3 vol% glycerol) for 1 h at room temperature with mixing (100 rpm) on a shaking table incubator. For the preparation of all conjugates, a 20:1 molar ratio of the polymer-to-primary amines in the enzyme was used. Immediately following the reaction, the LipA-PAN conjugates were purified by passing the enzyme over the same Ni^{2+}-charged Bio-Scale Mini cartridge (Bio-Rad) used for purification of the free enzyme, which removed any remaining free polymer unattached to the enzyme. The average number of polymers per enzyme was determined using the TNBSA assay to titrate the number of free amines remaining in the enzyme following modification, and the concentration of enzyme for the conjugates was similarly determined using the bicinchoninic acid assay. Notably, the bicinchoninic acid assay was insensitive to the presence of free PAN in solution. SDS-PAGE analysis was performed under denaturing and reducing conditions on a 4-15% acrylamide gradient gel using Mini-PROTEAN® TGX™ Precast Gels (Bio-Rad) with Coomassie staining.

Measurement of Transesterification Activity of LipA-PAN

The initial rate of transesterification of nitrophenyl butyrate (100 mM) with ethanol (1 M) in [BMIM][PF_6] was assayed spectrophotometrically by monitoring the release of p-nitrophenol at 420 nm in 96-well plates using an Infinite M Plex plate reader (Tecan) at 40 °C. For activity measurements, freeze-dried LipA-PAN, which was lyophilized from sodium phosphate buffer (5 mM, pH 8.0) was used. LipA-PAN conjugates were first dissolved in the IL at a concentration equivalent to 1 mg mL^{-1} enzyme by vigorously mixing the lyophilized powder in the IL solution at 95 °C for 3 min on a heat block. Samples were then diluted to a final concentration equivalent to 0.25 mg mL^{-1} enzyme before measuring activity.

For activity measurements involving the cycling of the conjugate between the dissolved and precipitated state, LipA-PAN was dissolved at a concentration equivalent to 1 mg mL^{-1} of enzyme in [BMIM][PF_6] as above. Stock solutions were cooled to 40 °C and aliquots were diluted to 0.25 mg mL^{-1} enzyme equivalent for measurement of initial activity at 40 °C (referred to as cycle 0). The stock solutions were then cooled to 4 °C for 5 min to precipitate the LipA-PAN conjugate, and subsequently heated back to 40 °C and incubated at the elevated temperature for 5 min to re-dissolve the LipA-PAN conjugate. Upon re-dissolution, the conjugate was diluted to 0.25 mg mL^{-1} enzyme equivalents and assayed at 40 °C as described above. The process of cycling the conjugate between the dissolved and precipitated state was repeated for a maximum of 10 times.

Cloud Point Measurements of LipA-PAN

The cloud points of the LipA-PAN conjugates were determined by measuring the transmittance at 658 nm as a function of temperature using a Litesizer™ 500 (Anton Paar).

Measurements of the cloud point were obtained in aqueous buffer (5 mM sodium phosphate, pH 8.0) and [BMIM][PF_6] with or without ethanol (1 M) at a concentration equivalent to 1 mg mL^{-1} of enzyme. The raw transmittance values over the range of temperatures analyzed were subsequently fit to a sigmoidal function of the form $F(X) = A_1 + \frac{(A_2 - A_1)}{1 + e^{\left(\frac{(X - X_0)}{dX}\right)}}$ where A_1, A_2, X, X_0, and dX represent the minimum transmittance value, maximum transmittance value, mole fraction of NIPAAm, mole fraction of NIPAAm at the inflection point of the sigmoid, and constant related to the width of the sigmoid, respectively. The cloud point of the LipA-PAN conjugate was defined as the temperature at the infection point of the sigmoid, which was referred to as T_0.

Extraction of LipA-PAN from IL to Buffer

The extraction of LipA-PAN from [BMIM][PF_6] to aqueous buffer was measured by initially dissolving an equivalent of 1 mg mL^{-1} enzyme in [BMIM][PF_6]. As indicated above, the dissolution of the conjugate at these conditions was facilitated by vigorously mixing the conjugate solution at 95 °C for 3 min. After mixing and cooling to 40 °C, ethanol (1 M) was added to the conjugate-containing IL solution to mimic the conditions used for activity measurements. The IL solution containing the conjugate and ethanol was subsequently mixed with buffer (5 mM sodium phosphate, pH 8.0) at a 1:10 ratio by volume of [BMIM][PF_6] solution-to-buffer for 1 min. Prior to the extraction, the IL solution containing the conjugate and ethanol and buffer were pre-equilibrated separately at the temperature at which the LipA-PAN was extracted (10-60 °C). The IL-aqueous biphasic mixture was settled by centrifugation at 2000 g for 30 s to achieve rapid phase separation. The extraction efficiency was defined as the relative percent of LipA-PAN recovered in the aqueous phase after mixing. The concentration of the conjugate in the buffer was determined

using the bicinchoninic acid assay, which was unaffected by the presence of trace amounts of [BMIM][PF_6].

Temperature-dependent Shuttling of LipA-PAN between IL and Buffer

To demonstrate the temperature-depending shuttling of LipA between [BMIM][PF_6] and aqueous buffer, LipA-PAN (1 mg mL^{-1} enzyme equivalent) was initially dissolved in [BMIM][PF_6] containing ethanol (1 M). Sodium phosphate (5 mM, pH 8.0) was added to conjugate-containing IL solution at a 1:10 ratio by volume of [BMIM][PF_6] solution-to-buffer. Samples were then incubated at specified temperatures and mixed to extract the LipA-PAN into either the aqueous phase (at low temperatures) or the IL phase (at high temperatures).

7.4Results and Discussion

7.4.1 Conjugate Synthesis and Characterization

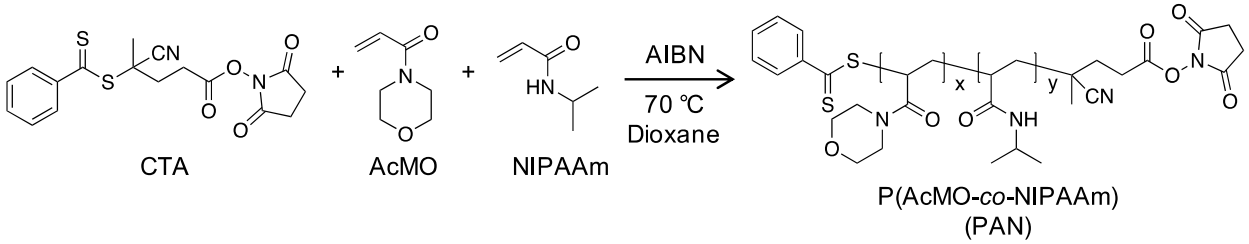

Figure 7.2 Overview of the synthesis of PAN copolymers by RAFT. x and y represent the number of AcMO and NIPAAm repeat units in PAN, respectively.

Thermoreversible solubility in [BMIM][PF_6] was imparted to LipA by initially synthesizing PAN via RAFT polymerization while varying the copolymer composition. Specifically, the copolymer composition was controlled quantitatively by changing the AcMO-to-NIPAAm monomer ratio, while the polymer molecular weight and polydispersity index were kept constant by maintaining the same total monomer-to-chain transfer agent and chain transfer agent-

to-radical initiator ratios (**Figure 7.2**). Under these conditions, the mole fraction of NIPAAm in PAN was varied from 0.58 to 0.88 as determined by ^{1}H NMR, with molecular weights ranging from 44.4 to 55.7 kg mol^{-1} and PDIs less than 1.25 as determined by gel permeation chromatography calibrated with PMMA standards. The apparent molecular weights and PDI values of the polymers are given in **Table A.1** while raw gel permeation chromatography traces are provided in **Figure A.11**.

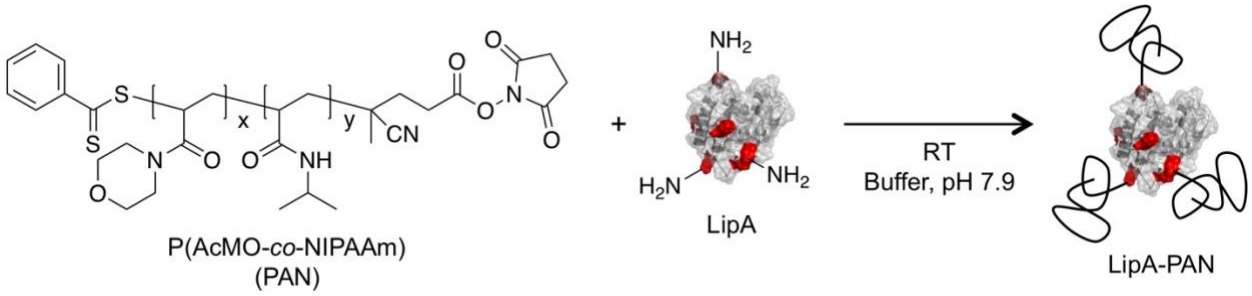

Figure 7.3 Conjugation of NHS-terminated PAN to LipA by NHS-amine coupling. The red spheres represent solvent-accessible lysine residues and the N-terminus that are present on the surface of LipA (PDB code: 5CRI).

Upon synthesis of PAN, LipA-PAN conjugates were prepared by reacting the terminal NHS group on the polymer with free amines on the surface of LipA (**Figure 7.3**). Based on the analysis of the crystal structure of *B. subtilis* LipA, there are a total of 11 primary amines from lysine residues plus the N-terminal amine in the primary sequence of the enzyme. However, of the 12 total amines, 7 are exposed, as defined by greater than 30 % solvent accessible surface area, which was determined using the Swiss-PDB Viewer. For the conjugation reaction, LipA and PAN were reacted at a molar ratio of 20:1 PAN-to-primary amines in LipA, after which residual free PAN was removed via affinity chromatography as described previously.[253] The mole fraction of NIPAAm in the conjugates was limited to between 0.58 and 0.88. Below a mole fraction of NIPAAm of 0.58, the cloud point of LipA-PAN was below 4°C, which was below the limit of detection for cloud point measurements, while above a mole fraction of NIPAAm of 0.88, the

cloud point for LipA-PAN was greater than the boiling point of one of the transesterification substrates for the enzyme (*e.g.*, ethanol).

Quantification of the number of residual unreacted amine groups on LipA-PAN conjugates using the TNBSA assay showed that the average number of attached polymer chains per enzyme ranged from 2.3 to 3.7 (**Table 7.1**). The average number of attached polymer chains and the molecular weight of the polymer was, in turn, used to estimate the total theoretical molecular weight of each conjugate. Notably, although the theoretical total molecular weight of the conjugates varied from 140 to 220 kDa, the majority of the conjugates were between 170 and 190 kDa. Given that the conjugates were of similar total size, differences in solubility and thus activity could be attributed primarily to the composition of the polymer. Additionally, the extent of modification of each conjugate was confirmed by SDS-PAGE analysis, which showed that virtually 100% of the LipA was modified for each conjugate (**Figure 7.4**). Analysis by SDS-PAGE further confirmed that the total theoretical molecular weight of the conjugates was similar as evident by the location of the bands in each lane.

Table 7.1 Characterization of the extent of modification of LipA-PAN conjugates with varying AcMO-to-NIPAAm ratios.

Conjugate Sample Name	Mole Fraction NIPAAm[a]	Number of Polymers per Enzyme[b]	Theoretical Total Molecular Weight (kDa)[c]	Conjugate Sample Name	Mole Fraction NIPAAm[a]	Number of Polymers per Enzyme[b]	Theoretical Total Molecular Weight (kDa)[c]
LipA-PAN58	0.583	3.6 ± 0.2	220 ± 10	LipA-PAN77	0.774	3.0 ± 0.4	180 ± 20
LipA-PAN61	0.614	3.2 ± 0.3	190 ± 20	LipA-PAN78	0.783	2.3 ± 0.1	140 ± 10
LipA-PAN62	0.623	3.3 ± 0.4	200 ± 20	LipA-PAN79	0.790	2.8 ± 0.5	180 ± 30
LipA-PAN63	0.630	2.9 ± 0.1	180 ± 10	LipA-PAN80	0.801	2.5 ± 0.2	150 ± 10
LipA-PAN65	0.651	3.0 ± 0.1	180 ± 10	LipA-PAN82	0.824	3.3 ± 0.4	190 ± 20
LipA-PAN68	0.679	2.9 ± 0.1	180 ± 10	LipA-PAN86	0.860	3.5 ± 0.6	180 ± 30
LipA-PAN72	0.723	2.9 ± 0.4	180 ± 20	LipA-PAN87	0.872	3.7 ± 0.6	180 ± 30
LipA-PAN76	0.759	2.8 ± 0.4	170 ± 20	LipA-PAN88	0.882	3.5 ± 0.2	180 ± 10

[a]Determined by ^{1}H NMR. [b]Measured by TNBSA assay. [c]Calculated using the measured number of polymers per enzyme, molecular weight of unmodified LipA, and polymer molecular weight (**Table A.1**).

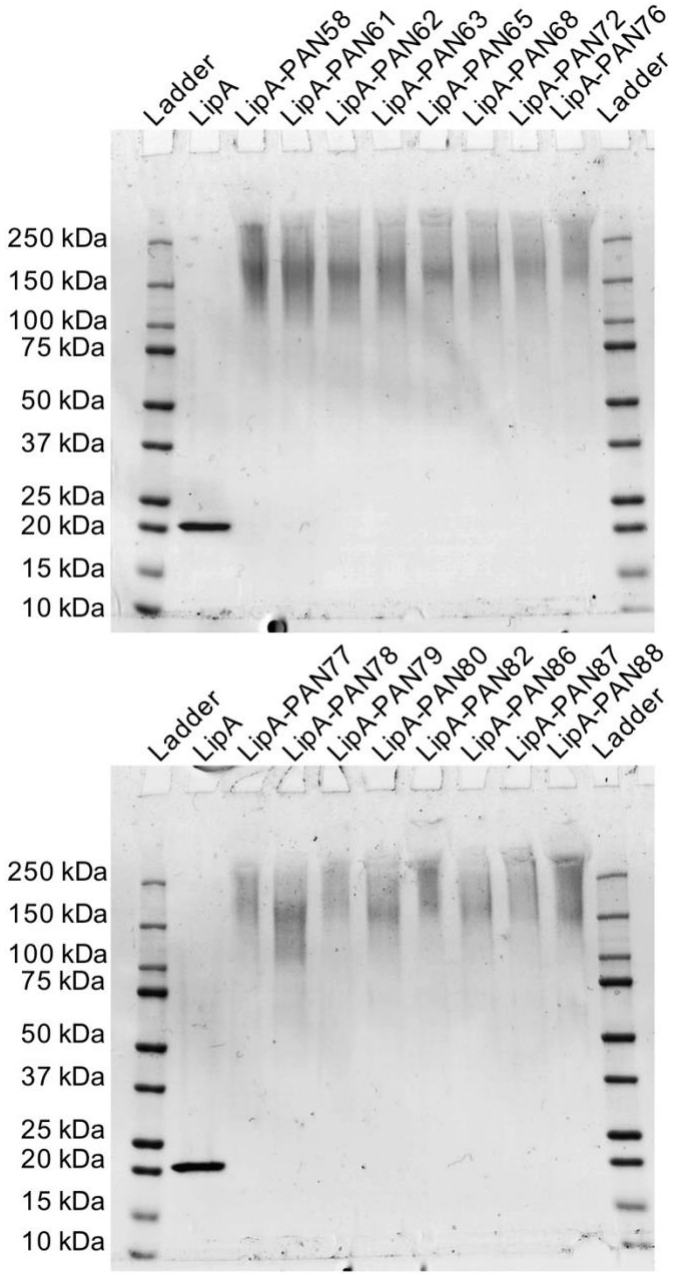

Figure 7.4 SDS-PAGE analysis of unmodified LipA and LipA-PAN conjugates stained with Coomassie under denaturing and reducing conditions with a 4-15% acrylamide gradient.

7.4.2 Conjugate Activity and Recycling in [BMIM][PF6]

As previously reported, the solubility of LipA conjugates containing only AcMO repeat units was the result of a balance between favorable polymer-IL interactions and unfavorable LipA-IL interactions.[253] Here, the thermodynamic favorability of copolymer-IL interactions was made

highly temperature-dependent in the temperature range of interest by the introduction of NIPAAm repeat units. In [BMIM][PF_6], PAN has UCST-type phase behavior such that at temperatures above the cloud point the polymer is soluble and below the cloud point the polymer is insoluble. Because the cloud point is dependent on the composition of the copolymer,[254,255] varying the ratio of AcMO-to-NIPAAm units provides a simple method to tune the cloud point of PAN in [BMIM][PF_6]. As such, one would expect the total thermodynamic favorability of the interactions between LipA-PAN and [BMIM][PF_6] to also be highly temperature dependent. Specifically, we hypothesized that the modification of LipA with PAN would facilitate dissolution of LipA above the cloud point of the conjugate as well as separation of LipA below the cloud point, where the conjugate phase separates from the IL.

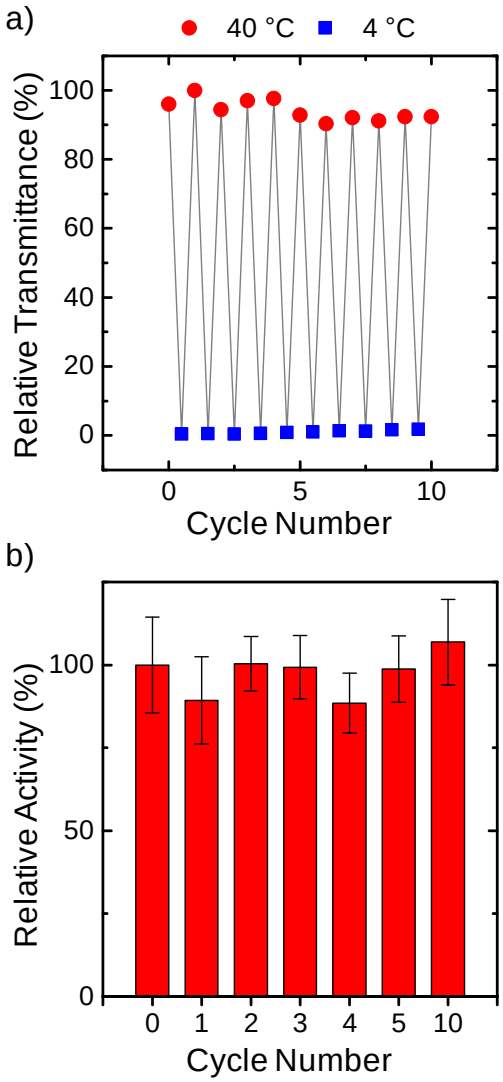

Figure 7.5 Temperature-dependent cycling of the dissolution and precipitation of LipA-PAN61 in anhydrous [BMIM][PF_6]. a) Relative transmittance as a function of precipitation cycling of LipA-PAN61 at a 1 mg mL^{-1} enzyme concentration in the IL containing 1 M ethanol, which was added to mimic conditions of the transesterification reaction used to assay LipA activity. The difference in relative transmittance at 658 nm for LipA-PAN61 was measured by cycling the temperature between 40 °C and 4 °C. The red circles represent the relative transmittance of the LipA-PAN61 conjugate at 40 °C, which is above the cloud point of the conjugate. The blue squares represent the relative transmittance of LipA-PAN61 at 4 °C, where the conjugate is insoluble. Cycle number represents the number of times the temperature was switched from 40 °C to 4 °C and back to 40 °C. Cycle 0 refers to relative transmittance at 40 °C before cooling to 4 °C for the first time (*i.e.*, before the first time the conjugate was precipitated from the IL). b) Relative transesterification activity of LipA-PAN61 in anhydrous [BMIM][PF_6] with 1 M ethanol and 0.1 M 4-nitrophenyl butyrate as a function of cycle number. The transesterification activity for each cycle was normalized to the apparent activity for cycle 0. Error bars represent one standard deviation for $n \geq 4$ distinct experiments.

As hypothesized, LipA-PAN conjugates displayed a UCST-type phase behavior in the IL, which was evident by repeatedly dissolving and precipitating the conjugates in the IL. This was specifically shown for LipA-PAN61, which was exposed to up to 10 cycles of repeated dissolution and precipitation. Notably, LipA-PAN61 was used to demonstrate the thermoresponsive nature of the solubility of the conjugates since it had a convenient cloud point of 20 °C. In the cycling experiments, the conjugate was dissolved by heating the conjugate-containing IL solution to 40 °C after which the solution was cooled to 4 °C at which temperature the conjugate was no longer soluble in the IL. The apparent difference in solubility of LipA-PAN61 at 40 °C and 4 °C was shown by measuring the relative optical transmittance of the conjugate in the IL. When initially heated to 40 °C, the relative transmittance of the conjugate was approximately 100 %, indicating the conjugate was almost completely dissolved (**Figure 7.5a**). However, after cooling, the relative transmittance of the conjugate was virtually 0 %, which was due to precipitation of the conjugate. Importantly, when precipitated and re-dissolved up to 10 cycles, the relative transmittance of the conjugate at 40 °C and 4 °C did not change, suggesting that the process was completely reversible (*i.e.*, all of the precipitate was readily re-dissolved upon increasing temperature). Moreover, the relative transmittance of LipA-PAN61 in [BMIM][PF_6] was measured in the presence of 1 M ethanol, which is a transesterification substrate for LipA.

In addition to showing the thermoresponsive nature of the solubility of LipA-PAN61, the activity of the conjugate in the IL after each precipitation and re-dissolution cycle was assayed. Specifically, after precipitating and re-dissolving, the transesterification activity of the conjugate was assayed to determine the extent to which the activity after cycling was recovered. To measure the transesterification activity of LipA-PAN61 in the IL, enzyme activity was assayed by monitoring the transesterification of 4-nitrophenyl butyrate with ethanol. This reaction is the same

reaction that we used previously to assay the transesterification activity of LipA conjugates containing only AcMO repeat units.[253] For each replicate, activity was measured by removing an aliquot of the IL from a stock solution of the conjugate in the IL after each cooling and heating cycle. Remarkably, the conjugate retained virtually 100% of its initial activity prior to the first time the conjugate was precipitated form the IL, which was denoted as cycle 0 (**Figure 7.5b**). Additionally, the activity of residual soluble conjugate in the IL after precipitation at 4 °C was only 7 % of the initial activity prior to precipitation, confirming very little of the enzyme remained soluble after cooling. In this case, after cooling, the conjugate that precipitated was removed via centrifugation and the activity of the remaining soluble conjugate was assayed at 40 °C (the same temperature the conjugates were assayed at after each precipitation and re-dissolution cycle). It was also noteworthy that the transesterification activity of LipA-PAN61 at 40 °C was 21 ± 2 times greater than unmodified LipA in anhydrous [BMIM][PF_6]. This enhancement in activity as a result of dissolution of the enzyme is nearly identical to that reported previously for conjugate containing only AcMO.[253]

7.4.3 Effect of Copolymer Composition on Conjugate Cloud Point

To determine the extent to which the cloud point of LipA-PAN could be tuned, the cloud point of LipA-PAN was measured as a function of the composition of PAN in the conjugate. The range of cloud points for the conjugates in **Table 7.1** was specifically determined by measuring relative optical transmittance at 658 nm as a function of temperature for each conjugate in the IL. The raw data of the relative transmittance as a function of temperature was subsequently fit to a sigmoidal function to yield the cloud point (*i.e.*, the inflection point in the curve of the raw data). Cloud point data is shown for three representative samples in **Figure 7.6a**, while data for all

samples is available in **Figure A.12**. Analysis of the cloud points for the conjugates showed that, for the range of mole fractions of NIPAAm used in preparing PAN, the cloud point in [BMIM][PF_6] varied between 16 °C to 76 °C (**Figure 7.6b**). Interestingly, the cloud point was linearly dependent on the mole fraction of NIPAAm in the LipA-PAN conjugates over the range of mole fractions used here. Given the linearity of the trend within this range of NIPAAm compositions, the cloud point was predictable and the composition of PAN could be rationally altered to yield a desired cloud point. It should be noted, however, that the dependence of cloud point on NIPAAm mole fraction may not be linear outside of this range and such correlations should not be extrapolated.[256]

Interestingly, the relationship between cloud point and the fraction of NIPAAm in the PAN of the conjugates was impacted by the presence of ethanol (blue triangles in **Figure 7.6b**). Specifically, in the presence of the ethanol (1 M), the cloud point increased substantially (by 10~25 °C) and the slope of this relationship was reduced, indicating the cloud point was relatively less sensitive to polymer composition. Having observed UCST-type behavior of the LipA-PAN conjugates in [BMIM][PF_6], it is interesting to consider the mechanism that underlies this thermodynamic behavior and set of observations. Asai and co-workers have previously observed the UCST-like behavior of poly(NIPAAm) and changes in polymer chain conformation in deuterated 1-ethyl-3-methylimidazolium bis(trifluoromethanesulfonyl)amide that ultimately arise due to the thermodynamic and molecular-level interactions between the polymer and the solvent environment.[257] Here, the system is more complex as a result of the diverse molecular-level interactions between the multiple copolymer repeat units and LipA with the IL solvent (as well as with each other). Additives, such as ethanol or other substrates, change the effective solvent quality and further complicate this picture by introducing additional interactions in the multicomponent

system. For the LipA-PAN conjugates in [BMIM][PF_6], the AcMO interactions with the IL are significantly more favorable than the NIPAAm interactions with the IL and drive the conjugate solubility. The inclusion of ethanol differentially modulates the strength of these interactions, with the AcMO-solvent and NIPAAm-solvent interactions becoming relatively less and more favorable, respectively. The AcMO is still more favorable than NIPAAm in the IL with ethanol, however, which means that a lower concentration of NIPAAm is required in the PAN to achieve the same conjugate cloud point as in a pure IL environment (*i.e.*, without ethanol).

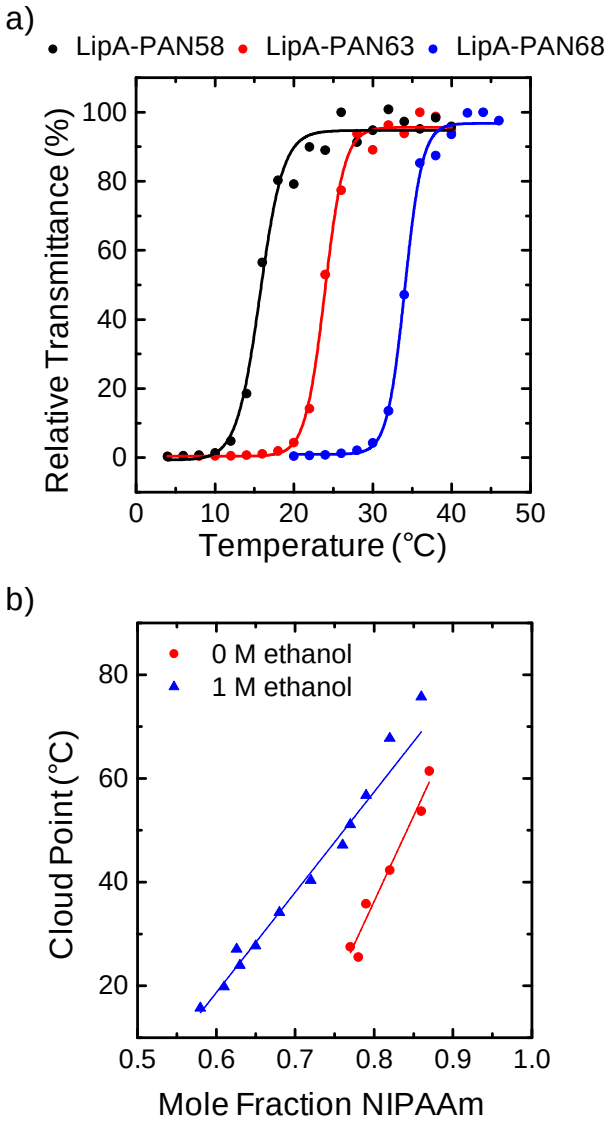

Figure 7.6 Effect of the composition of PAN on the cloud point of LipA-PAN conjugates in anhydrous [BMIM][PF_6]. a) Representative cloud point curves for three representative LipA-PAN conjugates (LipA-PAN58, LipA-PAN63, LipA-PAN68) in [BMIM][PF_6] containing 1 M ethanol. The solid curves represent the sigmoidal fit of the raw curves of relative transmittance versus temperature from which the cloud point was determined. b) Dependence of LipA-PAN cloud point on mole fraction of NIPAAm in PAN. Results are shown for both [BMIM][PF_6] with (blue triangles) and without (red circles) 1 M ethanol. The solid lines are meant to guide the eye and demonstrate the linearity of cloud point with mole fraction of NIPAAm.

7.4.4 Thermoreversible Shuttling Between [BMIM][PF_6] and Aqueous Buffer

In addition to precipitation from [BMIM][PF_6], which is immiscible with water, the separation of LipA-PAN via liquid-liquid extraction into buffer was also investigated.

Interestingly, over the temperature range investigated here, PAN exhibited an UCST-type phase behavior in [BMIM][PF_6], but in contrast had a lower critical solution temperature (LCST) type phase behavior in aqueous solutions due to the presence of the NIPAAm units. As presented in the cloud point data of **Figure 7.7a**, the LCST-type phase behavior meant that the LipA-PAN61 conjugates were soluble in buffer at temperatures below the cloud point of 39 °C, but phase separated at temperatures above the cloud point, which was reflected by a decrease in optical transmission. Given the LCST-type behavior in buffer and UCST-type behavior in IL, and more generally that the overall thermodynamic favorability of each solvent for LipA-PAN was highly temperature sensitive, it was possible to selectively exchange LipA-PAN between solvent environments in a thermoreversible manner.

To demonstrate the feasibility of this approach, LipA-PAN61 was dissolved in [BMIM][PF_6] containing 1 M ethanol to mimic the conditions of the transesterification reaction. Aqueous buffer was then added at a 10:1 volume ratio of buffer-to-IL, and the efficiency of extraction of the conjugate from the IL to buffer was quantified. The extraction efficiency, defined as the percentage of LipA-PAN61 recovered in the aqueous phase after equilibration and separation, showed a strong temperature dependence as shown in **Figure 7.7b**. Notably, the extraction efficiency was greater than 90% at low system temperatures, but dropped precipitously at ~40 °C and further decreased to near 0% by 45 °C.

The observed exchange behavior may be rationalized by considering the temperature dependence of the thermodynamic preferences for the LipA-PAN conjugates in each solvent environment. Under the initial conditions, LipA-PAN61 had a cloud point of 20 °C in the IL phase (*i.e.*, 1 M ethanol in [BMIM][PF_6]) whereas the conjugate had a cloud point of 39 °C in the buffer. At low temperatures (*i.e.*, $T < 20$ °C, below the cloud points of the conjugate in buffer and the IL),

the conjugate became insoluble in the IL and partitioned completely into the aqueous phase where it was soluble. At high temperatures (*i.e.*, $T > 39$ °C, above the cloud points of the conjugate in buffer and the IL), the conjugate was insoluble in the aqueous phase and remained in the IL phase in which it was soluble. These disparate responses explain the transition between high and low extraction efficiencies into buffer that are reported as a function of temperature in **Figure 7.7b**. However, at intermediate temperatures (*i.e.*, $20 < T < 39$ °C, above the UCST–type cloud point in the IL, but below the LCST-type cloud point of the conjugate in buffer) the conjugate should be soluble in both phases and partial segregation of the LipA-PAN conjugates may be anticipated. Notably, in this temperature range, a high extraction efficiency into buffer was also observed, which suggested that the interactions between LipA-PAN and water were significantly more favored thermodynamically than the interactions between LipA-PAN and [BMIM][PF_6]. Under such conditions, the temperature-dependence of the extraction efficiency was thus primarily dictated by the LCST-type behavior of the conjugates in buffer, and the inflection temperature in the extraction efficiency curve corresponded to that of the aqueous cloud point.

It should be noted that ethanol, which was also initially present in the IL phase at a concentration of 1 M, may partition between the aqueous and IL phases during mixing. Transfer of the ethanol out of the IL phase will lower the UCST-type cloud point of the conjugate in IL but may also impact the LCST-type cloud point in the aqueous phase. To examine this effect, the aqueous cloud point was measured in buffer containing 0.1 M ethanol, which corresponds to the maximum possible concentration of ethanol in the aqueous buffer after extraction with a 10:1 volume ratio of aqueous buffer-to-IL (**Figure 7.7a**). The presence of 0.1 M ethanol had a negligible effect (< 1 °C) on the aqueous cloud point, thereby indicating that the thermoresponsive extraction behavior was insensitive to the presence (or concentration) of the ethanol substrate in the system.

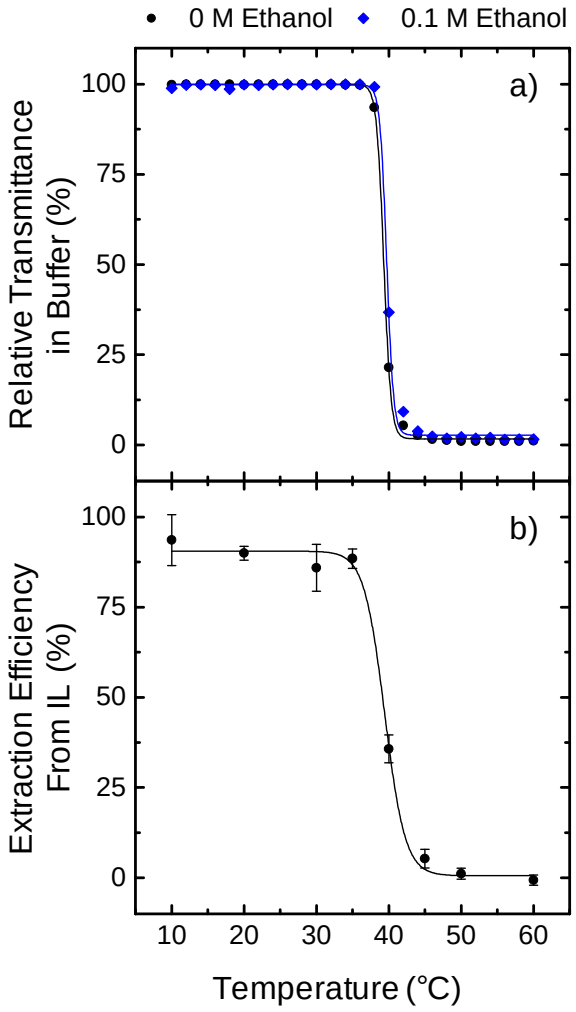

Figure 7.7 a) Relative transmittance of LipA-PAN61 in aqueous buffer (5 mM sodium phosphate, pH 8) without ethanol (black circles) and 0.1 M ethanol (blue diamonds) as a function of temperature. b) Extraction efficiency of LipA-PAN61 from [BMIM][PF_6] containing 1 M ethanol into aqueous buffer as a function of temperature. Extraction efficiency is defined as the percentage of total enzyme recovered in the aqueous phase after extraction. Solid lines represent sigmoidal fits of the raw extraction efficiency and relative transmittance data. Error bars represent one standard deviation of $n \geq 3$ distinct trials.

While investigating the recovery of LipA-PAN61 from [BMIM][PF_6] via extraction into buffer, we further explored if the extraction of the conjugate was reversible. Specifically, of interest was determining if LipA-PAN61 could be shuttled back and forth between the IL and aqueous phases via repeated heating and cooling cycles. The thermoreversible shuttling of the

conjugate between phases was demonstrated as depicted in **Figure 7.8**, which shows images of the conjugate in the immiscible IL/buffer system. Initially, LipA-PAN61 was dissolved at an enzyme concentration of 1 mg mL^{-1} in the IL phase by equilibrating the mixture of the IL and buffer at 45 °C (**Figure 7.8a**). The IL/buffer mixture was subsequently cooled to 4 °C, at which temperature the conjugate became insoluble in the IL phase and caused the IL phase to appear cloudy (**Figure 7.8b**). Upon mixing to extract the precipitated LipA-PAN61 into the aqueous phase, both phases once again became transparent (**Figure 7.8c**). Finally, when the biphasic system was subsequently heated to 45 °C, the conjugate became insoluble in the aqueous phase (**Figure 7.8d**) and could be selectively extracted back into the IL phase, thereby completing the thermoresponsive shuttling cycle.

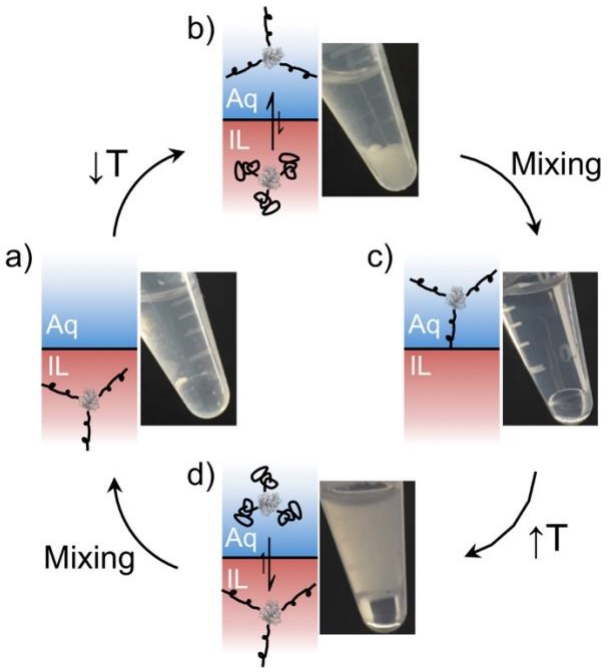

Figure 7.8 Thermoreversible shuttling cycle of LipA-PAN conjugate between [BMIM][PF_6] and aqueous solutions. In the images of the immiscible IL/buffer system, the IL and aqueous phases correspond to the bottom and top layers, respectively. a) LipA-PAN61 was initially dissolved in the [BMIM][PF_6] phase at 45 °C. b) Upon cooling to 4 °C, LipA-PAN61 became insoluble and caused the IL phase to become opaque. c) After vigorous mixing at 4 °C, both phases became transparent as a result of the extraction of the conjugate into the aqueous phase where the conjugate was soluble. d) Upon heating to 45 °C, the LipA-PAN61 became insoluble in the aqueous phase, thus causing the aqueous phase to turn opaque. After vigorous mixing at 45 °C, both phases became transparent, as seen in a), which was the result of the conjugate being extracted back into the IL phase where the conjugate was soluble at the mixing temperature.

Having demonstrated this approach for recycling LipA from [BMIM][PF_6], it is naturally interesting to consider how this approach may be extended to other enzyme/solvent systems. For example, this approach may, in theory, be readily extended to other systems by considering the UCST and LCST behavior of different polymers in other environments. As shown here, the UCST and LCST behavior of the polymer-enzyme conjugate in different solvents may be rationally tuned by systematically varying the polymer composition. Given this, one could envision using such an approach to recycle enzymes from other ILs (*e.g.*, [BMIM][BF_4], [BMIM][NTf_2], [BMPy][NTf_2]) as well as a broad range of organic solvents, such as hexane and acetonitrile, which are commonly used for non-aqueous biocatalysis.[143,144,148,258,259] In addition to facilitating recycling, this approach

(*i.e.*, thermoresponsive shuttling) could also be used as a switch to effectively turn enzymes "on" or "off" in a particular phase. Beyond biocatalysis, proteins that are modified with copolymers exhibiting UCST and LCST behaviors in different environments may also have utility as affinity surfactants for transferring (*e.g.*, extracting) protein cargo between immiscible solvents.[260] Specifically, in this case, the modified protein may be used to transfer a second protein (*i.e.*, a protein cargo) that binds to the modified protein without modifying the cargo itself. Furthermore, such an approach may also be used to control the reversible assembly of proteins into hierarchical three-dimensional nanostructures by modulating the solubility of the protein in a given solvent in response to changes in temperature.[236,261,262] Lastly, by modifying enzymes or proteins with copolymers that are responsive to other stimuli (*e.g.*, light,[155–157] pH,[158,159] or ionic strength[160]), the interactions of proteins with immiscible solvents may be mediated in response to different triggers.

7.5 Conclusions

In conclusion, our findings show the feasibility of modulating the thermoresponsive interactions of enzymes with non-native solvents via polymer modification. Specifically, we demonstrated that covalently modifying LipA with a PAN copolymer having well-defined ratios of AcMO-to-NIPAAm repeat units permitted solubilization of the LipA-PAN conjugates in [BMIM][PF_6] at desired temperatures. Moreover, by rationally controlling the temperature of phase separation, the enzyme-polymer conjugates could be reversibly separated from the IL in response to changes in temperature in a predictable manner, and effectively recycled without any loss of activity. Although in this work the composition of the polymer was tuned to facilitate enzyme recycling between 16-76 °C, in principle, the thermodynamic behavior and cloud point of the conjugates could be readily shifted by tuning the temperature-dependent molecular interactions

between the polymer and the solvent. For example, adjusting the composition of PAN or using alternative polymer constituents that have different interactions with the solvent would, in theory, change how the conjugate interacts with the solvent as a function of temperature. Additionally, we demonstrated that LipA-PAN could be shuttled between [BMIM][PF_6], which is water immiscible, and buffer using changes in temperature as a trigger. The ability to shuttle the conjugate between solvents is the result of the conjugate having a LCST-type phase behavior in buffer in addition to an UCST-type phase behavior in the IL. As an approach to tune the molecular interactions of enzymes and/or proteins with their solvent environment, this approach is general and has many applications beyond recycling enzymes for biocatalysis, including bioseparations, bionanotechnology, and potentially even protein trafficking in biological environments and drug delivery.[263]

7.6 Acknowledgements

We acknowledge financial support for this work from the National Science Foundation through the CBET division (award number 1454379). G.R.C. was also supported by a research fellowship through the Department of Education GAANN program (P200A150211). Additionally, this material is based upon work supported by the National Science Foundation Graduate Research Fellowship under Grant No. DGE 1144083 (to G.R.C.).

Bibliography

(1) Gody, G.; Zetterlund, P. B.; Perrier, S.; Harrisson, S. The Limits of Precision Monomer Placement in Chain Growth Polymerization. *Nat. Commun.* **2016**, *7*, 10514.

(2) Gody, G.; Maschmeyer, T.; Zetterlund, P. B.; Perrier, S. Rapid and Quantitative One-Pot Synthesis of Sequence-Controlled Polymers by Radical Polymerization. *Nat. Commun.* **2013**, *4*, 2505.

(3) Fleury, G.; Bates, F. S. Structure and Properties of Hexa- And Undecablock Terpolymers with Hierarchical Molecular Architectures. *Macromolecules* **2009**, *42*, 3598–3610.

(4) Nagata, Y.; Masuda, J.; Noro, A.; Cho, D.; Takano, A.; Matsushita, Y. Preparation and Characterization of a Styrene-Isoprene Undecablock Copolymer and Its Hierarchical Microdomain Structure in Bulk. *Macromolecules* **2005**, *38*, 10220–10225.

(5) Soeriyadi, A. H.; Boyer, C.; Nyström, F.; Zetterlund, P. B.; Whittaker, M. R. High-Order Multiblock Copolymers via Iterative Cu(0)-Mediated Radical Polymerizations (SET-LRP): Toward Biological Precision. *J. Am. Chem. Soc.* **2011**, *133*, 11128–11131.

(6) Son, J. G.; Chang, J.-B.; Berggren, K. K.; Ross, C. A. Assembly of Sub-10-Nm Block Copolymer Patterns with Mixed Morphology and Period Using Electron Irradiation and Solvent Annealing. *Nano Lett.* **2011**, *11*, 5079–5084.

(7) Bosworth, J. K.; Black, C. T.; Ober, C. K. Selective Area Control of Self-Assembled Pattern Architecture Using a Lithographically Patternable Block Copolymer. *ACS Nano* **2009**, *3*, 1761–1766.

(8) He, C.; Stoykovich, M. P. Photopatterning of Cross-Linkable Epoxide-Functionalized Block Copolymers and Dual-Tone Nanostructure Development for Fabrication across the Nano- and Microscales. *Small* **2015**, *11*, 2407–2416.

(9) Kim, S. O.; Solak, H. H.; Stoykovich, M. P.; Ferrier, N. J.; De Pablo, J. J.; Nealey, P. F. Epitaxial Self-Assembly of Block Copolymers on Lithographically Defined Nanopatterned Substrates. *Nature* **2003**, *424*, 411–414.

(10) Bita, I.; Yang, J. K. W.; Jung, Y. S.; Ross, C. A.; Thomas, E. L.; Berggren, K. K. Graphoepitaxy of Self-Assembled Block Copolymers on Two-Dimensional Periodic Patterned Templates. *Science* **2008**, *321*, 939–943.

(11) Park, S.-M.; Liang, X.; Harteneck, B. D.; Pick, T. E.; Hiroshiba, N.; Wu, Y.; Helms, B. A.; Olynick, D. L. Sub-10 Nm Nanofabrication via Nanoimprint Directed Self-Assembly

of Block Copolymers. *ACS Nano* **2011**, *5*, 8523–8531.

(12) Onses, M. S.; Song, C.; Williamson, L.; Sutanto, E.; Ferreira, P. M.; Alleyne, A. G.; Nealey, P. F.; Ahn, H.; Rogers, J. A. Hierarchical Patterns of Three-Dimensional Block-Copolymer Films Formed by Electrohydrodynamic Jet Printing and Self-Assembly. *Nat. Nanotechnol.* **2013**, *8*, 667–675.

(13) Tran, H.; Ronaldson, K.; Bailey, N. A.; Lynd, N. A.; Killops, K. L.; Vunjak-Novakovic, G.; Campos, L. M. Hierarchically Ordered Nanopatterns for Spatial Control of Biomolecules. *ACS Nano* **2014**, *8*, 11846–11853.

(14) Tran, H.; Killops, K. L.; Campos, L. M. Advancements and Challenges of Patterning Biomolecules with Sub-50 Nm Features. *Soft Matter* **2013**, *9*, 6578–6586.

(15) Van Der Lee, R.; Buljan, M.; Lang, B.; Weatheritt, R. J.; Daughdrill, G. W.; Dunker, A. K.; Fuxreiter, M.; Gough, J.; Gsponer, J.; Jones, D. T.; *et al.* Classification of Intrinsically Disordered Regions and Proteins. *Chem. Rev.* **2014**, *114*, 6589–6631.

(16) Raushel, F. M.; Thoden, J. B.; Holden, H. M. Enzymes with Molecular Tunnels. *Acc. Chem. Res.* **2003**, *36*, 539–548.

(17) Jørgensen, K.; Rasmussen, A. V.; Morant, M.; Nielsen, A. H.; Bjarnholt, N.; Zagrobelny, M.; Bak, S.; Møller, B. L. Metabolon Formation and Metabolic Channeling in the Biosynthesis of Plant Natural Products. *Curr. Opin. Plant Biol.* **2005**, *8*, 280–291.

(18) Bulutoglu, B.; Garcia, K. E.; Wu, F.; Minteer, S. D.; Banta, S. Direct Evidence for Metabolon Formation and Substrate Channeling in Recombinant TCA Cycle Enzymes. *ACS Chem. Biol.* **2016**, *11*, 2847–2853.

(19) Küchler, A.; Yoshimoto, M.; Luginbühl, S.; Mavelli, F.; Walde, P. Enzymatic Reactions in Confined Environments. *Nat. Nanotechnol.* **2016**, *11*, 409–420.

(20) Liu, F.; Banta, S.; Chen, W. Functional Assembly of a Multi-Enzyme Methanol Oxidation Cascade on a Surface-Displayed Trifunctional Scaffold for Enhanced NADH Production. *Chem. Commun.* **2013**, *49*, 3766–3768.

(21) Chen, R.; Chen, Q.; Kim, H.; Siu, K.; Sun, Q.; Tsai, S.; Chen, W. Biomolecular Scaffolds for Enhanced Signaling and Catalytic Efficiency. *Curr. Opin. Biotechnol.* **2014**, *28*, 59–68.

(22) Ulyanova, Y.; Arugula, M. A.; Rasmussen, M.; Pinchon, E.; Lindstrom, U.; Singhal, S.; Minteer, S. D. Bioelectrocatalytic Oxidation of Alkanes in a JP-8 Enzymatic Biofuel Cell.

ACS Catal. **2014**, *4*, 4289–4294.

(23) Moehlenbrock, M. J.; Toby, T. K.; Waheed, A.; Minteer, S. D. Metabolon Catalyzed Pyruvate/Air Biofuel Cell. *J. Am. Chem. Soc.* **2010**, *132*, 6288–6289.

(24) Eguílaz, M.; Villalonga, R.; Yáñez-Sedeño, P.; Pingarrón, J. M. Designing Electrochemical Interfaces with Functionalized Magnetic Nanoparticles and Wrapped Carbon Nanotubes as Platforms for the Construction of High-Performance Bienzyme Biosensors. *Anal. Chem.* **2011**, *83*, 7807–7814.

(25) Lee, H.; DeLoache, W. C.; Dueber, J. E. Spatial Organization of Enzymes for Metabolic Engineering. *Metab. Eng.* **2012**, *14*, 242–251.

(26) Zhang, Y.; Tsitkov, S.; Hess, H. Proximity Does Not Contribute to Activity Enhancement in the Glucose Oxidase-Horseradish Peroxidase Cascade. *Nat. Commun.* **2016**, *7*, 13982.

(27) Fu, J.; Liu, M.; Liu, Y.; Woodbury, N. W.; Yan, H. Interenzyme Substrate Diffusion for an Enzyme Cascade Organized on Spatially Addressable DNA Nanostructures. *J. Am. Chem. Soc.* **2012**, *134*, 5516–5519.

(28) Carrea, G.; Riva, S. Properties and Synthetic Applications of Enzymes in Organic Solvents. *Angew. Chem. Int. Ed. Engl.* **2000**, *39*, 2226–2254.

(29) Abe, Y.; Yoshiyama, K.; Yagi, Y.; Hayase, S.; Kawatsura, M.; Itoh, T. A Rational Design of Phosphonium Salt Type Ionic Liquids for Ionic Liquid Coated-Lipase Catalyzed Reaction. *Green Chem.* **2010**, *12*, 1976–1980.

(30) Itoh, T. Ionic Liquids as Tool to Improve Enzymatic Organic Synthesis. *Chem. Rev.* **2017**, *117*, 10567–10607.

(31) Kaar, J. L.; Jesionowski, A. M.; Berberich, J. A.; Moulton, R.; Russell, A. J. Impact of Ionic Liquid Physical Properties on Lipase Activity and Stability. *J. Am. Chem. Soc.* **2003**, *125*, 4125–4131.

(32) Roberts, N. J.; Seago, A.; Carey, J. S.; Freer, R.; Lye, G. J. Lipase Catalysed Resolution of the Lotrafiban Intermediate Acid Methyl Ester in Ionic Liquids: Comparison to the Industrial t-Butanol Process. *Green Chem.* **2004**, *6*, 475–482.

(33) Persson, M.; Bornscheuer, U. T. Increased Stability of an Esterase from Bacillus Stearothermophilus in Ionic Liquids as Compared to Organic Solvents. *J. Mol. Catal. B Enzym.* **2003**, *22*, 21–27.

(34) Ueki, T.; Watanabe, M. Macromolecules in Ionic Liquids: Progress, Challenges, and Opportunities. *Macromolecules* **2008**, *41*, 3739–3749.

(35) Lodge, T. P. Materials Science. A Unique Platform for Materials Design. *Science* **2008**, *321*, 50–51.

(36) Hadjichristidis, N.; Pitsikalis, M.; Pispas, S.; Iatrou, H. Polymers with Complex Architecture by Living Anionic Polymerization. *Chemical Reviews*, 2001, *101*, 3747–3792.

(37) Hadjichristidis, N.; Pispas, S.; Floudas, G. *Block Copolymers : Synthetic Strategies, Physical Properties, and Applications*; Wiley-Interscience, 2003.

(38) Hadjichristidis, N.; Iatrou, H.; Pitsikalis, M.; Mays, J. Macromolecular Architectures by Living and Controlled/Living Polymerizations. *Progress in Polymer Science (Oxford)*, 2006, *31*, 1068–1132.

(39) Bates, F. S.; Fredrickson, G. H. Block Copolymer Thermodynamics: Theory and Experiment. *Annu. Rev. Phys. Chem.* **1990**, *41*, 525–557.

(40) Bates, F. S.; Fredrickson, G. H. Block Copolymers—Designer Soft Materials. *Phys. Today* **1999**, *52*, 32–38.

(41) Abetz, V.; Simon, P. F. W. Phase Behaviour and Morphologies of Block Copolymers. *Adv. Polym. Sci.* **2005**, *189*, 125–212.

(42) Matsen, M. W.; Bates, F. S. Unifying Weak- and Strong-Segregation Block Copolymer Theories. *Macromolecules* **1996**, *29*, 1091–1098.

(43) Hashimoto, T.; Nagatoshi, K.; Todo, A.; Hasegawa, H.; Kawai, H. Domain-Boundary Structure of Styrene-Isoprene Block Copolymer Films Cast from Toluene Solutions. *Macromolecules* **1974**, *7*, 364–373.

(44) Hashimoto, T.; Todo, A.; Itoi, H.; Kawai, H. Domain-Boundary Structure of Styrene-Isoprene Block Copolymer Films Cast from Solutions. 2. Quantitative Estimation of the Interfacial Thickness of Lamellar Microphase Systems. *Macromolecules* **1977**, *10*, 377–384.

(45) Todo, A.; Hiroyukiuno; Miyoshi, K.; Hashimoto, T.; Hiromichikawai. Domain-Boundary Structure of Styrene-Isoprene Block Copolymer Films Cast from Solutions. III. Preliminary Results on Spherical Microdomains. *Polym. Eng. Sci.* **1977**, *17*, 587–597.

(46) Hashimoto, T.; Shibayama, M.; Kawai, H. Domain-Boundary Structure of Styrene-Isoprene Block Copolymer Films Cast from Solution. 4. Molecular-Weight Dependence of Lamellar Microdomains. *Macromolecules* **1980**, *13*, 1237–1247.

(47) Hashimoto, T.; Fujimura, M.; Kawai, H. Domain-Boundary Structure of Styrene-Isoprene Block Copolymer Films Cast from Solutions. 5. Molecular-Weight Dependence of Spherical Microdomains. *Macromolecules* **1980**, *13*, 1660–1669.

(48) Hashimoto, T. Generalized View of Molecular Weight Dependence of Microdomain Size of Block Polymers. Appraisal of Hadziioannou-Skoulios' Data on Binary Mixtures of Block Polymers. *Macromolecules* **1982**, *15*, 1548–1553.

(49) Hashimoto, T.; Yamasaki, K.; Koizumi, S.; Hasegawa, H. Ordered Structure in Blends of Block Copolymers. 1. Miscibility Criterion for Lamellar Block Copolymers. *Macromolecules* **1993**, *26*, 2895–2904.

(50) Hashimoto, T.; Koizumi, S.; Hasegawa, H. Ordered Structure in Blends of Block Copolymers.2.Self-Assembly for Immiscible Lamella-Forming Copolymers. *Macromolecules* **1994**, *27*, 1562–1570.

(51) Koizumi, S.; Hasegawa, H.; Hashimoto, T. Ordered Structure in Blends of Block Copolymers. 3. Self-Assembly in Blends of Sphere- or Cylinder-Forming Copolymers. *Macromolecules* **1994**, *27*, 4371–4381.

(52) Yamaguchi, D.; Bodycomb, J.; Koizumi, S.; Hashimoto, T. Ordered Structure in Blends of Block Copolymers. 4. Location of the Short Diblock. *Macromolecules* **1999**, *32*, 5884–5894.

(53) Yamaguchi, D.; Shiratake, S.; Hashimoto, T. Ordered Structure in Blends of Block Copolymers. 5. Blends of Lamella-Forming Block Copolymers Showing Both Microphase Separation Involving Unique Morphological Transitions and Macrophase Separation. *Macromolecules* **2000**, *33*, 8258–8268.

(54) Mayes, A. M.; Russell, T. P.; Deline, V. R.; Satija, S. K.; Majkrzak, C. F. Block Copolymer Mixtures As Revealed By Neutron Reflectivity. *Macromolecules* **1994**, *27*, 7447–7453.

(55) Mayes, A. M.; Russell, T. P.; Satija, S. K.; Majkrzak, C. F. Homopolymer Distributions in Ordered Block Copolymers. *Macromolecules* **1992**, *25*, 6523–6531.

(56) Torikai, N.; Takabayashi, N.; Noda, I.; Koizumi, S.; Morii, Y.; Matsushita, Y. Lamellar Domain Spacings of Diblock Copolymer/Homopolymer Blends and Conformations of Block Chains in Their Microdomains. *Macromolecules* **1997**, *30*, 5698–5703.

(57) Liu, G.; Stoykovich, M. P.; Ji, S.; Stuen, K. O.; Craig, G. S. W.; Nealey, P. F. Phase Behavior and Dimensional Scaling of Symmetric Block Copolymer−Homopolymer Ternary Blends in Thin Films. *Macromolecules* **2009**, *42*, 3063–3072.

(58) Winey, K. I.; Thomas, E. L.; Fetters, L. J. Isothermal Morphology Diagrams for Binary Blends of Diblock Copolymer and Homopolymer. *Macromolecules* **1992**, *25*, 2645–2650.

(59) Kim, J. K.; Yang, S. Y.; Lee, Y.; Kim, Y. Functional Nanomaterials Based on Block Copolymer Self-Assembly. *Prog. Polym. Sci.* **2010**, *35*, 1325–1349.

(60) Kim, H. C.; Park, S. M.; Hinsberg, W. D.; Division, I. R. Block Copolymer Based Nanostructures: Materials, Processes, and Applications to Electronics. *Chem. Rev.* **2010**, *110*, 146–177.

(61) Jo, P. S.; Sung, J.; Park, C.; Kim, E.; Ryu, D. Y.; Pyo, S.; Kim, H. C.; Hong, J. M. Controlled Topology of Block Copolymer Gate Insulators by Selective Etching of Cylindrical Microdomains in Pentacene Organic Thin Film Transistors. *Adv. Funct. Mater.* **2008**, *18*, 1202–1211.

(62) Nie, Z.; Kumacheva, E. Patterning Surfaces with Functional Polymers. *Nat. Mater.* **2008**, *7*, 277–290.

(63) Ruiz, R.; Dobisz, E.; Albrecht, T. R. Rectangular Patterns Using Block Copolymer Directed Assembly for High Bit Aspect Ratio Patterned Media. *ACS Nano* **2011**, *5*, 79–84.

(64) Diederichsen, K. M.; Brow, R. R.; Stoykovich, M. P. Percolating Transport and the Conductive Scaling Relationship in Lamellar Block Copolymers under Confinement. *ACS Nano* **2015**, *9*, 2465–2476.

(65) Ruiz, R.; Kang, H.; Detcheverry, F. A.; Dobisz, E.; Kercher, D. S.; Albrecht, T. R.; de Pablo, J. J.; Nealey, P. F. Density Multiplication and Improved Lithography by Directed Block Copolymer Assembly. *Science* **2008**, *321*, 936–939.

(66) Xiao, S.; Yang, X.; Park, S.; Weller, D.; Russell, T. P. A Novel Approach to Addressable 4 Teradot/in.2 Patterned Media. *Adv. Mater.* **2009**, *21*, 2516–2519.

(67) Tsai, H.; Pitera, J. W.; Miyazoe, H.; Bangsaruntip, S.; Engelmann, S. U.; Liu, C.-C.; Cheng, J. Y.; Bucchignano, J. J.; Klaus, D. P.; Joseph, E. A.; *et al.* Two-Dimensional Pattern Formation Using Graphoepitaxy of PS- b -PMMA Block Copolymers for Advanced FinFET Device and Circuit Fabrication. *ACS Nano* **2014**, *8*, 5227–5232.

(68) Daga, V. K.; Schwartz, E. L.; Chandler, C. M.; Lee, J. K.; Lin, Y.; Ober, C. K.; Watkins,

J. J. Photoinduced Ordering of Block Copolymers. *Nano Lett.* **2011**, *11*, 1153–1160.

(69) Onses, M. S.; Ramírez-Hernández, A.; Hur, S.-M.; Sutanto, E.; Williamson, L.; Alleyne, A. G.; Nealey, P. F.; de Pablo, J. J.; Rogers, J. A. Block Copolymer Assembly on Nanoscale Patterns of Polymer Brushes Formed by Electrohydrodynamic Jet Printing. *ACS Nano* **2014**, *8*, 6606–6613.

(70) Bosworth, J. K.; Paik, M. Y.; Ruiz, R.; Schwartz, E. L.; Huang, J. Q.; Ko, A. W.; Smilgies, D.-M.; Black, C. T.; Ober, C. K. Control of Self-Assembly of Lithographically Patternable Block Copolymer Films. *ACS Nano* **2008**, *2*, 1396–1402.

(71) Gotrik, K. W.; Hannon, A. F.; Son, J. G.; Keller, B.; Alexander-Katz, A.; Ross, C. A. Morphology Control in Block Copolymer Films Using Mixed Solvent Vapors. *ACS Nano* **2012**, *6*, 8052–8059.

(72) Conrado, R. J.; Varner, J. D.; DeLisa, M. P. Engineering the Spatial Organization of Metabolic Enzymes: Mimicking Nature's Synergy. *Curr. Opin. Biotechnol.* **2008**, *19*, 492–499.

(73) Jiang, H.; Wood, K. V; Morgan, J. A. Metabolic Engineering of the Phenylpropanoid Pathway in Saccharomyces Cerevisiae. *Appl. Environ. Microbiol.* **2005**, *71*, 2962–2969.

(74) Zhu, M. M.; Skraly, F. A.; Cameron, D. C. Accumulation of Methylglyoxal in Anaerobically Grown Escherichia Coli and Its Detoxification by Expression of the Pseudomonas Putida Glyoxalase I Gene. *Metab. Eng.* **2001**, *3*, 218–225.

(75) Locasale, J. W.; Cantley, L. C. Metabolic Flux and the Regulation of Mammalian Cell Growth. *Cell Metab.* **2011**, *14*, 443–451.

(76) Wheeldon, I.; Minteer, S. D.; Banta, S.; Barton, S. C.; Atanassov, P.; Sigman, M. Substrate Channelling as an Approach to Cascade Reactions. *Nat. Chem.* **2016**, *8*, 299–309.

(77) Hyde, C. C.; Ahmed, S. A.; Padlan, E. A.; Miles, E. W.; Davies, D. R. Thee-Dimensional Structure of the Tryptophan Synthase Alpha 2 Beta 2 Multienzyme Complex from Salmonella Typhimurium. *J. Biol. Chem.* **1988**, *263*, 17857–17871.

(78) Dunn, M. F.; Aguilar, V.; Brzović, P.; Leja, C. A.; Drewe, W. F.; Houben, K. F.; Roy, M. The Tryptophan Synthase Bienzyme Complex Transfers Indole between the α- and β-Sites via a 25-30 Å Long Tunnel. *Biochemistry* **1990**, *29*, 8598–8607.

(79) Thoden, J. B.; Holden, H. M.; Wesenberg, G.; Raushel, F. M.; Rayment, I. Structure of

Carbamoyl Phosphate Synthetase: A Journey of 96 Å from Substrate to Product. *Biochemistry* **1997**, *36*, 6305–6316.

(80) Krahn, J. M.; Kim, J. H.; Burns, M. R.; Parry, R. J.; Zalkin, H.; Smith, J. L. Coupled Formation of an Amidotransferase Interdomain Ammonia Channel and a Phosphoribosyltransferase Active Site. *Biochemistry* **1997**, *36*, 11061–11068.

(81) Larsen, T. M.; Boehlein, S. K.; Schuster, S. M.; Richards, N. G. J.; Thoden, J. B.; Holden, H. M.; Rayment, I. Three-Dimensional Structure of Escherichia Coli Asparagine Synthetase B: A Short Journey from Substrate to Product. *Biochemistry* **1999**, *38*, 16146–16157.

(82) Srere, P. Complexes Of Sequential Metabolic Enzymes. *Annu. Rev. Biochem.* **1987**, *56*, 89–124.

(83) Robinson, J. B.; Srere, P. A. Organization of Krebs Tricarboxylic Acid Cycle Enzymes. *Biochem. Med.* **1985**, *33*, 149–157.

(84) Wu, F.; Minteer, S. Krebs Cycle Metabolon: Structural Evidence of Substrate Channeling Revealed by Cross-Linking and Mass Spectrometry. *Angew. Chemie Int. Ed.* **2015**, *54*, 1851–1854.

(85) Vélot, C.; Mixon, M. B.; Teige, M.; Srere, P. A. Model of a Quinary Structure between Krebs TCA Cycle Enzymes: A Model for the Metabolon. *Biochemistry* **1997**, *36*, 14271–14276.

(86) Shatalin, K.; Lebreton, S.; Rault-Leonardon, M.; Vélot, C.; Srere, P. A. Electrostatic Channeling of Oxaloacetate in a Fusion Protein of Porcine Citrate Synthase and Porcine Mitochondrial Malate Dehydrogenase. *Biochemistry* **1999**, *38*, 881–889.

(87) French, J. B.; Jones, S. A.; Deng, H.; Pedley, A. M.; Kim, D.; Chan, C. Y.; Hu, H.; Pugh, R. J.; Zhao, H.; Zhang, Y.; *et al.* Spatial Colocalization and Functional Link of Purinosomes with Mitochondria. *Science (80-.).* **2016**, *351*, 733–737.

(88) An, S.; Kumar, R.; Sheets, E. D.; Benkovic, S. J. Reversible Compartmentalization of de Novo Purine Biosynthetic Complexes in Living Cells. *Science* **2008**, *320*, 103–106.

(89) Leivar, P.; González, V. M.; Castel, S.; Trelease, R. N.; López-Iglesias, C.; Arró, M.; Boronat, A.; Campos, N.; Ferrer, A.; Fernàndez-Busquets, X. Subcellular Localization of Arabidopsis 3-Hydroxy-3-Methylglutaryl-Coenzyme A Reductase. *Plant Physiol.* **2005**, *137*, 57–69.

(90) Welch, G. R.; Gaertner, F. H. Enzyme Organization in the Polyaromatic—Biosynthetic Pathway: The Arom Conjugate and Other Multienzyme Systems. *Curr. Top. Cell. Regul.* **1980**, *16*, 113–162.

(91) Burbulis, I. E.; Winkel-Shirley, B. Interactions among Enzymes of the Arabidopsis Flavonoid Biosynthetic Pathway. *Proc. Natl. Acad. Sci.* **1999**, *96*, 12929–12934.

(92) Ishikawa, M.; Tsuchiya, D.; Oyama, T.; Tsunaka, Y.; Morikawa, K. Structural Basis for Channelling Mechanism of a Fatty Acid Beta-Oxidation Multienzyme Complex. *EMBO J.* **2004**, *23*, 2745–2754.

(93) Kerfeld, C. A.; Sawaya, M. R.; Tanaka, S.; Nguyen, C. V; Phillips, M.; Beeby, M.; Yeates, T. O. Microbiology: Protein Structures Forming the Shell of Primitive Bacterial Organelles. *Science (80-.).* **2005**, *309*, 936–938.

(94) Doi, R. H.; Kosugi, A. Cellulosomes: Plant-Cell-Wall-Degrading Enzyme Complexes. *Nat. Rev. Microbiol.* **2004**, *2*, 541–551.

(95) Bayer, E. A.; Shimon, L. J. W.; Shoham, Y.; Lamed, R. Cellulosomes—Structure and Ultrastructure. *J. Struct. Biol.* **1998**, *124*, 221–234.

(96) Dhanasekaran, D. N.; Kashef, K.; Lee, C. M.; Xu, H.; Reddy, E. P. Scaffold Proteins of MAP-Kinase Modules. *Oncogene* **2007**, *26*, 3185–3202.

(97) Huang, P.-S.; Boyken, S. E.; Baker, D. The Coming of Age of de Novo Protein Design. *Nature* **2016**, *537*, 320–327.

(98) Dueber, J. E.; Wu, G. C.; Malmirchegini, G. R.; Moon, T. S.; Petzold, C. J.; Ullal, A. V; Prather, K. L. J.; Keasling, J. D. Synthetic Protein Scaffolds Provide Modular Control over Metabolic Flux. *Nat. Biotechnol.* **2009**, *27*, 753–759.

(99) Wilner, O. I.; Weizmann, Y.; Gill, R.; Lioubashevski, O.; Freeman, R.; Willner, I. Enzyme Cascades Activated on Topologically Programmed DNA Scaffolds. *Nat. Nanotechnol.* **2009**, *4*, 249–254.

(100) Berg, H. C. *Random Walks in Biology*; Princeton University Press: Princeton, N.J., 1983.

(101) Idan, O.; Hess, H. Origins of Activity Enhancement in Enzyme Cascades on Scaffolds. *ACS Nano* **2013**, *7*, 8658–8665.

(102) Goldstein, L.; Levin, Y.; Katchalski, E. A Water-Insoluble Polyanionic Derivative of Trypsin. II. Effect of the Polyelectrolyte Carrier on the Kinetic Behavior of the Bound

Trypsin *. *Biochemistry* **1964**, *3*, 1913–1919.

(103) Idan, O.; Hess, H. Diffusive Transport Phenomena in Artificial Enzyme Cascades on Scaffolds. *Nature Nanotechnology*, 2012, *7*, 769–770.

(104) Castellana, M.; Wilson, M. Z.; Xu, Y.; Joshi, P.; Cristea, I. M.; Rabinowitz, J. D.; Gitai, Z.; Wingreen, N. S. Enzyme Clustering Accelerates Processing of Intermediates through Metabolic Channeling. *Nat. Biotechnol.* **2014**, *32*, 1011–1018.

(105) Buchner, A.; Tostevin, F.; Gerland, U. Clustering and Optimal Arrangement of Enzymes in Reaction-Diffusion Systems. *Phys. Rev. Lett.* **2013**, *110*, 208104.

(106) Buchner, A.; Tostevin, F.; Hinzpeter, F.; Gerland, U. Optimization of Collective Enzyme Activity via Spatial Localization. *J. Chem. Phys.* **2013**, *139*, 135101.

(107) Klibanov, A. M. Improving Enzymes by Using Them in Organic Solvents. *Nature* **2001**, *409*, 241–246.

(108) Zaks, A.; Klibanov, A. M. Enzymatic Catalysis in Organic Media at 100 Degrees C. *Science (80-.).* **1984**, *224*, 1249–1251.

(109) Wescott, C. R.; Klibanov, A. M. The Solvent Dependence of Enzyme Specificity. *Biochim. Biophys. Acta - Protein Struct. Mol. Enzymol.* **1994**, *1206*, 1–9.

(110) Fitzpatrick, P. A.; Steinmetz, A. C.; Ringe, D.; Klibanov, A. M. Enzyme Crystal Structure in a Neat Organic Solvent. *Proc. Natl. Acad. Sci. U. S. A.* **1993**, *90*, 8653–8657.

(111) Kanerva, L. T.; Klibanov, A. M. Hammett Analysis of Enzyme Action in Organic Solvents. *J. Am. Chem. Soc.* **1989**, *111*, 6864–6865.

(112) Adams, K. A. H.; Chung, S. H.; Klibanov, A. M. Kinetic Isotope Effect Investigation of Enzyme Mechanisms in Organic Solvents. *J. Am. Chem. Soc.* **1990**, *112*, 9418–9419.

(113) Burke, P. A.; Griffin, R. G.; Klibanov, A. M. Solid-State Nuclear Magnetic Resonance Investigation of Solvent Dependence of Tyrosyl Ring Motion in an Enzyme. *Biotechnol. Bioeng.* **1993**, *42*, 87–94.

(114) Broos, J.; Visser, A. J. W. G.; Engbersen, J. F. J.; Verboom, W.; van Hoek, A.; Reinhoudt, D. N. Flexibility of Enzymes Suspended in Organic Solvents Probed by Time-Resolved Fluorescence Anisotropy. Evidence That Enzyme Activity and Enantioselectivity Are Directly Related to Enzyme Flexibility. *J. Am. Chem. Soc.* **1995**, *117*, 12657–12663.

(115) Ema, T.; Kobayashi, J.; Maeno, S.; Sakai, T.; Utaka, M. Origin of the Enantioselectivity of Lipases Explained by a Stereo-Sensing Mechanism Operative at the Transition State. *Bull. Chem. Soc. Jpn.* **1998**, *71*, 443–453.

(116) van Rantwijk, F.; Madeira Lau, R.; Sheldon, R. A. Biocatalytic Transformations in Ionic Liquids. *Trends Biotechnol.* **2003**, *21*, 131–138.

(117) de María, P. D. *Ionic Liquids in Biotransformations and Organocatalysis: Solvents and Beyond*; Domínguez de María, P., Ed.; John Wiley & Sons, Inc.: Hoboken, NJ, USA, 2012.

(118) Sheldon, R. Catalytic Reactions in Ionic Liquids. *Chem. Commun.* **2001**, *0*, 2399–2407.

(119) Dupont, J.; De Souza, R. F.; Suarez, P. A. Z. Ionic Liquid (Molten Salt) Phase Organometallic Catalysis. *Chem. Rev.* **2002**, *102*, 3667–3692.

(120) Walker, A. J.; Bruce, N. C. Combined Biological and Chemical Catalysis in the Preparation of Oxycodone. *Tetrahedron* **2004**, *60*, 561–568.

(121) Walker, A. J.; Bruce, N. C. Cofactor-Dependent Enzyme Catalysis in Functionalized Ionic Solvents. *Chem. Commun.* **2004**, *0*, 2570.

(122) Hussain, W.; Pollard, D. J.; Truppo, M.; Lye, G. J. Enzymatic Ketone Reductions with Co-Factor Recycling: Improved Reactions with Ionic Liquid Co-Solvents. *J. Mol. Catal. B Enzym.* **2008**, *55*, 19–29.

(123) Gaisberger, R. P.; Fechter, M. H.; Griengl, H. The First Hydroxynitrile Lyase Catalysed Cyanohydrin Formation in Ionic Liquids. *Tetrahedron Asymmetry* **2004**, *15*, 2959–2963.

(124) Lourenço, N. M. T.; Afonso, C. A. M. One-Pot Enzymatic Resolution and Separation of Sec-Alcohols Based on Ionic Acylating Agents. *Angew. Chemie - Int. Ed.* **2007**, *46*, 8178–8181.

(125) Lourenço, N. M. T.; Monteiro, C. M.; Afonso, C. A. M. Ionic Acylating Agents for the Enzymatic Resolution of Sec-Alcohols in Ionic Liquids. *European J. Org. Chem.* **2010**, *2010*, 6938–6943.

(126) Teixeira, R.; Lourenço, N. M. T. Enzymatic Kinetic Resolution of Sec-Alcohols Using an Ionic Liquid Anhydride as Acylating Agent. *Tetrahedron Asymmetry* **2014**, *25*, 944–948.

(127) Singh, M.; Singh, R. S.; Banerjee, U. C. Stereoselective Synthesis of (R)-1-Chloro-3(3,4-Difluorophenoxy)-2-Propanol Using Lipases from Pseudomonas Aeruginosa in Ionic

Liquid-Containing System. *J. Mol. Catal. B Enzym.* **2009**, *56*, 294–299.

(128) Park, S.; Kazlauskas, R. J. Improved Preparation and Use of Room-Temperature Ionic Liquids in Lipase-Catalyzed Enantio- and Regioselective Acylations. *J. Org. Chem.* **2001**, *66*, 8395–8401.

(129) Hara, P.; Hanefeld, U.; Kanerva, L. T. Immobilised Burkholderia Cepacia Lipase in Dry Organic Solvents and Ionic Liquids: A Comparison. *Green Chem.* **2009**, *11*, 250–256.

(130) Lou, W.-Y.; Zong, M.-H. Efficient Kinetic Resolution of (R,S)-1-Trimethylsilylethanol via Lipase-Mediated Enantioselective Acylation in Ionic Liquids. *Chirality* **2006**, *18*, 814–821.

(131) Lozano, P.; de Diego, T.; Guegan, J.-P.; Vaultier, M.; Iborra, J. L. Stabilization of ?-Chymotrypsin by Ionic Liquids in Transesterification Reactions. *Biotechnol. Bioeng.* **2001**, *75*, 563–569.

(132) Pace, C. N.; Trevino, S.; Prabhakaran, E.; Scholtz, J. M. Protein Structure, Stability and Solubility in Water and Other Solvents. *Philos. Trans. R. Soc. London Ser. B-Biological Sci.* **2004**, *359*, 1225–1234.

(133) Huang, M.-M.; Jiang, Y.; Sasisanker, P.; Driver, G. W.; Weingärtner, H. Static Relative Dielectric Permittivities of Ionic Liquids at 25 °C. *J. Chem. Eng. Data* **2011**, *56*, 1494–1499.

(134) Halling, P. J. Thermodynamic Predictions for Biocatalysis in Nonconventional Media: Theory, Tests, and Recommendations for Experimental Design and Analysis. *Enzyme Microb. Technol.* **1994**, *16*, 178–206.

(135) Moniruzzaman, M.; Kamiya, N.; Nakashima, K.; Goto, M. Water-in-Ionic Liquid Microemulsions as a New Medium for Enzymatic Reactions. *Green Chem.* **2008**, *10*, 497.

(136) Pavlidis, I. V.; Gournis, D.; Papadopoulos, G. K.; Stamatis, H. Lipases in Water-in-Ionic Liquid Microemulsions: Structural and Activity Studies. *J. Mol. Catal. B Enzym.* **2009**, *60*, 50–56.

(137) Zhou, G. P.; Zhang, Y.; Huang, X. R.; Shi, C. H.; Liu, W. F.; Li, Y. Z.; Qu, Y. B.; Gao, P. J. Catalytic Activities of Fungal Oxidases in Hydrophobic Ionic Liquid 1-Butyl-3-Methylimidazolium Hexafluorophosphate-Based Microemulsion. *Colloids Surfaces B Biointerfaces* **2008**, *66*, 146–149.

(138) Straathof, A. J. J. Enzymatic Catalysis via Liquid-Liquid Interfaces. *Biotechnol. Bioeng.*

2003, *83*, 371–375.

(139) Goto, M.; Kamiya, N.; Miyata, M.; Nakashio, F. Enzymic Esterification by Surfactant-Coated Lipase in Organic Media. *Biotechnol. Prog.* **1994**, *10*, 263–268.

(140) Kamiya, N.; Okazaki, S.; Goto, M. Surfactant-Horseradish Peroxidase Complex Catalytically Active in Anhydrous Benzene. *Biotechnol. Tech.* **1997**, *11*, 375–378.

(141) Kamiya, N.; Inoue, M.; Goto, M.; Nakamura, N.; Naruta, Y. Catalytic and Structural Properties of Surfactant-Horseradish Peroxidase Complex in Organic Media. *Biotechnol. Prog.* **2000**, *16*, 52–58.

(142) Bindhu, L. V.; Emilia Abraham, T. Preparation and Kinetic Studies of Surfactant–Horseradish Peroxidase Ion Paired Complex in Organic Media. *Biochem. Eng. J.* **2003**, *15*, 47–57.

(143) Brogan, A. P. S.; Hallett, J. P. Solubilizing and Stabilizing Proteins in Anhydrous Ionic Liquids through Formation of Protein–Polymer Surfactant Nanoconstructs. *J. Am. Chem. Soc.* **2016**, *138*, 4494–4501.

(144) Brogan, A. P. S.; Bui-Le, L.; Hallett, J. P. Non-Aqueous Homogenous Biocatalytic Conversion of Polysaccharides in Ionic Liquids Using Chemically Modified Glucosidase. *Nat. Chem.* **2018**, *10*, 859–865.

(145) Castillo, B.; Solá, R. J.; Ferrer, A.; Barletta, G.; Griebenow, K. Effect of PEG Modification on Subtilisin Carlsberg Activity, Enantioselectivity, and Structural Dynamics in 1,4-Dioxane. *Biotechnol. Bioeng.* **2008**, *99*, 9–17.

(146) Konieczny, S.; Fik, C. P.; Averesch, N. J. H.; Tiller, J. C. Organosoluble Enzyme Conjugates with Poly(2-Oxazoline)s via Pyromellitic Acid Dianhydride. *J. Biotechnol.* **2012**, *159*, 195–203.

(147) Konieczny, S.; Krumm, C.; Doert, D.; Neufeld, K.; Tiller, J. C. Investigations on the Activity of Poly(2-Oxazoline) Enzyme Conjugates Dissolved in Organic Solvents. *J. Biotechnol.* **2014**, *181*, 55–63.

(148) Cummings, C. S.; Murata, H.; Matyjaszewski, K.; Russell, A. J. Polymer-Based Protein Engineering Enables Molecular Dissolution of Chymotrypsin in Acetonitrile. *ACS Macro Lett.* **2016**, *5*, 493–497.

(149) Nakashima, K.; Maruyama, T.; Kamiya, N.; Goto, M. Homogeneous Enzymatic Reactions in Ionic Liquids with Poly(Ethylene Glycol)-Modified Subtilisin. *Org. Biomol. Chem.*

2006, *4*, 3462.

(150) Nakashima, K.; Okada, J.; Maruyama, T.; Kamiya, N.; Goto, M. Activation of Lipase in Ionic Liquids by Modification with Comb-Shaped Poly(Ethylene Glycol). *Sci. Technol. Adv. Mater.* **2006**, *7*, 692–698.

(151) Vandenbergh, J.; Junkers, T. Alpha and Omega: Importance of the Nonliving Chain End in Raft Multiblock Copolymerization. *Macromolecules* **2014**, *47*, 5051–5059.

(152) Li, H.; Bapat, A. P.; Li, M.; Sumerlin, B. S. Protein Conjugation of Thermoresponsive Amine-Reactive Polymers Prepared by RAFT. *Polym. Chem.* **2011**, *2*, 323–327.

(153) Li, H.; Li, M.; Yu, X.; Bapat, A. P.; Sumerlin, B. S. Block Copolymer Conjugates Prepared by Sequentially Grafting from Proteins via RAFT. *Polym. Chem.* **2011**, *2*, 1531.

(154) Dukes, D.; Li, Y.; Lewis, S.; Benicewicz, B.; Schadler, L.; Kumar, S. K. Conformational Transitions of Spherical Polymer Brushes: Synthesis, Characterization, and Theory. *Macromolecules* **2010**, *43*, 1564–1570.

(155) Shimoboji, T.; Ding, Z. L.; Stayton, P. S.; Hoffman, A. S. Photoswitching of Ligand Association with a Photoresponsive Polymer−Protein Conjugate. *Bioconjug. Chem.* **2002**, *13*, 915–919.

(156) Shimoboji, T.; Larenas, E.; Fowler, T.; Kulkarni, S.; Hoffman, A. S.; Stayton, P. S. Photoresponsive Polymer-Enzyme Switches. *Proc. Natl. Acad. Sci. U. S. A.* **2002**, *99*, 16592–16596.

(157) Ueki, T.; Nakamura, Y.; Yamaguchi, A.; Niitsuma, K.; Lodge, T. P.; Watanabe, M. UCST Phase Transition of Azobenzene-Containing Random Copolymer in an Ionic Liquid. *Macromolecules* **2011**, *44*, 6908–6914.

(158) Murata, H.; Cummings, C. S.; Koepsel, R. R.; Russell, A. J. Polymer-Based Protein Engineering Can Rationally Tune Enzyme Activity, PH-Dependence, and Stability. *Biomacromolecules* **2013**, *14*, 1919–1926.

(159) Bulmus, V.; Ding, Z.; Long, C. J.; Stayton, P. S.; Hoffman, A. S. Site-Specific Polymer−Streptavidin Bioconjugate for PH-Controlled Binding and Triggered Release of Biotin. *Bioconjug. Chem.* **2000**, *11*, 78–83.

(160) Chen, L.; Honma, Y.; Mizutani, T.; Liaw, D.-J.; Gong, J. .; Osada, Y. Effects of Polyelectrolyte Complexation on the UCST of Zwitterionic Polymer. *Polymer (Guildf).* **2000**, *41*, 141–147.

(161) Fujii, K.; Ueki, T.; Hashimoto, K.; Kobayashi, Y.; Kitazawa, Y.; Hirosawa, K.; Matsugami, M.; Ohara, K.; Watanabe, M.; Shibayama, M. Microscopic Structure of Solvated Poly(Benzyl Methacrylate) in an Imidazolium-Based Ionic Liquid: High-Energy X-Ray Total Scattering and All-Atom MD Simulation Study. *Macromolecules* **2017**, *50*, 4780–4786.

(162) Liu, H.; Zhang, J.; Luo, X.; Kong, N.; Cui, L.; Liu, J. Preparation of Biodegradable and Thermoresponsive Enzyme-Polymer Conjugates with Controllable Bioactivity via RAFT Polymerization. *Eur. Polym. J.* **2013**, *49*, 2949–2960.

(163) Lou, L.-L.; Qu, H.; Yu, W.; Wang, B.; Ouyang, L.; Liu, S.; Zhou, W. Covalently Immobilized Lipase on a Thermoresponsive Polymer with an Upper Critical Solution Temperature as an Efficient and Recyclable Asymmetric Catalyst in Aqueous Media. *ChemCatChem* **2018**, *10*, 1166–1172.

(164) Limadinata, P. A.; Li, A.; Li, Z. Temperature-Responsive Nanobiocatalysts with an Upper Critical Solution Temperature for High Performance Biotransformation and Easy Catalyst Recycling: Efficient Hydrolysis of Cellulose to Glucose. *Green Chem.* **2015**, *17*, 1194–1203.

(165) Cummings, C.; Murata, H.; Koepsel, R.; Russell, A. J. Tailoring Enzyme Activity and Stability Using Polymer-Based Protein Engineering. *Biomaterials* **2013**, *34*, 7437–7443.

(166) Hoffman, A. S.; Stayton, P. S. Conjugates of Stimuli-Responsive Polymers and Proteins. *Prog. Polym. Sci.* **2007**, *32*, 922–932.

(167) Mackenzie, K. J.; Francis, M. B. Recyclable Thermoresponsive Polymer–Cellulase Bioconjugates for Biomass Depolymerization. *J. Am. Chem. Soc.* **2013**, *135*, 293–300.

(168) De, P.; Li, M.; Gondi, S. R.; Sumerlin, B. S. Temperature-Regulated Activity of Responsive Polymer-Protein Conjugates Prepared by Grafting-from via RAFT Polymerization. *J. Am. Chem. Soc.* **2008**, *130*, 11288–11289.

(169) Cobo, I.; Li, M.; Sumerlin, B. S.; Perrier, S. Smart Hybrid Materials by Conjugation of Responsive Polymers to Biomacromolecules. *Nat. Mater.* **2015**, *14*, 143–149.

(170) Zhang, Y.; Dai, Y.; Hou, M.; Li, T.; Ge, J.; Liu, Z. Chemo-Enzymatic Synthesis of Valrubicin Using Pluronic Conjugated Lipase with Temperature Responsiveness in Organic Media. *RSC Adv.* **2013**, *3*, 22963–22966.

(171) Zhu, J.; Zhang, Y.; Lu, D.; Zare, R. N.; Ge, J.; Liu, Z. Temperature-Responsive Enzyme-Polymer Nanoconjugates with Enhanced Catalytic Activities in Organic Media. *Chem. Commun.* **2013**, *49*, 6090–6092.

(172) Hou, M.; Wang, R.; Wu, X.; Zhang, Y.; Ge, J.; Liu, Z. Synthesis of Lutein Esters by Using a Reusable Lipase-Pluronic Conjugate as the Catalyst. *Catal. Letters* **2015**, *145*, 1825–1829.

(173) Zhang, Y.; Ge, J.; Liu, Z. Enhanced Activity of Immobilized or Chemically Modified Enzymes. *ACS Catal.* **2015**, *5*, 4503–4513.

(174) Aissou, K.; Mumtaz, M.; Fleury, G.; Portale, G.; Navarro, C.; Cloutet, E.; Brochon, C.; Ross, C. A.; Hadziioannou, G. Sub-10 Nm Features Obtained from Directed Self-Assembly of Semicrystalline Polycarbosilane-Based Block Copolymer Thin Films. *Adv. Mater.* **2015**, *27*, 261–265.

(175) Cheng, J. Y.; Ross, C. A.; Chan, V. Z. H.; Thomas, E. L.; Lammertink, R. G. H.; Vancso, G. J. Formation of a Cobalt Magnetic Dot Array via Block Copolymer Lithography. *Adv. Mater.* **2001**, *13*, 1174–1178.

(176) Tang, C.; Lennon, E. M.; Fredrickson, G. H.; Kramer, E. J.; Hawker, C. J. Evolution of Block Copolymer Square Arrays. *Science (80-.).* **2008**, *322*, 429–432.

(177) He, C.; Stoykovich, M. P. Profile Control in Block Copolymer Nanostructures Using Bilayer Thin Films for Enhanced Pattern Transfer Processes. *Adv. Funct. Mater.* **2014**, *24*, 7078–7084.

(178) Campbell, I. P.; He, C.; Stoykovich, M. P. Topologically Distinct Lamellar Block Copolymer Morphologies Formed by Solvent and Thermal Annealing. *ACS Macro Lett.* **2013**, *2*, 918–923.

(179) Sinturel, C.; Vayer, M.; Morris, M.; Hillmyer, M. A. Solvent Vapor Annealing of Block Polymer Thin Films. *Macromolecules* **2013**, *46*, 5399–5415.

(180) Han, E.; Stuen, K. O.; La, Y.-H.; Nealey, P. F.; Gopalan, P. Effect of Composition of Substrate-Modifying Random Copolymers on the Orientation of Symmetric and Asymmetric Diblock Copolymer Domains. *Macromolecules* **2008**, *41*, 9090–9097.

(181) Maher, M. J.; Bates, C. M.; Blachut, G.; Carlson, M. C.; Self, J. L.; Janes, D. W.; Durand, W. J.; Lane, A. P.; Ellison, C. J.; Willson, C. G. Photopatternable Interfaces for Block Copolymer Lithography. *ACS Macro Lett.* **2014**, *3*, 824–828.

(182) Farrell, R. A.; Kehagias, N.; Shaw, M. T.; Reboud, V.; Zelsmann, M.; Holmes, J. D.; Sotomayor Torres, C. M.; Morris, M. A. Surface-Directed Dewetting of a Block Copolymer for Fabricating Highly Uniform Nanostructured Microdroplets and Concentric Nanorings. *ACS Nano* **2011**, *5*, 1073–1085.

(183) Cecchini, G. Function and Structure of Complex II of the Respiratory Chain. *Annu. Rev. Biochem.* **2003**, *72*, 77–109.

(184) Nelson, N.; Ben-Shem, A. The Complex Architecture of Oxygenic Photosynthesis. *Nat. Rev. Mol. Cell Biol.* **2004**, *5*, 971–982.

(185) Bayer, E. A.; Belaich, J.-P.; Shoham, Y.; Lamed, R. The Cellulosomes: Multienzyme Machines for Degradation of Plant Cell Wall Polysaccharides. *Annu. Rev. Microbiol.* **2004**, *58*, 521–554.

(186) Noree, C.; Sato, B. K.; Broyer, R. M.; Wilhelm, J. E. Identification of Novel Filament-Forming Proteins in Saccharomyces Cerevisiae and Drosophila Melanogaster. *J. Cell Biol.* **2010**, *190*, 541–551.

(187) An, S.; Deng, Y.; Tomsho, J. W.; Kyoung, M.; Benkovic, S. J. Microtubule-Assisted Mechanism for Functional Metabolic Macromolecular Complex Formation. *Proc. Natl. Acad. Sci.* **2010**, *107*, 12872–12876.

(188) Shoham, Y.; Lamed, R.; Bayer, E. A. The Cellulosome Concept as an Efficient Microbial Strategy for the Degradation of Insoluble Polysaccharides. *Trends Microbiol.* **1999**, *7*, 275–281.

(189) Park, M.; Sun, Q.; Liu, F.; DeLisa, M. P.; Chen, W. Positional Assembly of Enzymes on Bacterial Outer Membrane Vesicles for Cascade Reactions. *PLoS One* **2014**, *9*, e97103.

(190) You, C.; Myung, S.; Zhang, Y.-H. P. Facilitated Substrate Channeling in a Self-Assembled Trifunctional Enzyme Complex. *Angew. Chem. Int. Ed. Engl.* **2012**, *51*, 8787–8790.

(191) Moehlenbrock, M. J.; Meredith, M. T.; Minteer, S. D. Bioelectrocatalytic Oxidation of Glucose in CNT Impregnated Hydrogels: Advantages of Synthetic Enzymatic Metabolon Formation. *ACS Catal.* **2012**, *2*, 17–25.

(192) Sarma, A. K.; Vatsyayan, P.; Goswami, P.; Minteer, S. D. Recent Advances in Material Science for Developing Enzyme Electrodes. *Biosens. Bioelectron.* **2009**, *24*, 2313–2322.

(193) Lee, H.; DeLoache, W. C.; Dueber, J. E. Spatial Organization of Enzymes for Metabolic Engineering. *Metab. Eng.* **2012**, *14*, 242–251.

(194) Conrado, R. J.; Wu, G. C.; Boock, J. T.; Xu, H.; Chen, S. Y.; Lebar, T.; Turnšek, J.; Tomšič, N.; Avbelj, M.; Gaber, R.; *et al.* DNA-Guided Assembly of Biosynthetic Pathways Promotes Improved Catalytic Efficiency. *Nucleic Acids Res.* **2012**, *40*, 1879–

1889.

(195) Pröschel, M.; Detsch, R.; Boccaccini, A. R.; Sonnewald, U. Engineering of Metabolic Pathways by Artificial Enzyme Channels. *Front. Bioeng. Biotechnol.* **2015**, *3*, 168.

(196) Lin, J. L.; Palomec, L.; Wheeldon, I. Design and Analysis of Enhanced Catalysis in Scaffolded Multienzyme Cascade Reactions. *ACS Catalysis*, 2014, *4*, 505–511.

(197) Ngo, T. A.; Nakata, E.; Saimura, M.; Morii, T. Spatially Organized Enzymes Drive Cofactor-Coupled Cascade Reactions. *J. Am. Chem. Soc.* **2016**, *138*, 3012–3021.

(198) Mosiewicz, K. A.; Kolb, L.; van der Vlies, A. J.; Martino, M. M.; Lienemann, P. S.; Hubbell, J. A.; Ehrbar, M.; Lutolf, M. P. In Situ Cell Manipulation through Enzymatic Hydrogel Photopatterning. *Nat. Mater.* **2013**, *12*, 1072–1078.

(199) Tolstyka, Z. P.; Richardson, W.; Bat, E.; Stevens, C. J.; Parra, D. P.; Dozier, J. K.; Distefano, M. D.; Dunn, B.; Maynard, H. D. Chemoselective Immobilization of Proteins by Microcontact Printing and Bio-Orthogonal Click Reactions. *Chembiochem* **2013**, *14*, 2464–2471.

(200) Christman, K. L.; Schopf, E.; Broyer, R. M.; Li, R. C.; Chen, Y.; Maynard, H. D. Positioning Multiple Proteins at the Nanoscale with Electron Beam Cross-Linked Functional Polymers. *J. Am. Chem. Soc.* **2009**, *131*, 521–527.

(201) Kolodziej, C. M.; Maynard, H. D. Electron-Beam Lithography for Patterning Biomolecules at the Micron and Nanometer Scale. *Chem. Mater.* **2012**, *24*, 774–780.

(202) Killops, K. L.; Gupta, N.; Dimitriou, M. D.; Lynd, N. A.; Jung, H.; Tran, H.; Bang, J.; Campos, L. M. Nanopatterning Biomolecules by Block Copolymer Self-Assembly. *ACS Macro Lett.* **2012**, *1*, 758–763.

(203) Anderson, J. B.; Anderson, L. E.; Kussmann, J. Monte Carlo Simulations of Single- and Multistep Enzyme-Catalyzed Reaction Sequences: Effects of Diffusion, Cell Size, Enzyme Fluctuations, Colocalization, and Segregation. *J. Chem. Phys.* **2010**, *133*, 034104.

(204) Lineweaver, H.; Burk, D. The Determination of Enzyme Dissociation Constants. *J. Am. Chem. Soc.* **1934**, *56*, 658–666.

(205) Chang, F.-P.; Chen, Y.-P.; Mou, C.-Y. Intracellular Implantation of Enzymes in Hollow Silica Nanospheres for Protein Therapy: Cascade System of Superoxide Dismutase and Catalase. *Small* **2014**, *10*, 4785–4795.

(206) Urban, P. L.; Goodall, D. M.; Bruce, N. C. Enzymatic Microreactors in Chemical Analysis and Kinetic Studies. *Biotechnology Advances*, 2006, *24*, 42–57.

(207) Zhao, Z.; Fu, J.; Dhakal, S.; Johnson-Buck, A.; Liu, M.; Zhang, T.; Woodbury, N. W.; Liu, Y.; Walter, N. G.; Yan, H. Nanocaged Enzymes with Enhanced Catalytic Activity and Increased Stability against Protease Digestion. *Nat. Commun.* **2016**, *7*, 10619.

(208) Bauler, P.; Huber, G.; Leyh, T.; McCammon, J. A. Channeling by Proximity: The Catalytic Advantages of Active Site Colocalization Using Brownian Dynamics. *J. Phys. Chem. Lett.* **2010**, *1*, 1332–1335.

(209) El-Zahab, B.; Jia, H.; Wang, P. Enabling Multienzyme Biocatalysis Using Nanoporous Materials. *Biotechnol. Bioeng.* **2004**, *87*, 178–183.

(210) Stroud, R. M. An Electrostatic Highway. *Nat. Struct. Biol.* **1994**, *1*, 131–134.

(211) Yamada, Y.; Tsung, C.-K.; Huang, W.; Huo, Z.; Habas, S. E.; Soejima, T.; Aliaga, C. E.; Somorjai, G. A.; Yang, P. Nanocrystal Bilayer for Tandem Catalysis. *Nat. Chem.* **2011**, *3*, 372–376.

(212) Wang, S.; Meng, X.; Zhou, H.; Liu, Y.; Secundo, F.; Liu, Y. Enzyme Stability and Activity in Non-Aqueous Reaction Systems: A Mini Review. *Catalysts* **2016**, *6*, 32.

(213) Lau, R. M.; Van Rantwijk, F.; Seddon, K. R.; Sheldon, R. A. Lipase-Catalyzed Reactions in Ionic Liquids. *Org. Lett.* **2000**, *2*, 4189–4191.

(214) Itoh, T.; Akasaki, E.; Kudo, K.; Shirakami, S. Lipase-Catalyzed Enantioselective Acylation in the Ionic Liquid Solvent System: Reaction of Enzyme Anchored to the Solvent. *Chem. Lett.* **2001**, *30*, 262–263.

(215) Schöfer, S. H.; Kaftzik, N.; Kragl, U.; Wasserscheid, P. Enzyme Catalysis in Ionic Liquids: Lipase Catalysed Kinetic Resolution of 1-Phenylethanol with Improved Enantioselectivity. *Chem. Commun.* **2001**, *0*, 425–426.

(216) Erbeldinger, M.; Mesiano, A. J.; Russell, A. J. Enzymatic Catalysis of Formation of Z-Aspartame in Ionic Liquid an Alternative to Enzymatic Catalysis in Organic Solvents. *Biotechnol. Prog.* **2000**, *16*, 1129–1131.

(217) Moniruzzaman, M.; Nakashima, K.; Kamiya, N.; Goto, M. Recent Advances of Enzymatic Reactions in Ionic Liquids. *Biochem. Eng. J.* **2010**, *48*, 295–314.

(218) van Rantwijk, F.; Sheldon, R. A. Biocatalysis in Ionic Liquids. *Chem. Rev.* **2007**, *107*,

2757–2785.

(219) Zhao, H. Methods for Stabilizing and Activating Enzymes in Ionic Liquids - A Review. *J. Chem. Technol. Biotechnol.* **2010**, *85*, 891–907.

(220) Ohno, H.; Suzuki, C.; Fukumoto, K.; Yoshizawa, M.; Fujita, K. Electron Transfer Process of Poly(Ethylene Oxide)-Modified Cytochrome c in Imidazolium Type Ionic Liquid. *Chem. Lett.* **2003**, *32*, 450–451.

(221) Sakai, S.; Kodama, L.; Matsumura, H.; Nakamura, N.; Yohda, M.; Ohno, H. Solubilization of Heme Proteins in Low Polar Solvents by Chemical Modification on a Protein's Surface. *Polym. Adv. Technol.* **2008**, *19*, 1430–1435.

(222) Nakashima, K.; Maruyama, T.; Kamiya, N.; Goto, M. Spectrophotometric Assay for Protease Activity in Ionic Liquids Using Chromogenic Substrates. *Anal. Biochem.* **2008**, *374*, 285–290.

(223) Ganske, F.; Bornscheuer, U. T. Lipase-Catalyzed Glucose Fatty Acid Ester Synthesis in Ionic Liquids. *Org. Lett.* **2005**, *7*, 3097–3098.

(224) Maruyama, T.; Yamamura, H.; Kotani, T.; Kamiya, N.; Goto, M. Poly(Ethylene Glycol)-Lipase Complexes That Are Highly Active and Enantioselective in Ionic Liquids. *Org. Biomol. Chem.* **2004**, *2*, 1239.

(225) Maruyama, T.; Nagasawa, S.; Goto, M. Poly(Ethylene Glycol)-Lipase Complex That Is Catalytically Active for Alcoholysis Reactions in Ionic Liquids. *Biotechnol. Lett.* **2002**, *24*, 1341–1345.

(226) Livi, S.; Duchet-Rumeau, J.; Gérard, J. F.; Pham, T. N. Polymers and Ionic Liquids: A Successful Wedding. *Macromol. Chem. Phys.* **2015**, *216*, 359–368.

(227) Lodge, T. P.; Ueki, T. Mechanically Tunable, Readily Processable Ion Gels by Self-Assembly of Block Copolymers in Ionic Liquids. *Acc. Chem. Res.* **2016**, *49*, 2107–2114.

(228) Gu, Y.; Lodge, T. P. Synthesis and Gas Separation Performance of Triblock Copolymer Ion Gels with a Polymerized Ionic Liquid Mid-Block. *Macromolecules* **2011**, *44*, 1732–1736.

(229) Ueki, T.; Watanabe, M. Polymers in Ionic Liquids: Dawn of Neoteric Solvents and Innovative Materials. *Bull. Chem. Soc. Jpn.* **2012**, *85*, 33–50.

(230) Lee, H.-N.; Newell, N.; Bai, Z.; Lodge, T. P. Unusual Lower Critical Solution

Temperature Phase Behavior of Poly(Ethylene Oxide) in Ionic Liquids. *Macromolecules* **2012**, *45*, 3627–3633.

(231) Nordwald, E. M.; Plaks, J. G.; Snell, J. R.; Sousa, M. C.; Kaar, J. L. Crystallographic Investigation of Imidazolium Ionic Liquid Effects on Enzyme Structure. *ChemBioChem* **2015**, *16*, 2456–2459.

(232) Nordwald, E. M.; Armstrong, G. S.; Kaar, J. L. NMR-Guided Rational Engineering of an Ionic-Liquid-Tolerant Lipase. *ACS Catal.* **2014**, *4*, 4057–4064.

(233) Marcus, Y. Room Temperature Ionic Liquids: Their Cohesive Energies, Solubility Parameters and Solubilities in Them. *J. Solution Chem.* **2017**, *46*, 1778–1791.

(234) Tucker, B. S.; Coughlin, M. L.; Figg, C. A.; Sumerlin, B. S. Grafting-From Proteins Using Metal-Free PET–RAFT Polymerizations under Mild Visible-Light Irradiation. *ACS Macro Lett.* **2017**, *6*, 452–457.

(235) Li, M.; De, P.; Li, H.; Sumerlin, B. S. Conjugation of RAFT-Generated Polymers to Proteins by Two Consecutive Thiol–Ene Reactions. *Polym. Chem.* **2010**, *1*, 854–859.

(236) Dong, X. H.; Obermeyer, A. C.; Olsen, B. D. Three-Dimensional Ordered Antibody Arrays Through Self-Assembly of Antibody–Polymer Conjugates. *Angew. Chemie - Int. Ed.* **2017**, *56*, 1273–1277.

(237) Obermeyer, A. C.; Mills, C. E.; Dong, X.-H.; Flores, R. J.; Olsen, B. D. Complex Coacervation of Supercharged Proteins with Polyelectrolytes. *Soft Matter* **2016**, *12*, 3570–3581.

(238) Zhang, Y.; Wang, Q.; Hess, H. Increasing Enzyme Cascade Throughput by PH-Engineering the Microenvironment of Individual Enzymes. *ACS Catal.* **2017**, *7*, 2047–2051.

(239) Lucius, M.; Falatach, R.; McGlone, C.; Makaroff, K.; Danielson, A.; Williams, C.; Nix, J. C.; Konkolewicz, D.; Page, R. C.; Berberich, J. A. Investigating the Impact of Polymer Functional Groups on the Stability and Activity of Lysozyme–Polymer Conjugates. *Biomacromolecules* **2016**, *17*, 1123–1134.

(240) Wright, T. A.; Lucius Dougherty, M.; Schmitz, B.; Burridge, K. M.; Makaroff, K.; Stewart, J. M.; Fischesser, H. D.; Shepherd, J. T.; Berberich, J. A.; Konkolewicz, D.; *et al.* Polymer Conjugation to Enhance Cellulase Activity and Preserve Thermal and Functional Stability. *Bioconjug. Chem.* **2017**, *28*, 2638–2645.

(241) Mancini, R. J.; Lee, J.; Maynard, H. D. Trehalose Glycopolymers for Stabilization of Protein Conjugates to Environmental Stressors. *J. Am. Chem. Soc.* **2012**, *134*, 8474–8479.

(242) Chen, X.; McRae, S.; Samanta, D.; Emrick, T. Polymer−Protein Conjugation in Ionic Liquids. *Macromolecules* **2010**, *43*, 6261–6263.

(243) Ueno, K.; Fukai, T.; Nagatsuka, T.; Yasuda, T.; Watanabe, M. Solubility of Poly(Methyl Methacrylate) in Ionic Liquids in Relation to Solvent Parameters. *Langmuir* **2014**, *30*, 3228–3235.

(244) Lee, S. H.; Lee, S. B. The Hildebrand Solubility Parameters, Cohesive Energy Densities and Internal Energies of 1-Alkyl-3-Methylimidazolium-Based Room Temperature Ionic Liquids. *Chem. Commun.* **2005**, *125*, 3469.

(245) Batista, M. L. S.; Neves, C. M. S. S.; Carvalho, P. J.; Gani, R.; Coutinho, J. A. P. Chameleonic Behavior of Ionic Liquids and Its Impact on the Estimation of Solubility Parameters. *J. Phys. Chem. B* **2011**, *115*, 12879–12888.

(246) Kharel, A.; Lodge, T. P. Coil Dimensions of Poly(Ethylene Oxide) in an Ionic Liquid by Small-Angle Neutron Scattering. *Macromolecules* **2017**, *50*, 8739–8744.

(247) Sheldon, R. A. Enzyme Immobilization: The Quest for Optimum Performance. *Adv. Synth. Catal.* **2007**, *349*, 1289–1307.

(248) Rodrigues, R. C.; Ortiz, C.; Berenguer-Murcia, Á.; Torres, R.; Fernández-Lafuente, R. Modifying Enzyme Activity and Selectivity by Immobilization. *Chem. Soc. Rev.* **2013**, *42*, 6290–6307.

(249) Hanefeld, U.; Gardossi, L.; Magner, E. Understanding Enzyme Immobilisation. *Chem. Soc. Rev.* **2009**, *38*, 453–468.

(250) Grazú, V.; López-Gallego, F.; Montes, T.; Abian, O.; González, R.; Hermoso, J. A.; García, J. L.; Mateo, C.; Guisán, J. M. Promotion of Multipoint Covalent Immobilization through Different Regions of Genetically Modified Penicillin G Acylase from E. Coli. *Process Biochem.* **2010**, *45*, 390–398.

(251) Tischer, W.; Kasche, V. Immobilized Enzymes: Crystals or Carriers? *Trends Biotechnol.* **1999**, *17*, 326–335.

(252) Wu, X.; Ge, J.; Zhu, J.; Zhang, Y.; Yong, Y.; Liu, Z. A General Method for Synthesizing Enzyme–Polymer Conjugates in Reverse Emulsions Using Pluronic as a Reactive Surfactant. *Chem. Commun.* **2015**, *51*, 9674–9677.

(253) Chado, G. R.; Holland, E. N.; Tice, A. K.; Stoykovich, M. P.; Kaar, J. L. Modification of Lipase with Poly(4-Acryloylmorpholine) Enhances Solubility and Transesterification Activity in Anhydrous Ionic Liquids. *Biomacromolecules* **2018**, *19*, 1324–1332.

(254) Niskanen, J.; Tenhu, H. How to Manipulate the Upper Critical Solution Temperature (UCST)? *Polym. Chem.* **2017**, *8*, 220–232.

(255) Seuring, J.; Agarwal, S. Polymers with Upper Critical Solution Temperature in Aqueous Solution. *Macromol. Rapid Commun.* **2012**, *33*, 1898–1920.

(256) Seuring, J.; Agarwal, S. First Example of a Universal and Cost-Effective Approach: Polymers with Tunable Upper Critical Solution Temperature in Water and Electrolyte Solution. *Macromolecules* **2012**, *45*, 3910–3918.

(257) Asai, H.; Fujii, K.; Ueki, T.; Sawamura, S.; Nakamura, Y.; Kitazawa, Y.; Watanabe, M.; Han, Y. S.; Kim, T. H.; Shibayama, M. Structural Study on the UCST-Type Phase Separation of Poly(N -Isopropylacrylamide) in Ionic Liquid. *Macromolecules* **2013**, *46*, 1101–1106.

(258) Ueki, T. Stimuli-Responsive Polymers in Ionic Liquids. *Polym. J.* **2014**, *46*, 646–655.

(259) Depp, V.; Kaar, J. L.; Russell, A. J.; Lele, B. S. Enzyme Sheathing Enables Nanoscale Solubilization of Biocatalyst and Dramatically Increases Activity in Organic Solvent. *Biomacromolecules* **2008**, *9*, 1348–1351.

(260) Panza, J. L.; Russell, A. J.; Beckman, E. J. Fluorinated NAD as an Affinity Surfactant. *Chem. Commun.* **2002**, *0*, 928–929.

(261) Lam, C. N.; Kim, M.; Thomas, C. S.; Chang, D.; Sanoja, G. E.; Okwara, C. U.; Olsen, B. D. The Nature of Protein Interactions Governing Globular Protein-Polymer Block Copolymer Self-Assembly. *Biomacromolecules* **2014**, *15*, 1248–1258.

(262) Obermeyer, A. C.; Olsen, B. D. Synthesis and Application of Protein-Containing Block Copolymers. *ACS Macro Lett.* **2015**, 101–110.

(263) Cassano, R.; Mellace, S.; Trombino, S. Responsive Polymer-Biomacromolecule Conjugates for Drug Delivery. *Stimuli Responsive Polym. Nanocarriers Drug Deliv. Appl. Vol. 1* **2018**, 433–452.

Appendix A: Supplemental Information

A.1 Accessing the Spectrum of Block Copolymer Morphologies in Thin Films Through Facile and Localized Multilayer Self-Assembly: Supplemental Information

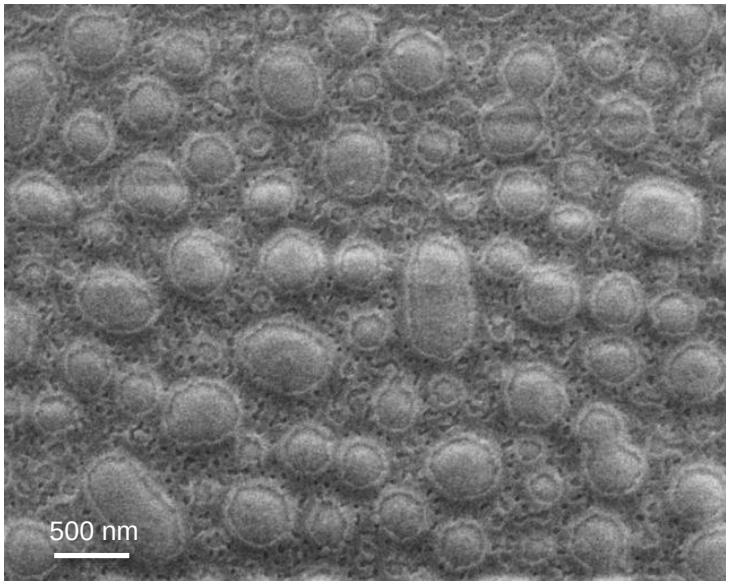

Figure A.1 Structure of the as-deposited multilayer films prior to annealing. Scanning electron micrograph of the structure after spin casting a 23 nm film of PS and PMMA homopolymers on top of a 45 nm film of lamellar-forming block copolymer. Light and dark colors in the SEM image correspond to the PS and PMMA domains, respectively.

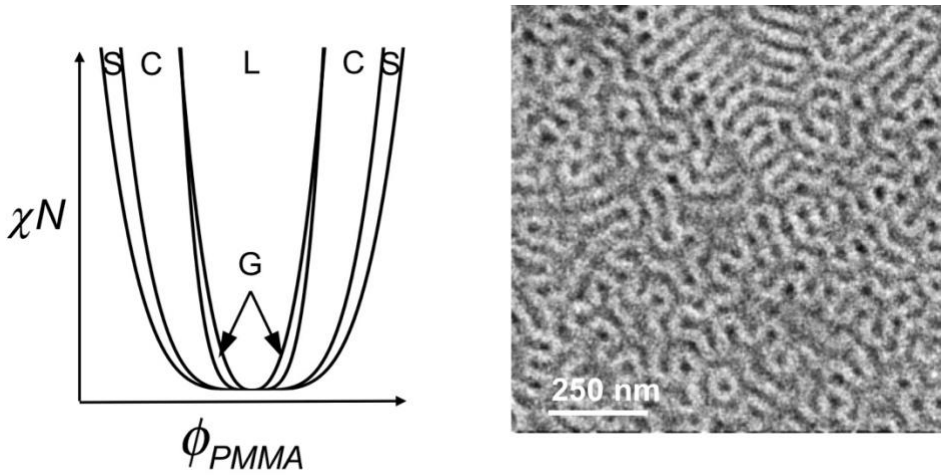

Figure A.2 Bicontinuous gyroid morphology self-assembled by multilayer mixing in thin films. The schematic phase diagram on the left illustrates regions between the cylindrical and lamellar morphologies in which a stable bicontinuous gyroid phase is observed. On the right, a SEM image displaying a gyroid structure achieved by bilayer blending between lamellar-forming (PS-b-PMMA 47-67 kg/mol) and cylinder-forming (PS-b-PMMA 46-21 kg/mol) block copolymers. The light and dark colors in the SEM images correspond to the PS and PMMA domains, respectively.

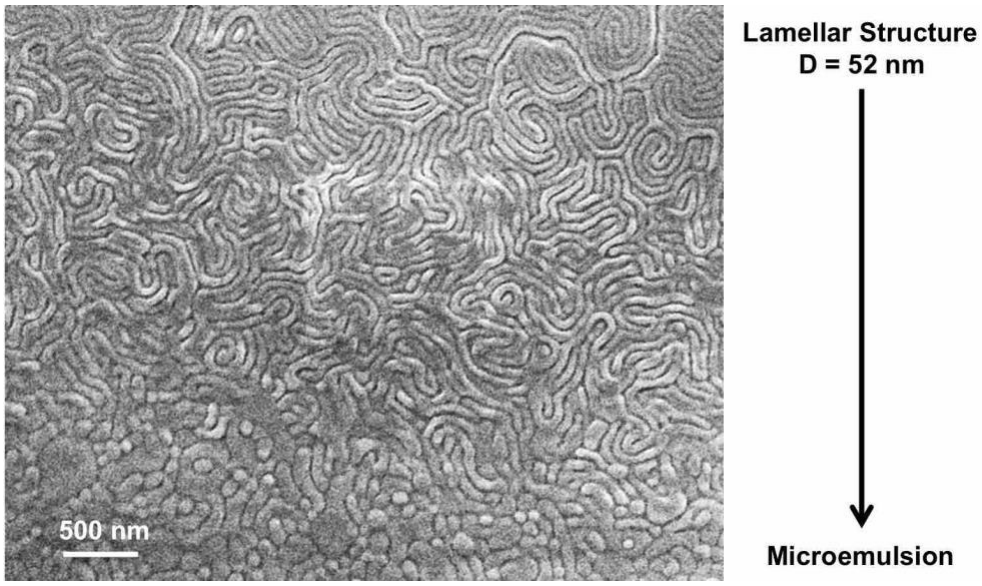

Figure A.3 Transition between lamellar and microemulsion structures formed by multilayer mixing of block copolymer and high concentrations of homopolymers. Scanning electron micrograph showing lamellar nanostructures self-assembled by a pure diblock copolymer (PS-b-PMMA 47-67 kg/mol with domain spacing of 52 nm) at the top being swollen symmetrically with PS and PMMA homopolymers until the lamellar structure was no longer stable and a microemulsion phase formed at the bottom. The light and dark colors in the SEM image correspond to the PS and PMMA domains, respectively. The first layer consisted of a 33 nm film of the lamellar PS-b-PMMA. Photo-initiated cross-linking and fixation of the lamellar structures was performed in select regions (top here) by optical lithography. A second layer consisting of a 39 nm film of a PS/PMMA homopolymer blend was subsequently deposited and annealed to allow for mixing of the polymer components. A microemulsion was formed because of the high concentration of homopolymer ($\phi_h \gtrsim 0.5$) in the blend region.

Note that the continuous transition between the lamellar and microemulsion structures (which extend far beyond the imaged region to the top and bottom, respectively) arises due to issues with the optical lithography process that blur the boundary between the mixed and unmixed regions. Over this transition region, the lamellae increase in dimension (from top to bottom) indicating an increase in homopolymer concentration blended in the film (from 0 to >50 %), and results from varying extents of partial crosslinking of the block copolymer lamellae (from high to none) that modulate the susceptibility of the first layer to swelling and mixing with the homopolymer provided in the second layer. Improvements to the lithographic process (*i.e.*, reduction in optical diffraction and control over the diffusion of the photo-initiated species) may be used to sharpen and eliminate this transition region.

A.2 Role of Dimension and Spatial Arrangement on the Activity of Coupled Biocatalytic Reactions on Scaffolds: Supplemental Information

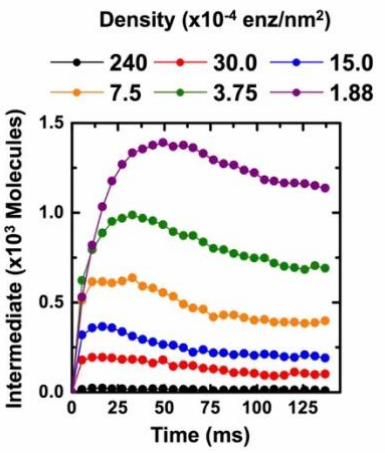

Figure A.4 Concentration of intermediate molecules in the simulation volume as a function of time for enzymes randomly immobilized on surfaces under diffusion-limited conditions.

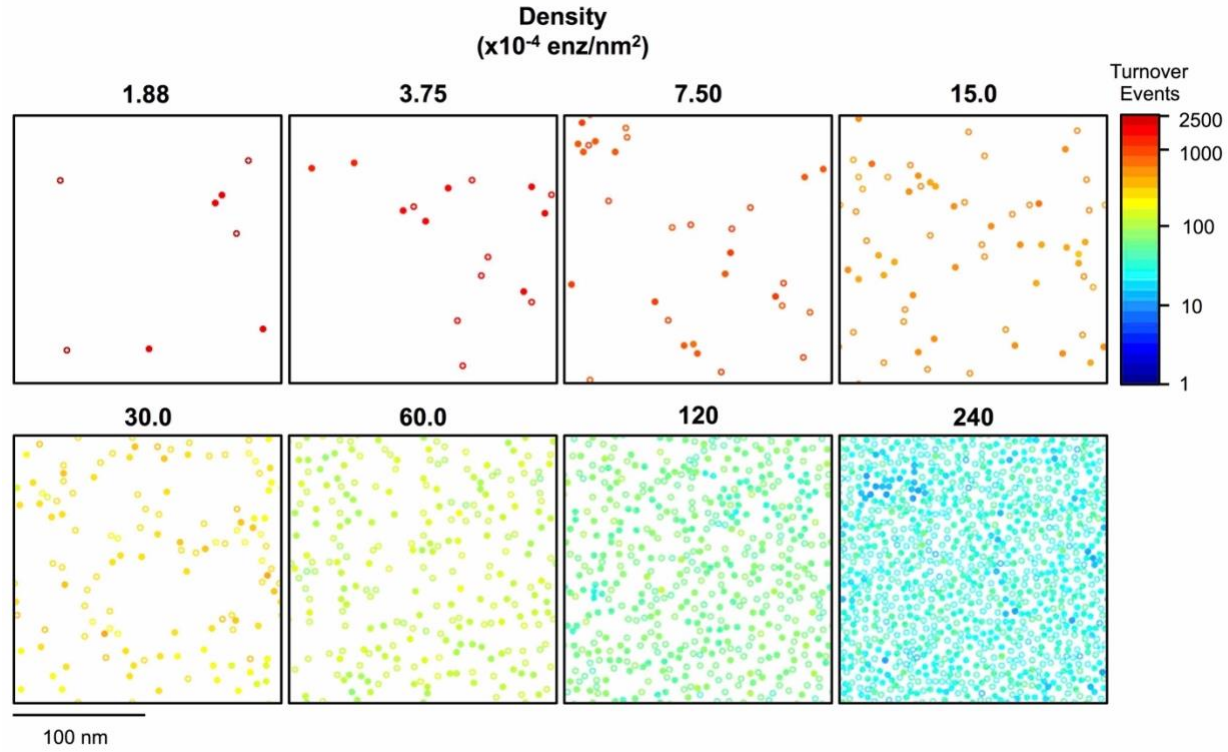

Figure A.5 Heat map of the activity of individual enzymes randomly immobilized on surfaces with coverages from 240 to 1.875 x 10^{-4} enz/nm^2. The simulations were performed under diffusion-limited conditions and the activity map shows the outcome of one representative simulation. Each enzyme is colored based on the number of reaction turnover events during the entire 137 ms simulation, as denoted by the colorbar which is presented with a $\log_{10}$-scale. The open and closed circles represent individual molecules of Enz_1 to Enz_2, respectively, and a 1:1 ratio of Enz_1 to Enz_2 was used each case.

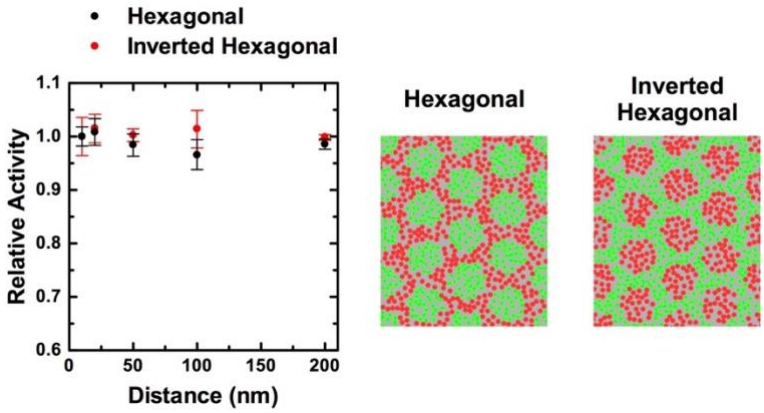

Figure A.6 Relative cascade activity as a function of geometry and center to center period (denoted distance) of hexagonal spatial arrangements under diffusion-limited conditions. Each point is the average of four independent simulations, with error bars reported as one standard deviation. As illustrated in the colorized images of enzyme position, the "hexagonal" and "inverted hexagonal" geometries have opposite tones in which Enz_1 (green) can be found in the circular spots and the continuous matrix, respectively. The position of Enz_2 molecules are denoted in red. A total enzyme density of 240 x 10^{-4} enzymes/nm^2 and 1:1 ratio of Enz_1 to Enz_2 was used for all cases.

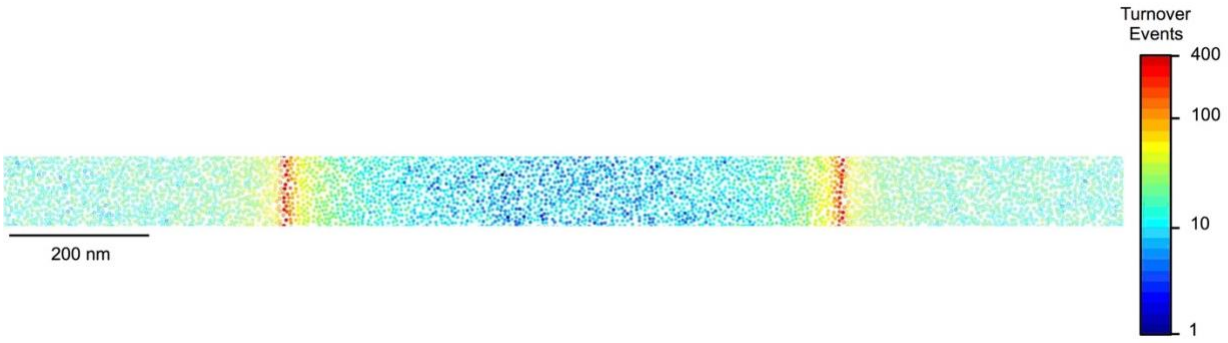

Figure A.7 Heat map of activity for individual enzymes immobilized in a lamellar spatial arrangement with a period of 1600 nm. The simulation was performed under diffusion-limited conditions and the activity map reports the outcome of one representative simulation. Each enzyme is colored based on the number of reaction turnover events during the entire 137 ms simulation, as denoted by the colorbar which is presented with a $\log_{10}$-scale. The open and closed circles represent individual molecules of Enz_1 to Enz_2, respectively. A total enzyme density of 240 x 10^{-4} enzymes/nm^2 and 1:1 ratio of Enz_1 to Enz_2 was used.

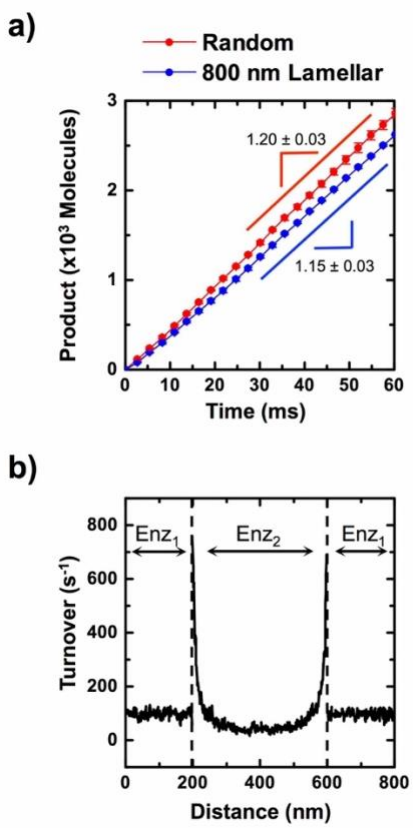

Figure A.8 Cascade activity for reaction-limited case where Enz_1 has a turnover rate of 100 s^{-1} and Enz_2 is diffusion-limited. (**a**) Cumulative product formation as a function of simulation time for randomly immobilized enzymes and enzymes immobilized on a lamellar pattern with 800 nm periodicity. Each curve is the average of three independent simulations, with error bars reported as one standard deviation. (**b**) Average enzyme turnover as a function of position for the 800 nm period lamellar spatial arrangement. A total enzyme density of 240 x 10^{-4} enzymes/nm^2 and 1:1 ratio of Enz_1 to Enz_2 was used.

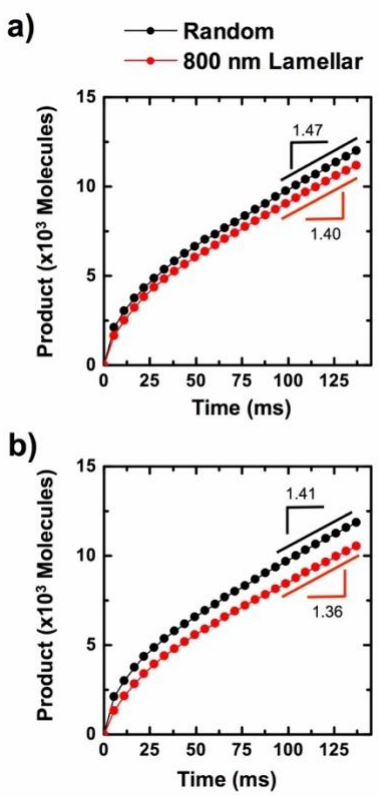

Figure A.9 Effect of altering enzyme turnover rate and stoichiometry for the diffusion-limited case. (**a**) Cascade activity with an equal number of Enz_1 and Enz_2 (*i.e.*, 1:1 ratio) for randomly immobilized enzymes and enzymes immobilized on a lamellar pattern with 800 nm periodicity. (**b**) Cascade activity for a 1:10 ratio of Enz_1 to Enz_2 in random and lamellar arrangements. A total enzyme density of 240 x 10^{-4} enzymes/nm^2 was used.

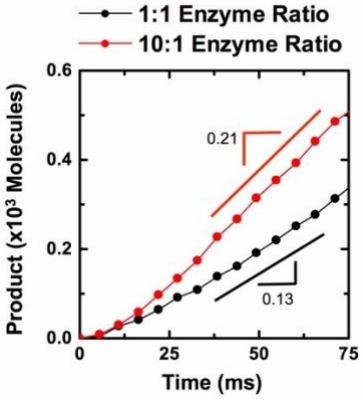

Figure A.10 Cascade activity for enzymes arranged randomly on the surface for reaction-limited conditions with a 1:1 and 10:1 ratio of Enz_1 to Enz_2. Turnover numbers were set to 10 s^{-1} and 100 s^{-1} for Enz_1 and Enz_2, respectively. A total enzyme density of 240 x 10^{-4} enzymes/nm^2 was used.

A.3 Exploiting the Benefits of Homogeneous and Heterogeneous Biocatalysis: Tuning the Molecular Interaction of Enzymes with Solvents via Polymer Modification: Supplemental Information

Table A.1 Characterization of PAN used in the preparation of LipA-PAN conjugates.

Polymer Sample Name	Mole Fraction NIPAAm[a]	Polymer M_n[b] (kg/mol)	PDI[b] (M_w/M_n)	Polymer Sample Name	Mol Fraction NIPAAm[a]	Polymer M_n[b] (kg/mol)	PDI[b] (M_w/M_n)
PAN-58	0.583	55.3	1.22	PAN-77	0.774	54.0	1.24
PAN-61	0.614	54.5	1.20	PAN-78	0.783	53.3	1.15
PAN-62	0.623	55.7	1.20	PAN-79	0.790	55.4	1.21
PAN-63	0.630	54.2	1.15	PAN-80	0.801	52.4	1.17
PAN-65	0.651	52.2	1.18	PAN-82	0.824	52.5	1.11
PAN-68	0.679	54.4	1.21	PAN-86	0.860	45.8	1.18
PAN-72	0.723	55.2	1.24	PAN-87	0.872	44.4	1.14
PAN-76	0.759	52.8	1.18	PAN-88	0.882	46.4	1.25

[a]Determined by ^{1}H NMR. [b]Measured by GPC calibrated using linear PMMA standards.

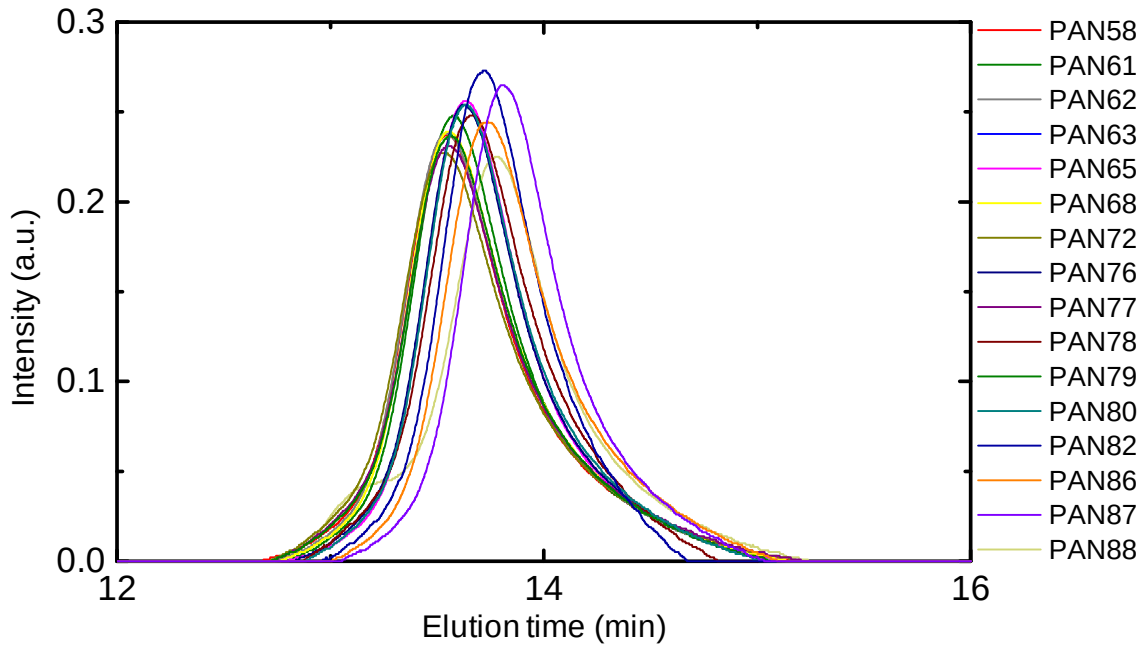

Figure A.11 GPC traces of NHS-terminated PAN at 1 mg mL^{-1} measured in DMSO with a refractive index detector using an EcoSEC HLC-8320GPC (Tosoh) system. For calibration, linear poly(methyl methacrylate) standards were used.

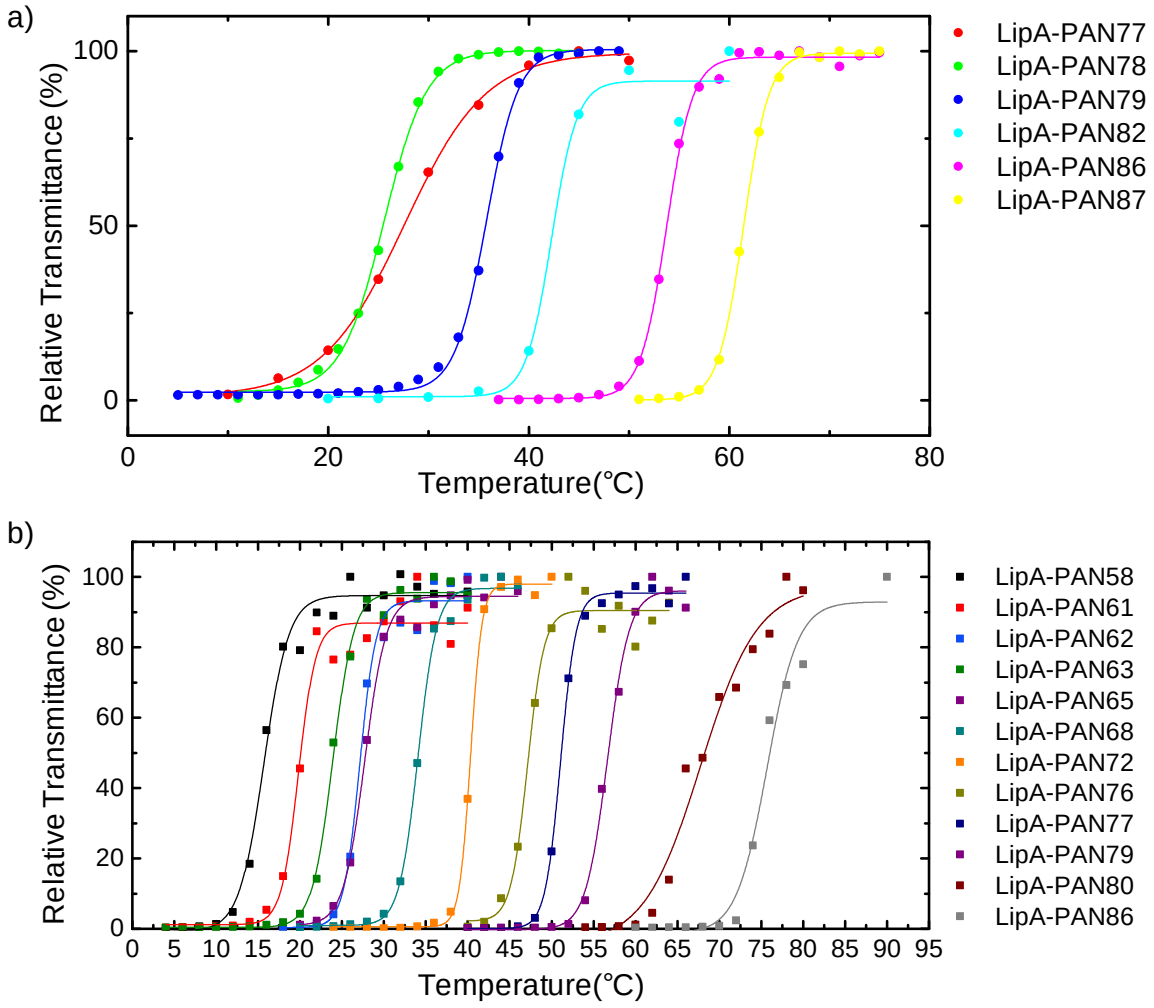

Figure A.12 Cloud point curves for all LipA-PAN conjugates at 1 mg mL^{-1} enzyme concentration in [BMIM][PF_6] without ethanol (a) or containing 1 M ethanol (b). The solid curves represent the sigmoidal fit of the raw curves of relative transmittance versus temperature from which the cloud point was determined.